A COMPARISON OF CONTROL DESIGN OPTIONS FOR HIGH ANGLE-OF-ATTACK FLIGHTS

by

PUI-CHUEN PATRICK YIP

S.B. Aeronautics and Astronautics, Massachusetts Institute of Technology
(1988)

Submitted to the Department of Aeronautics and Astronautics and
the Department of Electrical Engineering and Computer Science
in Partial Fulfillment of
the Requirements for the Degrees of

MASTER OF SCIENCE IN AERONAUTICS AND ASTRONAUTICS

and

MASTER OF SCIENCE IN ELECTRICAL ENGINEERING AND COMPUTER SCIENCE

at the

MASSACHUSETTS INSTITUTE OF TECHNOLOGY

June 1991

Signature of Author ________________________________
Department of Aeronautics and Astronautics
February 20, 1991

Certified by ________________________________
Professor Lena Valavani
Department of Aeronautics and Astronautics, Thesis Supervisor

Certified by ________________________________
Professor Munther Dahleh
Department of Electrical Engineering and Computer Science, Thesis Reader

Accepted by ________________________________
Professor Harold Y. Wachman
Chairman, Departmental Graduate Committee
Department of Aeronautics and Astronautics

Accepted by ________________________________
Professor Arthur C. Smith
Chairman, Departmental Graduate Committee
Department of Electrical Engineering and Computer Science

A COMPARISON OF CONTROL DESIGN OPTIONS FOR HIGH ANGLE-OF-ATTACK FLIGHTS

By

PUI-CHUEN PATRICK YIP

Submitted to the Department of Aeronautics and Astronautics and the Department of
Electrical Engineering and Computer Science on February 20, 1991, in partial fulfillment
of the requirements for the degrees of Master of Science in Aeronautics and Astronautics
and Master of Science in Electrical Engineering and Computer Science.

ABSTRACT

A comparative study of control designs at high angle-of-attack flights is conducted on the High Angle-of-Attack Research Vehicle (HARV) of NASA/Langley Research Center. Nonlinear model for the vehicle dynamics incorporating the high angle-of-attack nonlinearities and the nonlinear inertial couplings is derived for the inner-loop/outer-loop controller structure proposed in this thesis. The nonlinear technique of input-output linearization is utilized in the inner-loop controller to handle the nonlinearities while robust tracking control is provided through the outer-loop controller.

The performance of the nonlinear controller is compared with a LQG/LTR linear control design based on a trim point linearized model. Realistic comparison and evaluation of the controller designs are based on time simulations with a full-scale nonlinear model of the HARV provided by NASA/Langley. The time simulations show promising results for the nonlinear method proposed in this study. The nonlinear design is demonstrated to have a clear edge over the linear design in terms of superior performance at high angle-of-attack flights.

Thesis Supervisor: Dr. Lena Valavani

Title: Associate Professor of Aeronautics and Astronautics

ACKNOWLEDGEMENTS

First of all, I would like to express my deep gratitude to Professor Lena Valavani for her support, guidance, inspirations and enthusiasm she shared with me during the course of this research as my thesis supervisor. I am thankful for her time and efforts she has put into my thesis and also for the delicious thanksgiving turkey. I would also like to thank Professor Munther Dahleh for serving as my thesis reader for the Department of Electrical Engineering and Computer Science.

I am grateful to MIT for providing such a fine academic and research environment, under which I have spent almost six years for my undergraduate and graduate education. I have received lots of support and help from the faculty, colleagues and friends at MIT. In particular, I would like to thank Professor Emmet Witmer for his contagious enthusiasm that he spread to me as my undergraduate advisor, Professors Harold Wachman and Winston Markey for their help in securing the departmental fellowship that supported my first-year graduate education, and Professor Earl Murman for making Project Athena available to the general graduate student body (most of the computations involved in this research are performed on workstations provided by Project Athena). I am also grateful to the following faculty members, whose teaching and advice are much appreciated. They are Professors Lena Valavani, Munther Dahleh, Michael Athans, William Durfee, Jean-Jacques E. Slotine, Winston Markey, William Siebert, and Wallace Vander Velde. I would also like to mention my thanks to Rob Sanner, my beloved teaching assistant in 16.30 and UROP supervisor.

I am also indebted to my friends at MIT for being there when I needed them. I would like to thank my past and present colleagues and fellow graduate students in Room 41-219 and my friends in the aero/astro department. Specifically, I would like to mention Aki Inoue, Ed Wolf, Wilson Tsang, Matt Fox, Carl Resnik, Ricardo Zemella, Al Tadros and Kuok-Ming Lee. Additional gratitude is owed to Aki for providing me with the matlab functions used in generating the singular value plots and the setup of the word processing environment of this thesis. Outside the department, I would like to thank my suitemate in Tang Hall, Seong-Ho Lim, my past and present friends in Next House, and other friends I made during my undergraduate and graduate years at MIT, among whom is my good friend Choon-Phong Goh. In particular, I would like to thank Kristine Ma for all the free LSC movies she brought me in and her help and support during the last stressful months completing this thesis.

This acknowledgement is far from complete without mentioning the tremendous support I received from my family. I thank my parents for bringing me to America, giving me the opportunity to pursue my studies at MIT. I am also grateful to my big brothers and sisters who have done everything within their reach to help out their little brother. Also thanks to my friends (actually my grownup nephew and niece), Lok and Rebecca, for sharing their fun time with me by dragging me away from the computer during their tour of Boston in Christmas.

Finally, this research was supported by a grant from NASA/Langley Research Center under #NAG-1-1088. Special thanks are due to the AGCB technical staff at NASA/Langley, in particular Doug Arbuckle (now with NASA Headquarters), for their support and for providing the nonlinear simulation model of the High Angle-of-Attack Research Vehicle.

Table of Contents

List of Figures

Chapter 2 Vehicle Description and Model Formulation

Chapter 3 Input-Output Linearization

Chapter 4 Controller Design

Chapter 5 Evaluation and Comparison of the Controller Designs

Appendix

List of Tables

Chapter 2 Vehicle Description and Model Formulation

Chapter 3 Input-Output Linearization

CHAPTER 1

INTRODUCTION

1.1 Background and Motivation

Current research conducted in NASA/Langley's High Angle-of-Attack Technology Program [17] is concerned with the study of dynamics and controls of flights at very low speeds and high angles of attack (α). Theoretical analyses are coordinated with wind tunnel and flight tests to define high-α flow fields about high-performance aircraft. Special maneuvers have been studied in simulations and on the High Angle-of-Attack Research Vehicle (HARV) to explore the performance of future aircraft at high angles of attack. Because of the diminished dynamic pressure at low-speed flights, conventional aerodynamic control surfaces are less effective at high angles of attack. As a result, novel controls are investigated to provide effective moments to control the aircraft at high α's. In particular, the HARV will be fitted with thrust vectoring vanes to provide extra pitch and yaw controls at high angles of attack. The enhanced maneuverability will substantially expand the controllable flight envelope beyond stall.

As a result, new control laws are required to combine the unconventional thrust vectoring into the aircraft's fly-by-wire control system. With six degrees of freedom in translational and rotational motions, ten aerodynamic control surfaces [2] and the throttle control, the unaugmented aircraft is already a nontrivial multi-input—multi-output (MIMO) control problem. The addition of the thrust vectoring vanes further increases the complexity of the problem. A recent study was performed by Voulgaris [22] tackling the problem with the LQG/LTR and H_∞ multivariable linear design methodologies. His study was based on linear models at trim points with moderate values of α. The trim points were selected at $\alpha = 2.95$, 5 and 25 deg, even though controllable flight up to 70 deg is postulated by preliminary studies [17]. Furthermore, his simplified approach to the problem was confined to the longitudinal motion of the aircraft. The emphasis of the study was on the demonstration and comparison of the two design methodologies, together with a systematic selection of the redundant control inputs. In the above study, little attention was paid to the inherent dynamics of the aircraft at high α. Besides, recent results [3, 11] have shown that linear designs that attempt approximate inversion, like the LQG/LTR and H_∞ methodologies, are very sensitive to structured uncertainties in the presence of lightly damped poles. An inner-loop compensation was shown to be needed to desensitize the plant for these linear design methods to apply. In [3, 11], an inner-loop/outer-loop controller structure was needed to provide robustness to structured uncertainties facing these linear design methods.

Conventional studies of steady flight, with decoupled longitudinal and lateral motions, are based on the linearized equations of motion, neglecting all aerodynamic cross couplings [7]. This simplified, decoupled linear model is severely limited for flights at high α. At high angles of attack, highly nonlinear dynamics are caused by the unsteady and nonlinear aerodynamic flowfields around the aircraft [9]. Examples of these phenomena include vortex shedding and separation and reattachment of flows. Consequently, the aerodynamic characteristics vary nonlinearly with α at high angles of attack and a high degree of coupling exists between the lateral and longitudinal motions because of inertial coupling. Attached in Appendix A are some plots showing the α-nonlinearities of the aerodynamic characteristics (please refer to Section 2.5.1 for the definitions of the aerodynamic quantities shown in the plots). Meanwhile, the inertial coupling is evidenced by product terms like those involving the roll rate and the crosswind velocity (PV) and others involving the yaw rate and the roll rate (RP) in the time derivatives of the longitudinal variables. (The equations of motion are shown in equations 2-1 to 2-6 in Chapter 2.) Moreover, severe control problems are encountered because the aerodynamic control surfaces become ineffective at low speeds and high α's. It is indeed a challenge to maintain a sustained flight at the boundary of the expanded envelope.

Because of the severe nonlinear characteristics of the vehicle dynamics at high α, one is tempted to venture outside the linear design domain (as represented by the LQG/LTR and H_∞ designs by Voulgaris [22]), and choose to design with nonlinear methods. Indeed, there has been previous work involving the use of nonlinear techniques for flight control. Nonlinear inversion/sliding control techniques were used by Hedrick and Gopalswamy [10] to design a pitch-axis control system for high-performance aircraft. Angle of attack nonlinearities present in the aerodynamic coefficients were incorporated into the design using inversion techniques and sliding controllers were employed for robustness to modelling errors. Meyer *et al.* [16] used nonlinear transformations for linearization of the aircraft dynamics. Garrad and Jordan [8] used a nonlinear optimal approach for the pitch axis control of the F8 Crusader. Lane and Stengel [15] designed a controller for the Navion general aviation aircraft incorporating the nonlinear vehicle dynamics (both nonlinear inertial couplings and α-nonlinearities). Their design "decouples specific state variables that are of particular interest to the pilot" by the use of nonlinear inverse dynamics. In [6], Elgersma and Morton designed a controller based on partial nonlinear inversion. They computed the inverse dynamics of the invertible part of the nonlinear system and studied the stability of the uninverted part of the system to ensure adequate performance of the partially inverted system. Moreover, significant progress and improvements have been made in nonlinear design techniques like input-state linearization, input-output linearization and sliding controls [4, 12, 19].

The goal of the thesis is an exploration of the nonlinear design alternative combining the nonlinear inversion/feedback linearization techniques and the robustness motivated inner-loop/outer-loop controller structure, while a comparison is drawn to a baseline LQG/LTR linear design along Vouglaris's approach in [22]. The comparison is an important part of the study providing concrete and realistic evaluations of the different design approaches.

1.2 Contribution of the Thesis

Instead of designing around the simplified, decoupled linear model for the vehicle dynamics, this thesis spends a substantial effort in developing a nonlinear model for the vehicle dynamics starting from the rigid-body equations of motion. Undoubtedly, simplifying assumptions are made along the development, but the reader is informed of these assumptions, and can be alerted to the consequences of the violations of these assumptions. On the other hand, despite these simplifying assumptions, the model still captures a major part of the nonlinearities, like the nonlinear variations of the aerodynamic characteristics with α, and the inertial coupling between the longitudinal and lateral motions, which are totally ignored in the linear models. Moreover, previous nonlinear approaches only involved the decoupled longitudinal motion [8, 10]. A totally nonlinear approach is taken here to design for high performance.

In the meantime, by combining the robustness-motivated inner-loop/outer-loop controller structure with the input-output linearization method for high performance, this thesis has demonstrated a systematic way for designing robust, high-performance controllers for highly nonlinear systems. Finally, the comparison with the conventional linear LQG/LTR design provides realistic evaluations of the two different design approaches by hooking up the controller designs with a full-scale nonlinear model of the HARV for time simulations. Promising results are obtained for the nonlinear approach in terms of superior performance and robustness at high-α flights.

1.3 Organization of the Thesis

This thesis is organized into six chapters and six appendices. The current chapter has described the background, motivation, and contribution of the thesis. Chapter 2 gives a description of the High Angle-of-Attack Research Vehicle (HARV) and the derivation of the nonlinear model of the vehicle dynamics. Chapter 3 describes the nonlinear design method known as input-output linearization, which is applied on the HARV in the inner-loop compensator. Chapter 4 provides a description of the linear and nonlinear controller designs proposed to be studied. Chapter 5 is a comparison between the baseline LQG/LTR linear design along the approach of Voulgaris in [22] and the nonlinear inner-loop/outer-loop designs incorporating input-output linearization techniques. Chapter 6 discusses the results and proposes directions for future research.

The appendices include graphical results showing the nonlinear aerodynamic characteristics of the vehicle, and validation of the nonlinear model developed in Chapter 2. Meanwhile, complex mathematical expressions and numerical data involved in the design and analysis of the control systems are also included in the appendices. Specifically, Appendix A includes the plot showing the variations of the aerodynamic stability derivatives with α. Appendix B contains time simulation results verifying the nonlinear model of the vehicle dynamics derived in Chapter 2. Algebraic details involved in the derivation of the input-output linearizing controller are collected in Appendix C. Numerical data for the linear models derived in Chapter 2 are presented in Appendix D. Plots of the aerodynamic coefficients vs. the control surface deflections are shown in Appendix E. Lastly, numerical data for the LQG/LTR controllers in Chapter 4 are included in Appendix F.

CHAPTER 2

VEHICLE DESCRIPTION AND MODEL FORMULATION

2.1 Introduction

This chapter contains a brief description of the aircraft and the control inputs. Rigid-body equations of motion are derived to describe the vehicle dynamics based on the approach in [7]. From this set of nonlinear equations, a state-space description of the vehicle dynamics is obtained incorporating the kinematics, aerodynamics and characteristics of the propulsive elements. The derivation of the nonlinear model is completed with a discussion about the determination of the aerodynamic and propulsive forces and moments, given the state variables and control inputs. Linear models of the vehicle dynamics can also be obtained from the nonlinear state-space model by perturbation about equilibrium points.

2.2 Description of the F18/High-Angle-of-Attack Research Vehicle (HARV)

The F18 High Angle-of-Attack Research Vehicle is a modified version of the F/A-18 "Hornet" aircraft operated by NASA/Langley in the High Angle-of-Attack Technology Program. It is equipped with a thrust vectoring control system providing extra maneuverability for the F/A-18. The thrust vectoring control system is especially important at high angle-of-attack, low-speed flights when the low dynamic pressure renders the aerodynamic control surfaces ineffective.

The F/A-18 shown in Figure 2.1 [2] is outfitted with two General Electric F404 turbofan engines, each producing approximately 712 kN (16000 lb) sea-level static thrust at full power. The wing planform is a low-sweep, trapezoidal design with an area of 400 square feet. The aerodynamic control surfaces (illustrated in Figure 2.2 [2]) include:

(i) Leading edge and trailing edge flaps scheduled with angle-of-attack and Mach number.

(ii) Single slotted, drooped ailerons for take-off and landing, with ± 25° deflection for maneuvering and cruise conditions.

(iii) Twin rudders for directional control and roll coordination.

(iv) All moving stabilators.

As mentioned above, the leading and trailing edge flaps are scheduled with angle of attack (α) and Mach number (M). However, for the flight conditions we are interested in, i.e. high α and low speed, the deflection schedule is almost constant. As a result, the flaps are considered fixed in this thesis.

Additionally, controls for the propulsive elements include:

(v) Throttle positions regulating the thrust output of each individual engine.

(vi) Thrust vectoring control system (see Figure 2.3) providing multi-axis thrust vectoring.

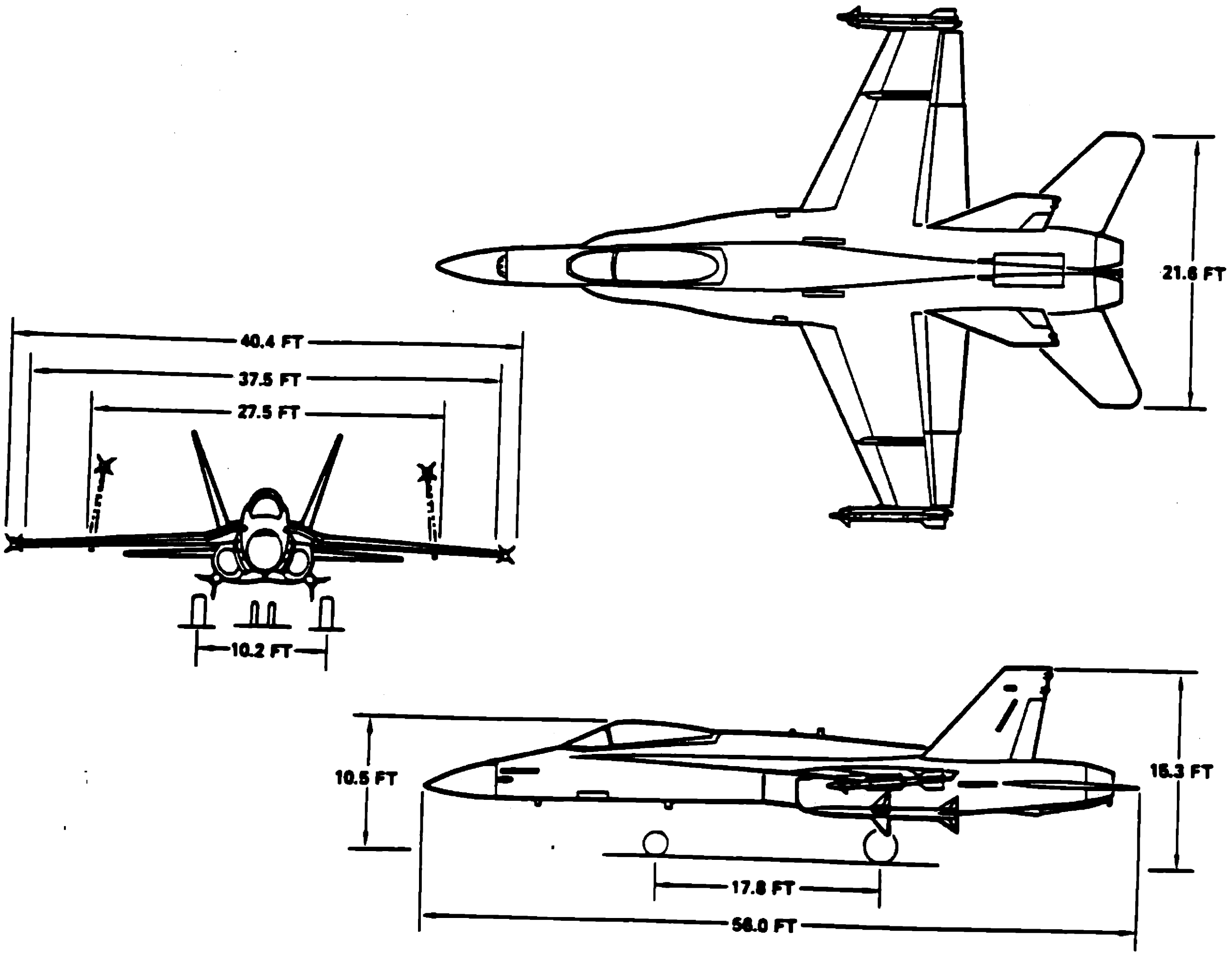

Figure 2.1 F/A-18 "Hornet " Aircraft

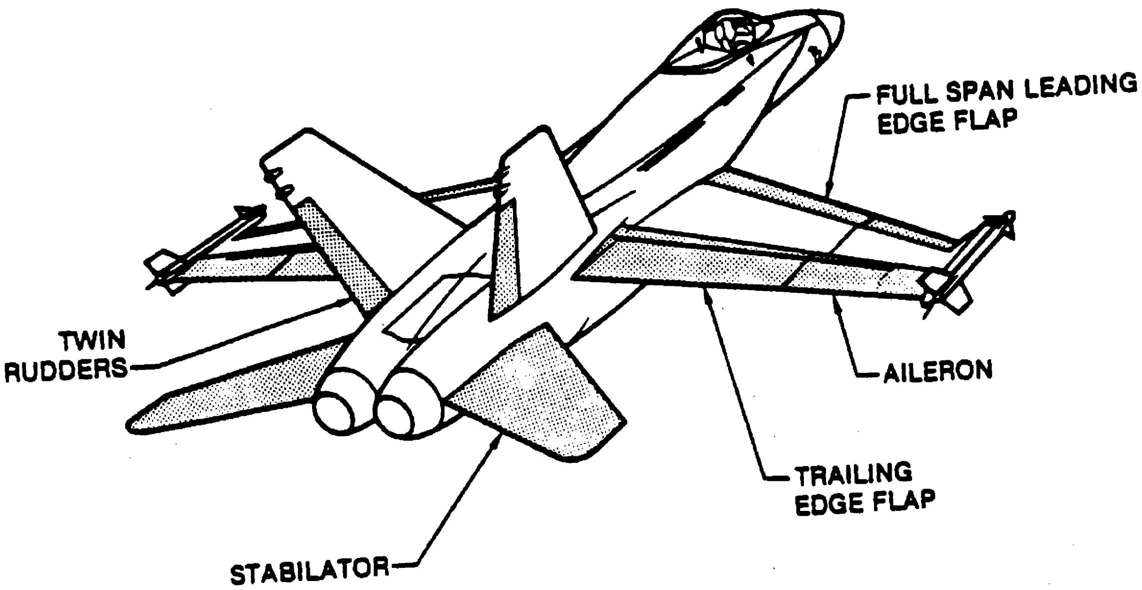

Figure 2.2 Aerodynamic Control Surfaces

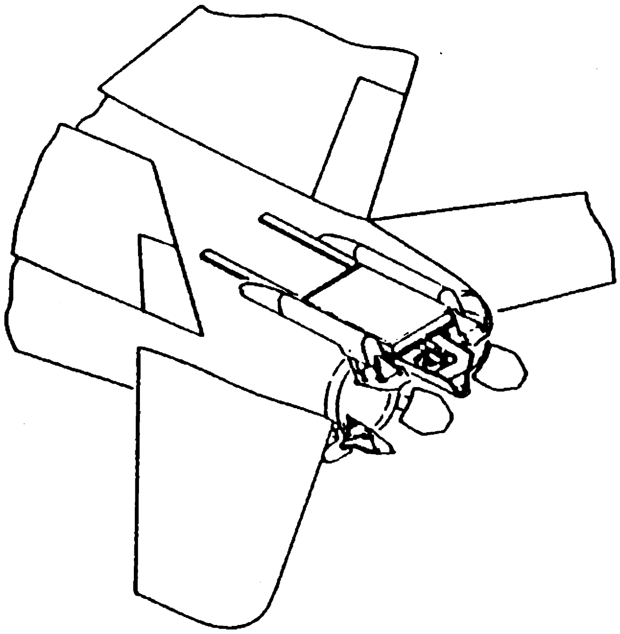

Figure 2.3 Thrust Vectoring Control System

2.3 Equations of Motion

The six-degree-of-freedom rigid-body equations of motion given here are based on a coordinate system fixed in the aircraft, with origin at the center of mass (see illustration in Figure 2.4). The equations are derived assuming symmetry of the airplane about the xz-plane and the absence of any rotor gyroscopic effects.

$$X - mg \sin \theta = m(\dot{U} + QW - RV) \tag{2-1}$$

$$Y + mg \cos \theta = m(\dot{V} + RU - PW) \tag{2-2}$$

$$Z + mg \cos \theta \cos \phi = m(\dot{W} + PV - QU) \tag{2-3}$$

$$L = I_{xx}\dot{P} - I_{xz}\dot{R} + QR(I_{zz} - I_{yy}) - I_{xz}PQ \tag{2-4}$$

$$M = I_{yy}\dot{Q} + RP(I_{xx} - I_{zz}) + I_{xz}(P^2 - R^2) \tag{2-5}$$

$$N = -I_{xz}\dot{P} + I_{zz}\dot{R} + PQ(I_{yy} - I_{xx}) + I_{xz}QR \tag{2-6}$$

where m is the mass of the airplane,

g is the acceleration of gravity,

P, Q, and R are the roll, pitch, and yaw rates,

I_{xx}, I_{yy}, and I_{zz} are the moments of inertia,

I_{xz} is the product of inertia $\int xz\, dm$,

θ, ϕ, and ψ are the Euler angles corresponding to pitch, roll, and yaw,

X, Y, Z, L, M, and N are components of the external (aerodynamic and propulsive) forces and moments along the x, y, and z axes respectively,

U, V, and W are components of the velocity of the airplane along the x, y, and z axes.

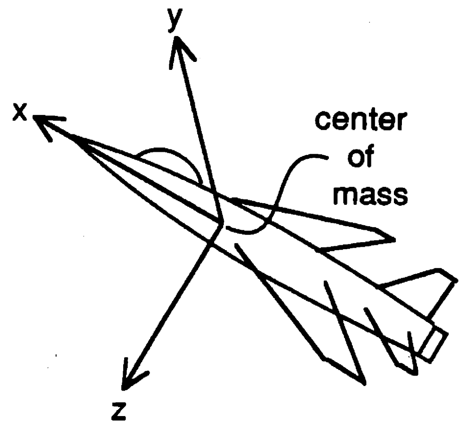

Figure 2.4 Orientation of the Body-Axis Coordinate System

2.4 State-Space Description of the Vehicle Dynamics

In the state-space form of description of dynamic system, we would like to express the rate of change of the state variables as a function of the state variables and the control inputs. We have to transform the equations of motion into the form of $\dot{\mathrm{x}} = \mathrm{f}(\mathrm{x},\mathbf{u})$, where x is the state vector, and $\mathbf{u}$ is the vector of control inputs.

In equations 2-1 to 2-3, the velocity vector is represented in component form with U, V, and W. On the other hand, the velocity vector is usually described by the more familiar parameters: total airspeed (V_t), angle of attack (α), and sideslip angle (β) (see Figure 2.5 [7] for the definitions of α and β).

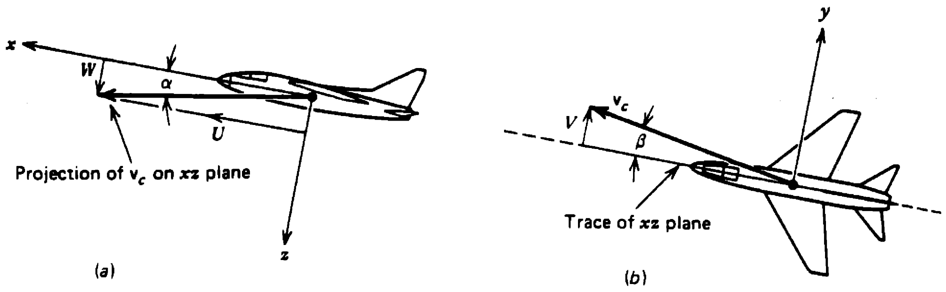

Figure 2.5 (a) Definition of α

(b) Definition of β, viewed in plane of y and v_c (velocity vector)

If we switch from U, V, and W to the state variables V_t, α, and β, and solve for the time derivatives of V_t, α, and β, we get:

$$\dot{V}_t = g(\cos\theta\cos\phi\cos\beta\sin\alpha - \sin\theta\cos\beta\cos\alpha + \cos\theta\sin\phi\sin\beta) + \frac{X}{m}\cos\beta\cos\alpha + \frac{Z}{m}\cos\beta\sin\alpha + \frac{Y}{m}\sin\beta \tag{2-7}$$

$$\dot{\alpha} = Q - \tan\beta\,(P\cos\alpha + R\sin\alpha) + \frac{g}{V_t\cos\beta}(\cos\theta\cos\phi\cos\alpha + \sin\alpha\sin\theta) + \frac{1}{V_t\cos\beta}\left(-\frac{X}{m}\sin\alpha + \frac{Z}{m}\cos\alpha\right) \tag{2-8}$$

$$\dot{\beta} = P\sin\alpha - R\cos\alpha + \frac{1}{V_t}\left(-\frac{X}{m}\sin\beta\cos\alpha - \frac{Z}{m}\sin\beta\sin\alpha + \frac{Y}{m}\cos\beta\right) + \frac{g}{V_t}(\sin\theta\cos\alpha\sin\beta - \cos\theta\cos\phi\sin\alpha\sin\beta + \cos\beta\cos\theta\sin\phi) \tag{2-9}$$

Solving for the time derivatives of the state variables P, Q and R from equations 2-4 to 2-6:

$$\dot{P} = (A/B)PQ + (C/B)QR + (I_{zz}/B)N \tag{2-10}$$

$$\dot{Q} = [(I_{zz} - I_{xx})/I_{yy}]\,RP + (I_{xz}/I_{yy})(R^2 - P^2) + M/I_{yy} \tag{2-11}$$

$$\dot{R} = (D/B)PQ + (E/B)QR + (I_{xz}/B)L + (I_{xx}/B)N \tag{2-12}$$

where $A = I_{zz}I_{xz} + I_{xz}I_{xx} - I_{xz}I_{yy}$

$B = I_{xx}I_{zz} - I_{xz}^2$

$C = -I_{zz}^2 - I_{xz}^2 + I_{zz}I_{yy}$

$D = I_{xx}^2 + I_{xz}^2 - I_{xx}I_{yy}$

$E = -I_{xz}I_{zz} + I_{xz}I_{yy} - I_{xx}I_{xz}$

We also need the rate of change of the Euler angles, the state variables θ, ϕ, and ψ:

$$\dot{\theta} = Q\cos\phi - R\sin\phi \tag{2-13}$$

$$\dot{\phi} = P + Q\sin\phi\tan\theta + R\cos\phi\tan\theta \tag{2-14}$$

$$\dot{\psi} = Q\sin\phi\sec\theta + R\cos\phi\sec\theta \tag{2-15}$$

For the altitude (h),

$$\dot{h} = V_t \cos\beta \cos(\theta - \alpha) \quad (2\text{-}16)$$

The external forces and moments labeled X, Y, Z, L, M, and N include contributions from both the aerodynamic, and propulsive elements of the aircraft. The aerodynamic component is characterized by the non-dimensional aerodynamic coefficients while the propulsive component depends on the thrust level, thrust vector setting and the location of the engines. Breaking down the forces and moments into the corresponding aerodynamic and propulsive elements, we obtain:

$$X = 1/2\ \rho V_t^2 S[C_L \sin\alpha - C_D \cos\alpha] + T_X \quad (2\text{-}17)$$

$$Y = 1/2\ \rho V_t^2 S C_Y + T_Y \quad (2\text{-}18)$$

$$Z = -1/2\ \rho V_t^2 S[C_L \cos\alpha + C_D \sin\alpha] + T_Z \quad (2\text{-}19)$$

$$L = 1/2\ \rho V_t^2 S b C_l + T_L \quad (2\text{-}20)$$

$$M = 1/2\ \rho V_t^2 S c C_M + T_M \quad (2\text{-}21)$$

$$N = 1/2\ \rho V_t^2 S b C_N + T_N \quad (2\text{-}22)$$

where C_L, C_D, C_Y are the aerodynamic coefficients for lift, drag, and side force,

C_l, C_M, C_N are the aerodynamic coefficients for the rolling, pitching, and yawing moments,

T_x, T_y, T_z are components of the propulsive forces,

T_L, T_M, T_N are components of the propulsive moments about the center of mass,

S is the wing area,

b is the wing span,

and c is the average wing chord.

From equations 2-17 to 2-18, we can see that the aerodynamic control surfaces become less effective at low speeds, since they affect the dynamics through the aerodynamic forces and moments, which go down with the dynamic pressure ($1/2\ \rho V_t^2$).

Substituting in equations 2-7 to 2-9 the above expressions for the external forces and moments, we get:

$$\begin{aligned}\dot{V}_t = {} & g(\cos\theta\cos\phi\cos\beta\sin\alpha - \sin\theta\cos\beta\cos\alpha + \cos\theta\sin\phi\sin\beta)\\ & + \frac{\frac{1}{2}\rho V_t^2}{m} S(-C_D\cos\beta + C_Y\sin\beta)\\ & + \frac{1}{m}(T_X\cos\alpha\cos\beta + T_Y\sin\beta + T_Z\cos\beta\sin\alpha)\end{aligned} \tag{2-23}$$

$$\begin{aligned}\dot{\alpha} = {} & Q - \tan\beta(P\cos\alpha + R\sin\alpha) + \frac{g}{V_t\cos\beta}(\cos\theta\cos\phi\cos\alpha + \sin\alpha\sin\theta)\\ & - \frac{\frac{1}{2}\rho V_t}{m} S\,C_L + \frac{1}{m\,V_t\cos\beta}(-T_X\sin\alpha + T_Z\cos\alpha)\end{aligned} \tag{2-24}$$

$$\begin{aligned}\dot{\beta} = {} & P\sin\alpha - R\cos\alpha + \frac{\frac{1}{2}\rho V_t}{m} S\,(C_D\sin\beta + C_Y\cos\beta)\\ & + \frac{g}{V_t}(\sin\theta\cos\alpha\sin\beta - \cos\theta\cos\phi\sin\alpha\sin\beta + \cos\beta\cos\theta\sin\phi)\\ & + \frac{1}{mV_t}(-T_X\sin\beta\cos\alpha + T_Y\cos\beta - T_Z\sin\beta\sin\alpha)\end{aligned} \tag{2-25}$$

Furthermore, the state equations can be simplified if we consider flight regimes with small sideslips, i.e. small β. The following relations can then be used to simplify the state equations:

$$\sin\beta \approx \beta,\ \tan\beta \approx \beta,\ \cos\beta \approx 1.$$

After all the above manipulations, the final form of the state equations becomes:

$$\begin{aligned}\dot{V}_t = {} & 1/2\ (\rho/m)V_t^2 S[-C_D + \beta\, C_Y] + g[\cos\theta\cos\phi\sin\alpha - \sin\theta\cos\alpha + \beta\cos\theta\sin\phi]\\ & +1/m\ (\cos\alpha\, T_X + \beta T_Y + \sin\alpha\, T_Z)\end{aligned} \tag{2-26}$$

$$\begin{aligned}\dot{\alpha} = {} & Q + (g/V_t)[\cos\theta\cos\phi\cos\alpha + \sin\alpha\sin\theta] - \beta P\cos\alpha - \beta R\sin\alpha\\ & - 1/2\ (\rho/m)V_t S C_L + 1/(V_t m)\ [-\sin\alpha\, T_X + \cos\alpha\, T_Z]\end{aligned} \tag{2-27}$$

$$\dot{\beta} = 1/2\,(\rho/m)V_tS[\beta C_D + C_Y] + g/V_t\ [\beta(\sin\theta\cos\alpha - \cos\theta\sin\alpha\cos\phi) + \sin\phi\cos\theta]$$
$$+ P\sin\alpha - R\cos\alpha + 1/(V_tm)\ [T_Y - T_X\beta\cos\alpha - T_Z\beta\sin\alpha] \tag{2-28}$$

$$\dot{P} = (A/B)PQ + (C/B)QR + (I_{ZZ}/B)(1/2\ \rho V_t^2SbC_l + T_L)$$
$$+ (I_{XZ}/B)(1/2\ \rho V_t^2SbC_N + T_N) \tag{2-29}$$

$$\dot{Q} = (I_{ZZ} - I_{XX})/I_{yy}\ RP + I_{XZ}/I_{yy}\ (R^2 - P^2) + (1/2\ \rho V_t^2ScC_M + T_M)/I_{yy} \tag{2-30}$$

$$\dot{R} = (D/B)PQ + (E/B)QR + (I_{XZ}/B)(1/2\ \rho V_t^2SbC_l + T_L)$$
$$+ (I_{XX}/B)(1/2\ \rho V_t^2SbC_N + T_N) \tag{2-31}$$

$$\dot{\theta} = Q\cos\phi - R\sin\phi \tag{2-32}$$

$$\dot{\phi} = P + Q\sin\phi\tan\theta + R\cos\phi\tan\theta \tag{2-33}$$

$$\dot{\psi} = Q\sin\phi\sec\theta + R\cos\phi\sec\theta \tag{2-34}$$

At this point, we have dropped the altitude (h) from the state vector for the following reasons. First, h is not affected directly by the controls. Secondly, for small perturbations in altitude (particularly in a linearized model), h has negligible effects on the rest of the state variables. Besides, h influences the dynamics only through the variation of air density (ρ) with altitude (since we are going to neglect the effects of Mach number on the aerodynamic coefficients). With information about h gathered from the altimeter, we can incorporate this variation into the air density we have used to calculate the aerodynamic forces and moments.

2.5 Aerodynamic and Propulsive Forces and Moments

2.5.1 Approximations of the Aerodynamic Coefficients

The aerodynamic coefficients appearing in equations 2-26 to 2-31 can be approximated by means of stability derivatives obtained at a range of values of α. The stability derivatives are obtained by perturbing the states and controls (from the trim settings) one at a time with different α's. The trim settings of the states and controls (aerodynamic control surfaces) are selected to be those corresponding to a steady, level flight. This leads to the following trim settings:

$\beta = 0,$

$P = Q = R = 0,$

and zero deflections for the rudders and ailerons.

However, the steady-level-flight setting of the stabilator (elevator) changes with the value of α. As a result, a single trim setting is selected for the stabilator corresponding to a steady straight level flight at $\alpha = 35°$. Table 2.1 shows the numerical values used for the trim settings of the control surfaces.

Table 2.1 Trim Settings of Control Surfaces for the Determination of Aerodynamic Coefficients

Control Surface	Deflection in Degree (down as positive)
Aileron	0
Rudder	0 (in as positive)
Stabilator	-9.70415
Leading-Edge Flap	0
Trailing-Edge Flap	33

Assuming the effects of the Mach number are negligible at the flight regimes of interest (low speed and high α), the aerodynamic coefficients can be approximated as:

$$C_L \approx C_{L0}(\alpha) + \frac{\partial C_L}{\partial Q}(\alpha)\cdot Q + \frac{\partial C_L}{\partial Ail_{sym}}(\alpha)\cdot Ail_{sym} + \frac{\partial C_L}{\partial Stab_{sym}}(\alpha)\cdot Stab_{sym} \tag{2-35}$$

$$C_D \approx C_{D0}(\alpha) + \frac{\partial C_D}{\partial Q}(\alpha)\cdot Q + \frac{\partial C_D}{\partial Stab_{sym}}(\alpha)\cdot Stab_{sym} \tag{2-36}$$

$$\begin{aligned} C_Y \approx\ & \frac{\partial C_Y}{\partial \beta}(\alpha)\cdot \beta + \frac{\partial C_Y}{\partial P}(\alpha)\cdot P + \frac{\partial C_Y}{\partial R}(\alpha)\cdot R \\ & + \frac{\partial C_Y}{\partial Ail_{asy}}(\alpha)\cdot Ail_{asy} + \frac{\partial C_Y}{\partial Rud}(\alpha)\cdot Rud + \frac{\partial C_Y}{\partial Stab_{asy}}(\alpha)\cdot Stab_{asy} \end{aligned} \tag{2-37}$$

$$\begin{aligned} C_l \approx\ & C_{l asy} + \frac{\partial C_l}{\partial \beta}(\alpha)\cdot \beta + \frac{\partial C_l}{\partial P}(\alpha)\cdot P + \frac{\partial C_l}{\partial R}(\alpha)\cdot R \\ & + \frac{\partial C_l}{\partial Ail_{asy}}(\alpha)\cdot Ail_{asy} + \frac{\partial C_l}{\partial Rud}(\alpha)\cdot Rud + \frac{\partial C_l}{\partial Stab_{asy}}(\alpha)\cdot Stab_{asy} \end{aligned} \tag{2-38}$$

$$C_M \approx C_{M0}(\alpha) + \frac{\partial C_M}{\partial Q}(\alpha)\cdot Q + \frac{\partial C_M}{\partial Ail_{sym}}(\alpha)\cdot Ail_{sym} + \frac{\partial C_M}{\partial Stab_{sym}}(\alpha)\cdot Stab_{sym} \tag{2-39}$$

$$\begin{aligned} C_N \approx\ & \frac{\partial C_N}{\partial \beta}(\alpha)\cdot \beta + \frac{\partial C_N}{\partial P}(\alpha)\cdot P + \frac{\partial C_N}{\partial R}(\alpha)\cdot R \\ & + \frac{\partial C_N}{\partial Ail_{asy}}(\alpha)\cdot Ail_{asy} + \frac{\partial C_N}{\partial Rud}(\alpha)\cdot Rud + \frac{\partial C_N}{\partial Stab_{asy}}(\alpha)\cdot Stab_{asy} \end{aligned} \tag{2-40}$$

where Ail_{sym} = (Deflection of Right Aileron + Deflection of Left Aileron) / 2

$Stab_{sym}$ = (Deflection of Right Stabilator + Deflection of Left Stabilator) / 2

Ail_{asy} = (Deflection of Right Aileron - Deflection of Left Aileron) / 2

Rud = Deflection of the twin rudders acted in unison

$Stab_{asy}$ = (Deflection of Right - Deflection of Left Stabilator) / 2

and the functional dependence of the stability derivatives upon α is indicated as in

$$\frac{\partial C_L}{\partial Q}(\alpha),\quad \frac{\partial C_M}{\partial Stab_{sym}}(\alpha),\ \text{etc.}$$

Stability derivatives involving the leading edge and trailing edge flaps are not included in equations 2-35 to 2-40 because the flaps are assumed to be fixed as explained in Section 2.2.

The aerodynamic coefficients at the perturbed settings are obtained from the ACSL (Advanced Continuous Simulation Language) simulation code provided by Doug Arbuckle (previously with NASA/Langley, now with NASA Headquarters). The corresponding stability derivatives are then calculated as the ratios of the changes in the coefficients over the perturbations. For example, $\partial C_L/\partial Q$ is calculated as $\Delta C_L/\Delta Q$ where ΔQ is the perturbation in Q, and ΔC_L is the resulting change in the lift coefficient. The stability derivatives listed in equations 2-34 to 2-39 are calculated at a set of values of α. The values of the stability derivatives at other settings of α can be easily obtained through linear interpolations. (Furthermore, they can even be approximated as simple analytic functions of α, and calculated as such.) Attached in Appendix A are some plots showing the behavior of the stability derivatives at various values of α.

Two analytical models for the airplane dynamics are developed based on these aerodynamics data. In the first model (model 1), the aerodynamic coefficients are obtained through linear interpolation of the stability derivatives data set at the desired α. In the second model (model 2), the aerodynamic coefficients are calculated treating the stability derivatives as simple analytic functions of α, obtained from the curve-fitting approximations of the data set. As a comparison of these models with the "true" model provided from Doug Arbuckle (the ACSL simulation codes), time simulations (using a fourth-order Runge-Kutta integration scheme) were performed on all three models at flight settings slightly perturbed from a steady, level flight with fixed controls. The simulation results are attached in Appendix B. When the airplane motion is purely longitudinal, both models 1 and 2 seem to give acceptable results. Nevertheless, model 1 appears to be more accurate. When lateral motion is involved, model 2 gives totally different results compared with the other two models. This can be attributed to the bigger errors in the curve-fitting approximations of the lateral aerodynamic coefficients C_Y, C_l, and C_N. Since the lateral motion is coupled with the longitudinal counterpart, big errors in the lateral states (β, P, R, ϕ, and ψ) also lead to big errors in the longitudinal states (V_t, α, Q, and θ). Besides, β is assumed to be small in the derivations of the state equations (3a-3f). When β gets large ($|\beta| > 5°$), as in the results from model 2, the analytical model is no longer valid.

2.5.2 Propulsive Forces and Moments

The propulsive forces and moments depend on the throttle settings of the left and right engines, the locations of the engines, and the orientations of the thrust vectoring vanes. However, the key elements are the effective thrust output from each individual engine through the thrust-vectoring vanes. Once we figure out the components of the effective thrust from each engine, we can easily calculate the moments induced by the engine forces.

The thrust-vectoring vanes are modelled as devices capable of deflecting the thrust within a 30-deg cone from the nominal thrust line of each engine. However, the deflection also causes a loss in the effective thrust by a factor of $(1 - \cos(\sigma))$, where σ is the angle between the deflected thrust and the nominal thrust line.

Taking into account the locations and orientations of the engines, the components of the effective thrust from the left engine are as follows:

$$Tx_l = T_l \cos(\sigma_l)(\cos(\sigma_l)\cos\delta + \sin(\sigma_l)\sin(\eta_l)\sin\delta) \quad (2\text{-}41)$$

$$Ty_l = T_l \cos(\sigma_l)(-\cos(\sigma_l)\sin\delta + \sin(\sigma_l)\sin(\eta_l)\cos\delta) \quad (2\text{-}42)$$

$$Tz_l = -T_l \cos(\sigma_l)\sin(\sigma_l)\cos(\eta_l) \quad (2\text{-}43)$$

For the right engine:

$$Tx_r = T_r \cos(\sigma_r)(\cos(\sigma_r)\cos\delta - \sin(\sigma_r)\sin(\eta_r)\sin\delta) \quad (2\text{-}44)$$

$$Ty_r = T_r \cos(\sigma_r)(\cos(\sigma_r)\sin\delta + \sin(\sigma_r)\sin(\eta_r)\cos\delta) \quad (2\text{-}45)$$

$$Tz_r = -T_r \cos(\sigma_r)\sin(\sigma_r)\cos(\eta_r) \quad (2\text{-}46)$$

where T is the magnitude of the undeflected thrust,

Tx, Ty, and Tz are components of the effective thrust along the x, y, and z axes,

δ is the angle between the nominal thrust line and the center-line of the airplane,

σ and η are the parameters describing the orientations of the deflected thrust,

and the subscripts l and r denote the left and right engine respectively.

The angles δ, σ, and η are illustrated in Figure 2.6.

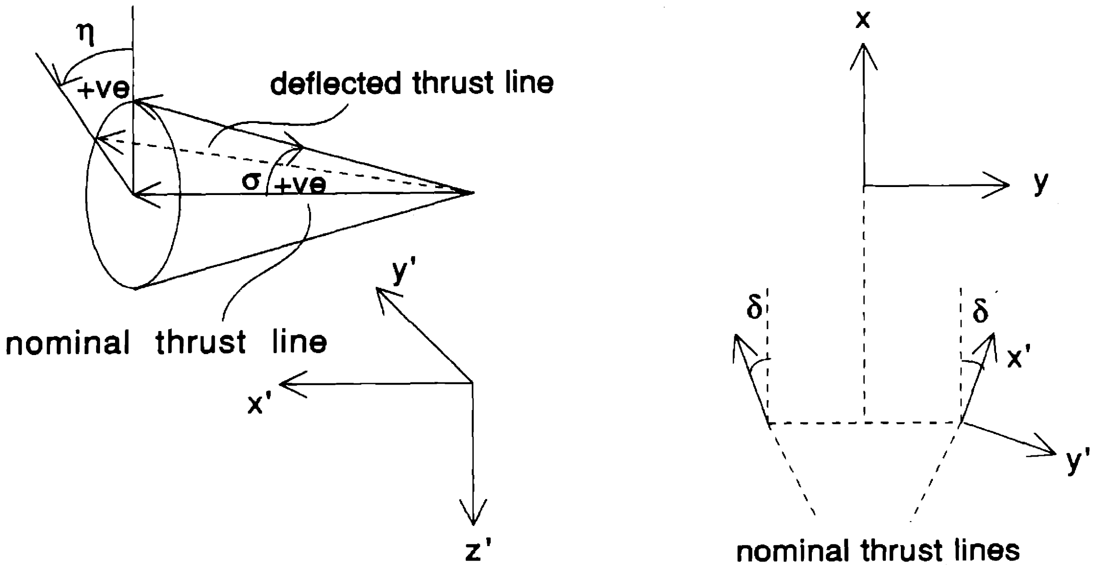

Figure 2.6 Geometry of the Thrust Vectoring Parameters

Once the effective thrust from each engine is obtained, we can easily calculate the moments induced about the center of mass:

$$T_L = -(Ty_l + Ty_r)z_0 + (Tz_r - Tz_l)y_0 \tag{2-47}$$

$$T_M = (Tz_l + Tz_r)x_0 + (Tx_l + Tx_r)z_0 \tag{2-48}$$

$$T_N = -(Tx_r - Tx_l)y_0 - (Ty_l + Ty_r)x_0 \tag{2-49}$$

where x_0, y_0, and z_0 are distances of the engines from the center of mass (see Figure 2.7).

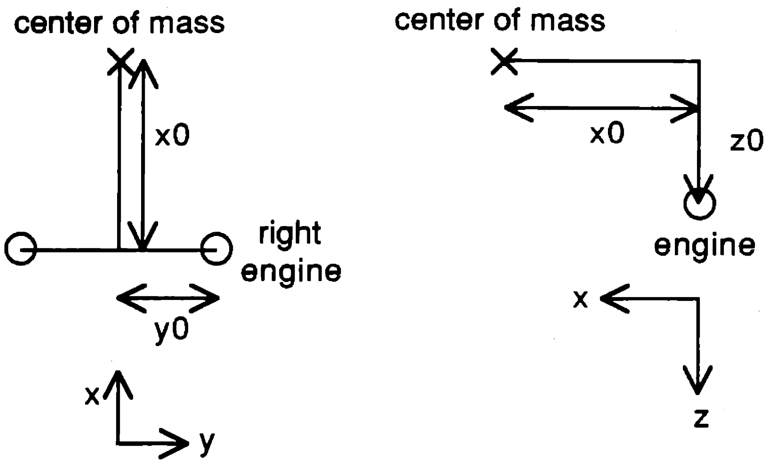

Figure 2.7 Geometry of the Engine Locations

2.6 Linear Model through Perturbation about Equilibrium Point

From the nonlinear state-space model $\dot{x} = f(x,u)$, we can obtain linear models by perturbing the states and controls from their settings at the equilibrium points. Assuming small state and control perturbations (δx and δu), and keeping only the linear terms in the Taylor series expansion, we get,

$$\delta \dot{x} \approx A\delta x + B\delta u \tag{2-50}$$

where

$$A = \frac{\partial f(x,u)}{\partial x} \Big|_{x_0,u_0}, \quad B = \frac{\partial f(x,u)}{\partial u} \Big|_{x_0,u_0}$$

and x_0, u_0 are the states and controls at the equilibrium point.

The elements of the A and B matrices can be approximated by measuring the state derivatives when the system is perturbed one state or one control at a time:

$$(A)_{ij} \approx \delta \dot{x}_i / \delta x_j \qquad (B)_{kl} \approx \delta \dot{x}_k / \delta u_l$$

where $(A)_{ij}$ is the element at the i-th row and j-th column of the matrix A,

$(B)_{kl}$ is the element at the k-th row and l-th column of the matrix B,

$\delta \dot{x}_i$ is the i-th component of the state derivative vector when the j-th component of the state vector is perturbed by δx_j,

$\delta \dot{x}_k$ is the k-th component of the state derivative vector when the l-th component of the control vector is perturbed by δu_l.

2.7 Summary

This chapter provides some basic information about the physical system to be controlled. Derivation of the nonlinear state-space model and the linearized model of the vehicle dynamics are also included. The control designs in Chapter 3 and Chapter 4 will be based on the models developed in this chapter.

CHAPTER 3

INPUT-OUTPUT LINEARIZATION

3.1 Introduction

This chapter describes the nonlinear control design methodology known as input-output linearization, and the general procedure in applying the linearization process to control designs. Specifically, the input-output linearization method is applied to the HARV and the resulting input-output linearized plant is compared to the uncompensated plant. For the nonlinear control design covered in Chapter 4, input-output linearization is performed in an inner-loop compensator, and an outer-loop compensator is then designed around the linearized plant.

3.2 Motivation

Unlike nonlinear control system design, control design for linear systems has been well established and understood. There exist many systematic and powerful linear design techniques such as pole placement, LQR, LQG/LTR, and H_∞ [1, 5, 14, 20, 21]. However, almost all real physical systems are nonlinear in nature. The linear model approximation may prove to be too crude or of limited range of validity, and the resulting robust linear design may be too conservative. Although nonlinear designs are not as well understood, they hold promise for alleviating the conservatism in the linear model based robust designs. Specifically, feedback linearization is a nonlinear design approach that algebraically transforms a nonlinear system into a linear one. It is then hoped that, using this approach, linear models of wide range of validity can be obtained, and thus alleviating the need for gain scheduled linear controllers densely spaced along the operating envelope. The resulting linearized system can then be handled by the powerful linear design methods.

Current techniques for feedback linearization include input-state linearization and input-output linearization [12, 19]. Consider a nonlinear system of the form,

$$\dot{x} = f(x,u)$$

$$y = h(x)$$

In input-state linearization, with a state transformation $z = w(x)$ and an input transformation $u = g(x,v)$, the nonlinear system dynamics is transformed into a linear time-invariant system $\dot{z} = Az + Bv$. One can then use linear techniques to design v.

In input-output linearization, one finds an input transformation $u = g(x,v)$, so that the transformed control input v, and the system output y can be related through a system of linear differential equations. In other words, the input-output relation can be expressed in terms of a transfer function matrix from v to y, and a linear system is established in an input-output sense. Linear techniques can then be used to design v.

In this thesis, we are going to limit our discussion to input-output linearization, which is the technique we use in the inner-loop/outer-loop control design described in Chapter 4. Input-output linearization is performed with the inner-loop controller while the outer-loop controller is designed around the linearized plant using linear control synthesis techniques. The basic idea is to use the inner-loop controller to cancel out the nonlinear effects, and then wrap a linear controller around the linearized plant. Figure 3.1 is a block diagram of the proposed controller structure.

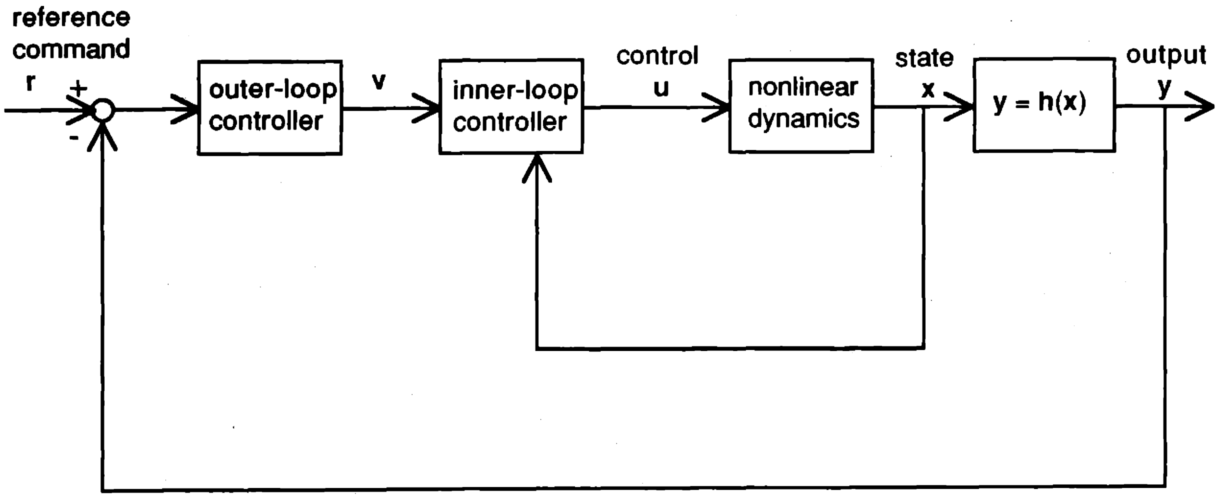

Figure 3.1 Block Diagram of the Inner-Loop/Outer-Loop Controller Structure

The motivation of the inner-loop/outer-loop controller structure also comes from the recent results established in the sensitivity studies of the H_∞ methodology by Craig and Inoue [3, 11]. It was found that the H_∞ methodology is very sensitive to structured uncertainty in the presence of lightly damped poles. In fact, this problem exists for all linear designs attempting approximate plant inversions including both LQG/LTR and H_∞. A technique called inner loop compensation was introduced to desensitize H_∞ designs to structured uncertainty. The idea is to increase the damping of the lightly damped poles in the inner-loop compensation either through full-state feedback, output feedback or other feedback schemes. An H_∞ compensator was then designed around the inner-loop compensated plant. In the studies cited above, the resulting designs were shown to be robust to structured uncertainties.

In fact, the open-loop linear model for the HARV has a pair of lightly damped unstable poles at the trim point of interest (numerical data are shown in Section 3.4). Hence, it makes sense to use the inner-loop/outer-loop structure even if we are doing linear designs. Meanwhile, because of the severe nonlinear characteristics of the vehicle dynamics (like inertial couplings, nonlinear variations of the aerodynamic characteristics with the angle-of-attack), the linear model has a very limited validity. Since we are linearizing around a steady straight level flight, a lot of terms involving the inertial couplings are discarded in the linearized equations of motion (because we set $P = Q = R = \beta = \phi = 0$). The effects of inertial couplings are totally ignored in the linear models. Besides, in the linear models, the aerodynamic characteristics are linearized around the trim values of α selected, but we see in the plots shown in Appendix A that the aerodynamic coefficients are hardly linear with α at all, especially when the airplane is around stall. These compounding effects can result in large modelling errors and a robust linear controller tolerating these errors may prove to be too conservative to provide any performance. Thus, the need to design for high performance has led us to choose the nonlinear approach of input-output linearization, directly incorporating all the dominant nonlinear effects in the inner-loop controller design, while robustness is provided in a more traditional way through the outer-loop feedback linear designs. The resulting structure provides a systematic way of designing high-performance, robust controllers for nonlinear systems. By using the proposed nonlinear approach, we can actually design a controller for flight envelopes covering a large range of α, thus bypassing the traditional patchwork approach of handling the α-nonlinearities through gain scheduling.

3.3 The Input-Output Linearization Process

3.3.1 General Procedure

Consider the multi-input multi-output system of the form

$$\dot{x} = f(x) + \sum_{i=1}^{M} g_i(x)\, u_i \tag{3-1a}$$

$$y_1 = h_1(x)$$

$$\dots \tag{3-1b}$$

$$y_m = h_m(x)$$

where x is the state vector of dimension n,

u_i's ($i = 1, \dots, M$) are control inputs,

y_j's ($j = 1, \dots, m$) are outputs,

f and g_i's are smooth vector fields,

and h_j's are smooth scalar functions.

If we collect the control inputs u_i's into a vector **u**, the outputs y_j's into a vector y, h_j's into a vector **h**, and the vectors g_i's into a matrix G, the state-space description of the system can be written as

$$\dot{x} = f(x) + G(x)\,\mathbf{u} \tag{3-2a}$$

$$y = \mathbf{h}(x) \tag{3-2b}$$

To obtain the input-output linearization of the system described by equations 3-2a and 3-2b, we repeatedly differentiate the outputs y_j (with respect to time) until the inputs appear. Let r_j be the smallest integer such that at least one of the inputs appear in $y_j^{(r_j)}$. After performing this procedure for every output y_j, we get

$$\begin{bmatrix} y_1^{(r_1)} \\ \dots \\ \dots \\ y_m^{(r_m)} \end{bmatrix} = \mathbf{a}(x) + B(x)\,\mathbf{u} \tag{3-3}$$

with

$$\mathbf{a}(x) = \begin{bmatrix} L_f^{r_1} h_1(x) \\ \dots \\ \dots \\ L_f^{r_m} h_m(x) \end{bmatrix}, \quad B(x) = \begin{bmatrix} L_{g_1} L_f^{r_1-1} h_1 & \cdots\cdots & L_{g_M} L_f^{r_1-1} h_1 \\ \dots & \dots\dots & \dots \\ \dots & \dots\dots & \dots \\ L_{g_1} L_f^{r_m-1} h_m & \cdots\cdots & L_{g_M} L_f^{r_m-1} h_m \end{bmatrix}$$

where the Lie derivative $L_f h$ is the directional derivative of h along the direction of the vector f, i.e. $L_f h = \nabla h\, f$, and repeated Lie derivatives are defined recursively

$$L_f^0 h = h$$

$$L_f^i h = L_f(L_f^{i-1} h) = \nabla(L_f^{i-1} h)\, f \qquad \text{for } i = 1, 2, \ldots$$

The scalar function $L_g L_f h(x)$ is simply

$$L_g L_f h = \nabla(L_f h)\, g$$

From equation 3-3, we see that the system can be input-output linearized by choosing **u** such that

$$B(x)\, u = -a(x) + v \tag{3-4}$$

thus obtaining a linear system in an input-output sense from v to y,

$$\begin{bmatrix} y_1^{(r_1)} \\ \cdots \\ \cdots \\ y_m^{(r_m)} \end{bmatrix} = \begin{bmatrix} v_1 \\ \cdots \\ \cdots \\ v_m \end{bmatrix} = v \tag{3-5}$$

If the sum of the r_j's , $r = r_1 + \ldots + r_m$, is smaller than n, part of the dynamics will not be observable under the input-output relation between v and y. This part of the dynamics is known as the internal dynamics associated with the input-output linearization. The stability of the internal dynamics has to be ensured to maintain the effectiveness of the control design based on input-output linearization.

3.3.2 Application to the F18/HARV

The state-space description of the aircraft dynamics is derived in Chapter 2 under equations 2-26 to 2-34. If we follow the procedure outlined in Section 2.5.1 to approximate the aerodynamic coefficients (C_L, C_D, C_M, etc.) by means of the stability derivatives, the state-space description can be turned into the form of equations 3-2a and 3-2b introduced in the previous section, and we can proceed with input-output linearization as described there. In the case of the HARV, the state vector is given by

$x = [V_t, \alpha, \beta, P, Q, R, \theta, \phi, \psi]^T$,

with the state variables as defined in sections 2.3 and 2.4, while the control inputs are given by

$u = [Ail_{sym}, Stab_{sym}, Ail_{asy}, Rud, Stab_{asy}, Tx_{sym}, Tx_{asy}, Ty_l, Ty_r, Tz_l, Tz_r]^T$,

where Ail_{sym}, Ail_{asy} are the symmetric and asymmetric aileron deflections,

$Stab_{sym}$, $Stab_{asy}$ are the symmetric and asymmetric stabilator deflections (actually the perturbations from the trim settings listed in Table 2.1),

Rud is the deflection of the twin rudders acted in unison,

Tx_{sym}, Tx_{asy} are the symmetric and asymmetric thrust in the x-direction,

Ty_l, Ty_r are the y-components of the thrust for the left and right engines,

Tz_l, Tz_r are the z-components of the thrust for the left and right engines,

and the symmetric quantities are defined as the average of the left and right quantities

$X_{sym} = (X_l + X_r)/2$

while the asymmetric quantities are defined as one half of the difference between the left and right quantities

$X_{asy} = (X_r - X_l)/2$

e.g. $Tx_{sym} = (Tx_l + Tx_r)/2$, and $Tx_{asy} = (Tx_r - Tx_l)/2$.

If we go back to the state equations in Chapter 2 (equations 2-32 to 2-34), we see that the Euler angles (θ, ϕ, ψ) are not affected directly by the control inputs. The bottom three rows of the G matrix in

$\dot{x} = f(x) + G(x)\, u$,

are all zero. As a result, the G matrix can be at most of rank six, and we can only control at most six independent outputs.

For the outputs, we are going to choose

$y = [V_t, \alpha, \beta, \theta, \phi, \psi]^T$

implying $h(x) = Cx$, with C a constant matrix.

With the above choice of x, u, and y, we have established a design model for the HARV to apply the input-output linearization method

$$\dot{x} = f(x) + G(x)\,u \tag{3-6a}$$

$$y = Cx \tag{3-6b}$$

The full expressions for f and G are quite lengthy and they are included, together with the expression for C, in Section C.1 of Appendix C which contains the details of the input-output linearizing controller. A note of caution is that the matrix G in equation (3-6a) is a function of the state x only because of the way we approximate the aerodynamic coefficients in Section 2.5.1. The stability derivatives involving the control surfaces (such as $\partial C_M/\partial Stab_{sym}$, $\partial C_N/\partial Rud$, etc.) are assumed to be independent of the control surface deflections. This may not be true if the control surfaces are far from the trim settings. In that case, G is actually G(x,u). However, the mathematics in figuring out the linearizing control u is much simpler if we assume G to be G(x) instead of G(x,u), as we shall see later on in this section. We have to recognize the limitation of the approximation, and be aware of the modelling errors when the controls are not near trim. Hopefully, the outer-loop robust controller should be able to take care of the errors. (Included in Appendix E are plots of the aerodynamic coefficients vs. the control surface deflections. These plots may give us an idea about the extent of the validity of the stability derivative approximations and the extent of the dependency of the G matrix with the controls.)

From the simulation results of the closed loop system presented later in Chapter 5, it seems that the limitation cited above for our approach does not seem to offset the advantages of our nonlinear method very much. The inertial couplings and α-nonlinearities are the most serious shortcomings for the linear models. Errors resulting from the linear control assumption seem to only have minor effects. In fact, the modelling errors resulting from the G(x) assumption can be thought of as issues relating to the gain margins of the system, which are much simpler to deal with in terms of robust control than the hard nonlinearities of inertial couplings and high-α aerodynamics.

Nevertheless, this is only a conjecture. A systematic and quantitative study of the modelling errors resulting from our way of input-output linearization will be needed for better understanding of the issue. Because of time constraints, this study has not been conducted for the research effort reported in this thesis, although it will be a very valuable piece of information for the outer-loop design and for the application of the nonlinear method to flight control systems in general. This study is strongly suggested for future research efforts.

In carrying out the linearization process, we need to differentiate θ, ϕ, and ψ twice for the inputs to appear, while V_t, α, and β only need to be differentiated once. After the differentiation process is performed, we obtained

$$\begin{bmatrix} \dot{V}_t \\ \dot{\alpha} \\ \dot{\beta} \\ \ddot{\theta} \\ \ddot{\phi} \\ \ddot{\psi} \end{bmatrix} = \mathbf{a}(\mathbf{x}) + \mathbf{B}(\mathbf{x})\,\mathbf{u} \tag{3-7}$$

The full expressions for $\mathbf{a}(\mathbf{x})$ and $\mathbf{B}(\mathbf{x})$ are included in Section C.2 in Appendix C. For subsequent results presented in this chapter and the later chapters, the numerical values used for $\mathbf{a}(\mathbf{x})$ and $\mathbf{B}(\mathbf{x})$ are based on the nonlinear model of the vehicle dynamics (model 1) described in Section 2.5.1, which approximates the aerodynamic coefficients through linear interpolations of the stability derivatives data set.

The next step is to find the control $\mathbf{u}$ such that $\mathbf{B}(\mathbf{x})\,\mathbf{u} = -\mathbf{a}(\mathbf{x}) + \mathbf{v}$. Since $\mathbf{B}$ is a rectangular matrix (it is of dimension 6 x 10), the problem is underconstrained and there are more than one solutions for this matrix equation. A common trick is to solve the problem in a least-squares sense by picking the $\mathbf{u}$ with the minimum weighed norm $\mathbf{u}^T W \mathbf{u}$ among the solutions satisfying equation 3-4. In other words, we are turning the problem into a constrained minimization

$$\min (\mathbf{u}^T W \mathbf{u}) \quad \text{with respect to } \mathbf{u}$$

subject to the constraint

$$a(x) + B(x)\,\mathbf{u} = v$$

In some sense, the weighted norm $\mathbf{u}^T W \mathbf{u}$ is a measure of the control effort. By minimizing $\mathbf{u}^T W \mathbf{u}$, we are trying to pick the **u** that achieves the performance objective with minimum effort. The weighting matrix W also lets us address the relative cost we attach to the various control inputs. Using the method of Largrange multipliers, a close form solution to the minimization problem is given by

$$\mathbf{u} = [W^{-1}B^T(BW^{-1}B^T)^{-1}]\,(-a + v) \tag{3-8}$$

A reasonable choice for the weighting matrix is a diagonal matrix with the diagonal elements being the square of the inverse of the maximum values allowed for each input, i.e. $W = \text{diagonal}(1/(u_{1max})^2 \ldots 1/(u_{Mmax})^2)$. Numerical information about the W matrix can be found in Section C.3 in Appendix C. One minor point about the control **u** is that we are using the x, y, and z components of the engine thrusts to represent the propulsive control inputs instead of the physical propulsive controls of engine throttles (which is related to the magnitude of the engine thrusts T_l, and T_r) and the orientation of the thrust vectoring vanes (the angles σ and η described in Section 2.5.2). We can easily calculate the corresponding physical propulsive controls using the relations established in equations 2-41 to 2-46 in Section 2.5.2.

The resulting linearized system is of the form,

$$\dot{V}_t = v_1 \tag{3-9}$$

$$\dot{\alpha} = v_2 \tag{3-10}$$

$$\dot{\beta} = v_3 \tag{3-11}$$

$$\ddot{\theta} = v_4 \tag{3-12}$$

$$\ddot{\phi} = v_5 \tag{3-13}$$

$$\ddot{\psi} = v_6 \tag{3-14}$$

or, in state-space form,

$$\dot{z} = A_l z + B_l v \tag{3-15}$$

$$y = C_l z \tag{3-16}$$

with

$$A_l = \begin{bmatrix} 0&0&0&0&0&0&0&0&0 \\ 0&0&0&0&0&0&0&0&0 \\ 0&0&0&0&0&0&0&0&0 \\ 0&0&0&0&1&0&0&0&0 \\ 0&0&0&0&0&0&0&0&0 \\ 0&0&0&0&0&0&1&0&0 \\ 0&0&0&0&0&0&0&0&0 \\ 0&0&0&0&0&0&0&0&1 \\ 0&0&0&0&0&0&0&0&0 \end{bmatrix}, \; B_l = \begin{bmatrix} 1&0&0&0&0&0 \\ 0&1&0&0&0&0 \\ 0&0&1&0&0&0 \\ 0&0&0&0&0&0 \\ 0&0&0&1&0&0 \\ 0&0&0&0&0&0 \\ 0&0&0&0&1&0 \\ 0&0&0&0&0&0 \\ 0&0&0&0&0&1 \end{bmatrix}$$

$$C_l = \begin{bmatrix} 1&0&0&0&0&0&0&0&0 \\ 0&1&0&0&0&0&0&0&0 \\ 0&0&1&0&0&0&0&0&0 \\ 0&0&0&1&0&0&0&0&0 \\ 0&0&0&0&0&1&0&0&0 \\ 0&0&0&0&0&0&0&1&0 \end{bmatrix}$$

and

$$z = [V_t, \alpha, \beta, \theta, \dot{\theta}, \phi, \dot{\phi}, \psi, \dot{\psi}]^T$$

$$y = [V_t, \alpha, \beta, \theta, \phi, \psi]^T$$

$$v = [v_1, v_2, v_3, v_4, v_5, v_6]^T$$

Since the relative degree of the linearized system (the sum of the r_j's) is equal to the order of the original nonlinear system ($n = 9$), the system has been fully linearized and there is no internal dynamics associated with the linearization.

After seeing the derivation of the linearizing control, one may now understand why G is assumed to have the form G(x) instead of G(x,u), which results in B(x) instead of B(x,u). If **B** is of the form B(x,**u**), equation 3-4 will be nonlinear in **u**, and there is no close form solution for the nonlinear equations in general. One has to resort to iterative methods for solving the linearizing control, which complicates the situation with issues of stability and convergence of the iterative schemes. In fact, no current nonlinear inversion scheme includes the control dependency in the G matrix as a result of the above difficulty.

Research on alternative approaches may be able to avoid or solve the difficulty, and directly incorporate the control dependency into the controller design. However, as suggested earlier, the modelling errors caused by the exclusion of the control dependency in the G matrix seem to be benign enough to be handled through an outer-loop feedback controller. In that case, all the complexity related to the inclusion of the control dependency may not seem to be worthwhile.

3.4 Comparison of the Inner-Loop Compensated Plant to the Uncompensated Plant

For the purpose of comparison with the input-output linearized system, a linear model of the uncompensated plant is obtained as discussed in Section 2.6 at the trim point corresponding to a straight level flight at

$h = 15000$ ft, $V_t = 211.231$ ft/sec (Mach 0.199771), and $\alpha = 35^\circ$.

The numerical data for the linear model can be found in Appendix D. Upon analysis of its eigenstructure, it is found that there are no transmission zeros, and there are four pairs of complex poles and a real pole at the origin. The pole at the origin corresponds to the lateral mode of "heading displacement", in which only ψ differs from zero and is constant in time. This is due to the fact that the airplane does not seek any particular heading. When the airplane is disturbed, after recovery of a straight level flight, it will in general have some heading other than the original heading before the disturbance. Two of the complex pole pairs correspond to decoupled longitudinal motion since only longitudinal variables (V_t, α, θ, Q) are involved in the eigenvectors. One of the longitudinal pole pairs is actually unstable and very lightly damped. The remaining complex pole pairs correspond to modes where the longitudinal and lateral motions are coupled together. The poles of the linearized model for the uncompensated plant are summarized in Table 3.1.

Table 3.1 Poles of the Linearized Model for the Uncompensated Plant at Trim Point h = 15000 ft, V_t = 211.231 ft/sec, $\alpha = 35°$

Pole Location	Coupling	Damping Ratio ζ	Natural Frequency
0.0063±0.1406j	Decoupled Long. Mode	-0.0448	0.1407
-0.2951±0.3444j	Decoupled Long. Mode	0.6507	0.4535
-0.1301±0.1953j	Coupled Long./Lat. Mode	0.5544	0.2347
-0.4240±0.4127j	Coupled Long./Lat. Mode	0.7166	0.5917
0.0000	Decoupled Lat. Mode	-	-

(Long. = Longitudinal, Lat. = Lateral)

At first glance, we see that this is a very tough trim point for control design. The system is unstable and the lightly damped pole pair would be extremely difficult for linear control designs like H_∞ and LQG/LTR [3, 11]. Besides, the longitudinal and lateral modes are coupled together. An integrated controller has to be designed for both the longitudinal and lateral motions.

Looking back at the input-output linearized system, we see that the nominal system described by equations 3-9 to 3-14, is relatively simple with all the poles located at the origin and all the channels decoupled. One can actually use classical single-input–single-output (SISO) control design techniques for each decoupled subsystem. However, one has to bear in mind that the input-output linearization will not be perfect because of parameter uncertainties and other modelling errors. In order to get some feeling about how good the feedback linearization is, a linear model of the inner-loop compensated plant is obtained through perturbation around the same trim point as the linear model of the uncompensated plant. If we choose the state vector z, control vector v, and output vector y as defined in equations 3-15 and 3-16, the state-space description of the inner-loop compensated plant can be written generally as

$$\dot{z} = f(z,v) \qquad (3\text{-}17a)$$

$$y = Cz \qquad (3\text{-}17b)$$

We are using f(z,v) to indicate that $\dot{z}$ is in general a nonlinear function of both the states and controls. C is a constant matrix relating the states and outputs we choose for the state space representation. Perturbing around the trim point

$$z_0 = [211.231\ \text{ft/sec}, 35^\circ, 0^\circ, 35^\circ, 0^\circ/\text{sec}, 0^\circ, 0^\circ/\text{sec}, 0^\circ, 0^\circ/\text{sec}]^T$$

$$v_0 = [0\ \text{ft/sec}^2, 0^\circ/\text{sec}, 0^\circ/\text{sec}, 0^\circ/\text{sec}^2, 0^\circ/\text{sec}^2, 0^\circ/\text{sec}^2]^T$$

the linear model of the inner-loop compensated plant is of the form

$$\dot{z} = A\ \delta z + B\ \delta v + \mathbf{d} \tag{3-18a}$$

$$y = Cz \tag{3-18b}$$

where

$$A = \frac{\partial f(z,v)}{\partial z}\Big|_{z_0,v_0},\quad B = \frac{\partial f(z,v)}{\partial v}\Big|_{z_0,v_0},\quad \mathbf{d} = f(z_0,v_0)$$

(**d** is an offset vector which results from the imperfect linearization: $\dot{z}$ is nonzero even if both z and v are zero)

and

δz is the perturbation of the state vector from the trim point, i.e. $\delta z = z - z_0$,

δv is the perturbation of the control vector from the trim point, i.e. $\delta v = v - v_0$.

Since the exact form of f with the linearizing control is not known to us, the linear model we are getting in the form of 3-18a and 3-18b is purely a numerical one. The values of the A and B matrices are obtained by numerically perturbing the states and controls one at a time. **d** is obtained by setting $z = v = 0$, and the resulting $\dot{z}$ is then noted for **d**.

The matrix C in equation 3-18b is the same as C_l in equation 3-16 since we use the same definitions for z and y here. Because the linearization is not perfect, the matrices A and B will not be the same as A_l and B_l in equation 3-15, and **d** will be nonzero. Cross-coupling terms will also appear in the A and B matrices. The numerical values of the A and B matrices, and the **d** vector can be found in Appendix D. An interesting observation is that all the poles of the linear model of the inner-loop compensated system are real. The poles are located at s = 0, 0.0002, 0.0311, 0.1011, 0.2401, 13.4165, -0.0383, -0.5180, and -0.5578. We see that the poles are no longer all at the origin, but scatter around the neighborhood of s = 0, with the exceptional case of the one at s = 13.4165, which corresponds to an unstable lateral mode. Meanwhile, the eigenvectors all contain components from several variables, but they still decouple roughly into eigenvectors for longitudinal modes and eigenvectors for lateral modes, except for the one which contains all the state variables. There are also no transmission zeros. These results are not totally unexpected since we know there is going to be some departure from the nominal input-output linearized system because of the imperfect linearization. A robust outer-loop controller is needed to overcome this departure while accomplishing satisfactory performance for command following. The singular value plots for the linear models of the uncompensated system and the inner-loop compensated system are shown in Figure 3.2 and Figure 3.3. In obtaining the singular values, the following scaling factors are used for the uncompensated system.

For the outputs: 6 ft/sec for V_t,
1 deg for α, θ, and ϕ,
0.2 deg for β,
and 0.5 deg for ψ.

For the controls: 14 deg for the stabilators,
30 deg for the rudders,
25 deg for the ailerons,
30 deg for the thrust vectoring,
and 12 deg for the throttles.

Meanwhile, for the inner-loop compensated system, the scaling factors for the outputs are the same as above while the scaling factors for the controls are as follows:

6 ft/sec^2 for v_1,
1 deg/sec for v_2,
0.2 deg/sec for v_3,
1 deg/sec^2 for v_4 and v_5,
and 0.5 deg/sec^2 for v_6.

Looking at Figure 3.2 and Figure 3.3, we notice that the inner-loop compensated system is much smoother in terms of the frequency response of the singular values, in contrast to the sharp peaks occurring around $\omega = 0.1$ rad/sec in the singular value plot of the uncompensated system. One can definitely tell that Figure 3.3 is obtained from a compensated system instead of a crude physical system. The singular value plot represents a lumped and smooth system with no singular characteristics which are problematic for plant inversions. In spite of the imperfect input-output linearization, the inner-loop compensated system is a much better conditioned system to do linear control designs.

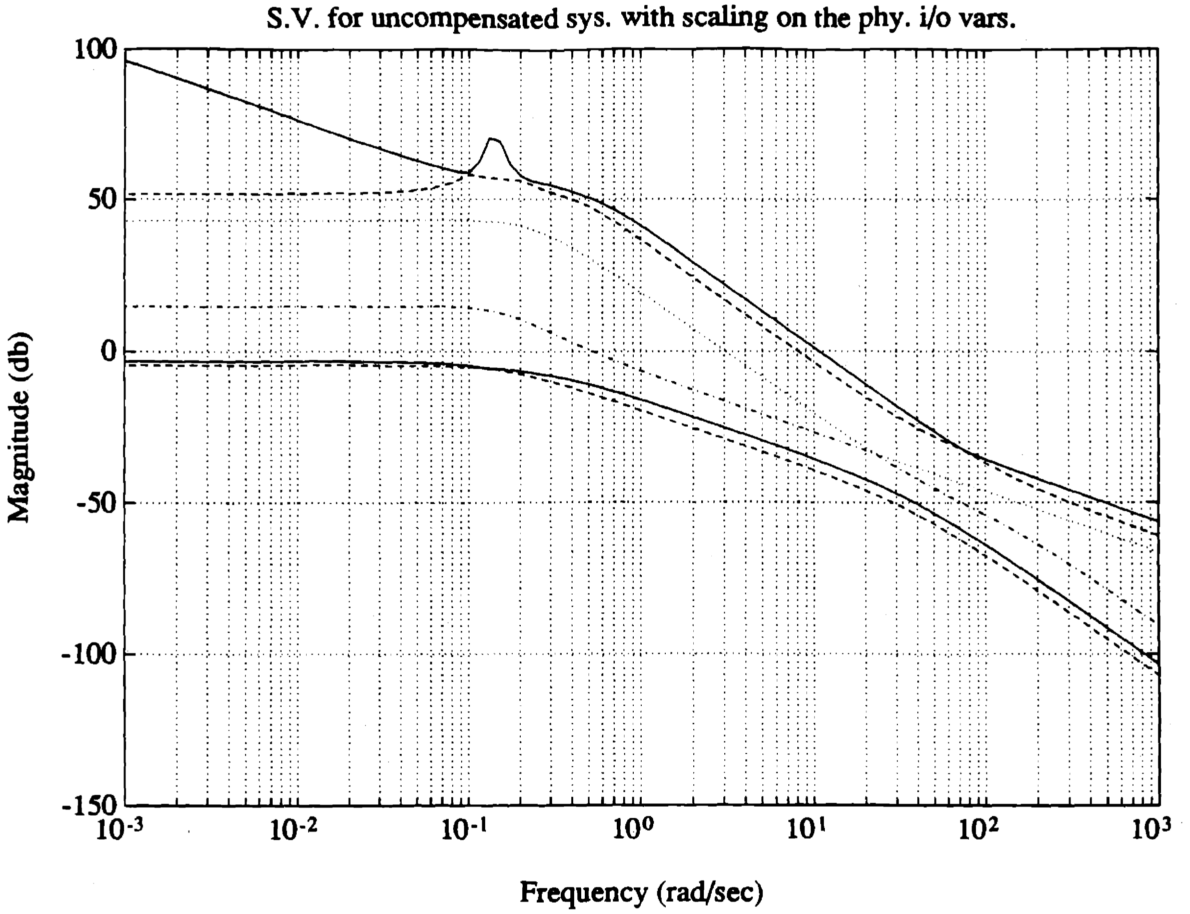

Figure 3.2 Singular Values of the Uncompensated System

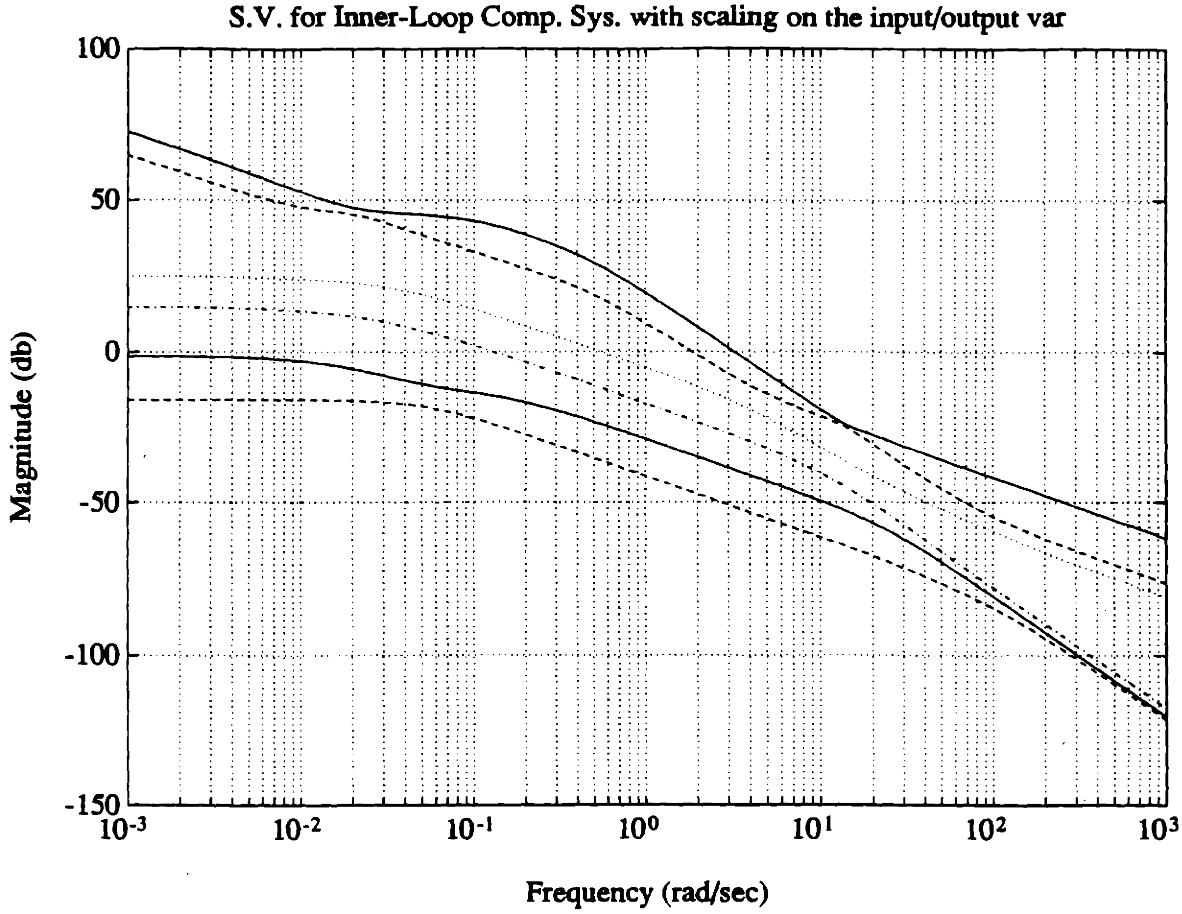

Figure 3.3 Singular Values of the Inner-Loop Compensated System

3.5 Summary

The input-output linearization method is described briefly in this chapter. It forms the basis of the nonlinear control design (inner-loop/outer-loop controller) in Chapter 4. The linearization method is applied to the HARV and implemented in the inner-loop compensator of the inner-loop/outer-loop controller structure. A comparison of the feedback linearized system with the (uncompensated) Taylor series linearized system is also presented to reveal the relative ease of designing the outer-loop controller around the input-output linearized system over designing around the linear model of the uncompensated system.

CHAPTER 4

CONTROLLER DESIGN

4.1 Introduction

As stated in Chapter 1, the goal of the thesis is to explore the nonlinear control design alternatives for high-α flights, as distinct from the traditional linear multi-input–multi-output (MIMO) methods such as LQG/LTR and H_∞. In this chapter, a linear design using the LQG/LTR method is first obtained along the approach of Voulgaris in [22] (with the extension of purely longitudinal motion to both longitudinal and lateral motions). This design based on a linear model will serve as a baseline for comparison with the nonlinear designs, namely the inner-loop/outer-loop controller structure with input-output linearization, based on the nonlinear model of the vehicle dynamics derived in Chapter 2. The controller designs described in this chapter are compared with one another later in Chapter 5, by "hooking" them up with the full-scale nonlinear simulation model provided by NASA/Langley for the HARV. Robustness and performance are thus directly checked on the "real" plant, complete with modelling errors that were not included in the design nonlinear model.

4.2 Design Based on the Linear Model (LQG/LTR)

4.2.1 Selection of Trim Point and the Corresponding Linear Model

The linear model described in Section 3.4 is obtained at a trim point corresponding to a straight level flight at an altitude of 15,000 ft and an angle of attack of 35°. This trim point is chosen for its severe α-nonlinearity since the stall angle is approximately at $\alpha = 40°$. The aerodynamic characteristics change abruptly around stall with all the nonlinear aerodynamic phenomena mentioned in Chapter 1. Besides, this trim point is unstable, and requires active control for stability. Once again, the reader can refer to Appendix D for the numerical values of the A, B, and C matrices and the definitions of the state, output, and control vectors for the linear model. The same set of output variables are chosen as in the input-output linearization process applied to the HARV in Section 3.3.2, so that we can compare the tracking response of the linear and nonlinear designs directly.

Since the LQG/LTR method is based on the singular values of the loop transfer function $T(s) = C\Phi(s)BK(s)$,[1] we have to scale the inputs and outputs appropriately for meaningful comparison of the input and output quantities with different units of measurements, and meaningful results for the singular values. For the trim point we have chosen, the scaling factors used for the outputs are 6 ft/sec for V_t, 1 deg for α, 1/5 deg for β, 1 deg for ϕ, 1 deg for θ, and 1/2 deg for ψ. The scaling of the inputs is taken care of through the pseudo-control approach described in the next section, which handles the control redundancy of the system.

4.2.2 Design of the LQG/LTR Compensator

The LQG/LTR design procedure [1, 20] outlined here is very similar to the approach used by Voulgaris in [22], except for the inclusion of both longitudinal and lateral motions instead of just purely longitudinal motion as in [22]. The pseudo-control approach developed in [22] is followed closely here to handle the control redundancy of the system. Dynamic augmentation is also undertaken to add integrators in each input channel in order

---

[1] K(s) is the transfer function matrix of the LQG/LTR compensator and $\Phi(s) = (sI - A)^{-1}$.

to achieve zero steady state error to constant commands or disturbances. Since the design procedure follows closely the steps outlined in [22], step-by-step details of the general LQG/LTR methodology will not be presented in the following sections. Readers who are unfamiliar with the LQG/LTR methodology can consult [1, 20, 22] for the step-by-step details.

4.2.2.1 Pseudo-Control Approach for the Control Redundancy of the System

Examining the structure of the linear model as shown in Section D.2 of Appendix D, we see that the B matrix has a rank of six, which suggests that we can control six output variables independently. With the six outputs defined by equation D-5 (in Appendix D) and the ten control inputs defined by equation D-4 (in Appendix D), we have gotten ourselves a rectangular MIMO system with more inputs than outputs. The idea of the pseudo-control approach is to convert the system to a square one by designing around a pseudo system $G_v(s)$ with fictitious control input $v \in R^{6x1}$ instead of the actual physical control input $u \in R^{10x1}$. Since the rank of the B matrix is six, the input term Bu in the state space description of the linear model can be replaced by $B_v v$, where the column space of B_v is the same as that of B. Taking into account the particular structure of B,

$$B = \begin{bmatrix} B_1 \\ 0_{3x10} \end{bmatrix} \qquad (4\text{-}1)$$

with $\text{rank}(B_1) = 6$.

A convenient choice of B_v is

$$B_v = \begin{bmatrix} I_{6x6} \\ 0_{3x6} \end{bmatrix} \qquad (4\text{-}2)$$

As a result, the state space description of the pseudo system with the fictitious input v is given by

$$\dot{x} = Ax + B_v v \qquad (4\text{-}3a)$$

$$y = Cx \tag{4-3b}$$

with B_v given by equation 4-2.

With $v \in R^{6x1}$ and $y \in R^{6x1}$, the pseudo system is clearly a square system, and we can proceed with the design as in the case of a regular square system. The LQG/LTR compensator designed for the pseudo system will be denoted by $K_v(s)$. On the other hand, we still have to figure out a way to transform the fictitious input v into the physical input **u**. We know that v and **u** are related by $B\mathbf{u} = B_v v$. From equations 4-1 and 4-2, this can be replaced by

$$B_1 \mathbf{u} = v \tag{4-4}$$

Since B_1 is rectangular ($B_1 \in R^{6x10}$), there will be infinitely many vectors **u** satisfying equation 4-4 for a given v. One way to solve the problem is to pick the **u** that satisfies equation 4-4 while minimizing the cost function $J = \mathbf{u}^T W \mathbf{u}$, where W is a positive definite weighting matrix. The close form solution of the minimization problem is given by

$$\mathbf{u} = Tv \tag{4-5}$$

where $T = W^{-1}B_1{}^T(B_1W^{-1}B_1{}^T)^{-1}$ (4-6)

A reasonable choice for the W matrix is a diagonal matrix with its diagonal elements corresponding to the inverses of the maximum values allowed for the control in each input channel. In this way, the scaling of the control inputs mentioned in Section 4.2.1 are actually handled through the weights assigned to the diagonal elements of the W matrix. Finally, the actual LQG/LTR compensator is given by

$$K(s) = TK_v(s) \tag{4-7}$$

4.2.2.2 LQG/LTR Design for the Pseudo System

With the pseudo-control approach outlined in the previous section, the LQG/LTR design is applied on the pseudo system $G_v(s)$ instead of the actual system $G_0(s)$.

However, we are going to add an integrator to each input channel to achieve zero steady state error for constant commands or disturbance. Therefore, the design plant model is going to include both the dynamics of the augmented integrators and the pseudo system. Figure 4.1 is an illustration of the dynamic augmentation with integrators for the design plant model.

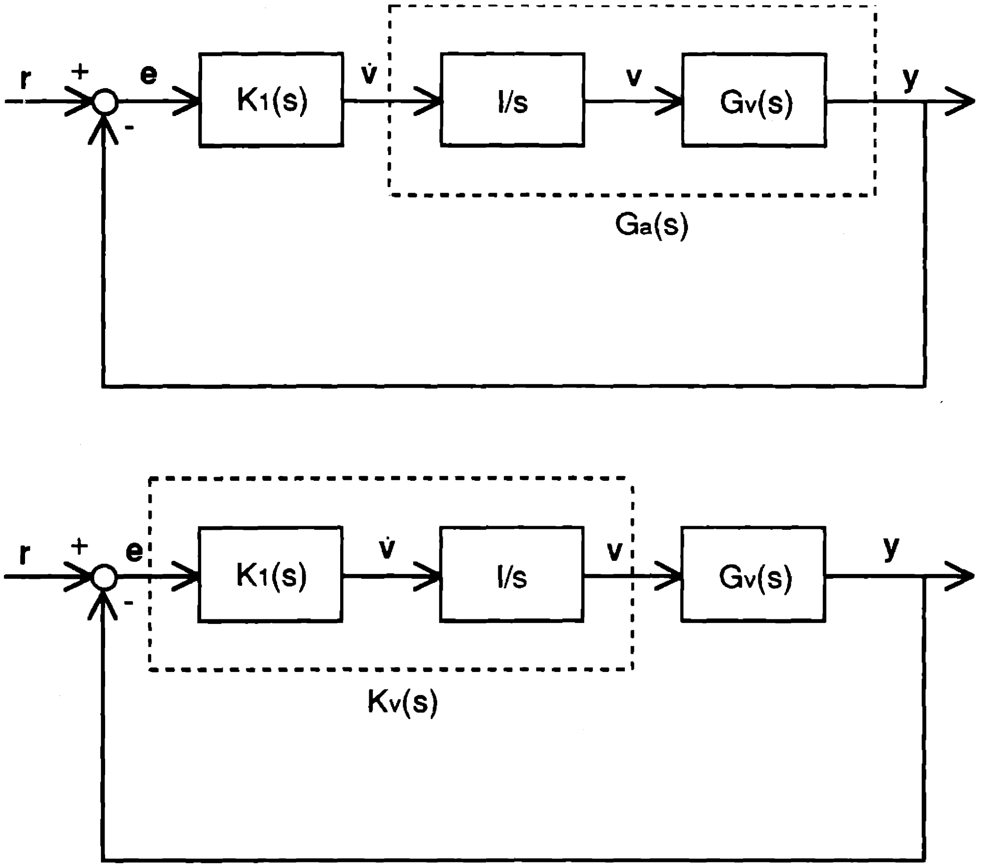

Figure 4.1 Augmentation with Integrators

The state space description of the augmented system $G_a(s)$ is given by

$$\dot{x}_a = A_a x_a + B_a u_a \tag{4-8a}$$

$$y_a = C_a x_a \tag{4-8b}$$

with

$$A_a = \begin{bmatrix} 0 & 0 \\ B_v & A \end{bmatrix}, \quad B_a = \begin{bmatrix} I \\ 0 \end{bmatrix}, \quad C_a = \begin{bmatrix} 0 & C \end{bmatrix}$$

$$x_a = \begin{bmatrix} v \\ x \end{bmatrix}, \quad u_a = v, \quad y_a = y.$$

Augmentation with integrators at the plant inputs allows the designer extra freedom to do loop shaping and to match singular values at both low and high frequencies. On designing the target loop, we can partition the design parameter matrix L as:

$$L = \begin{bmatrix} L_l \\ L_h \end{bmatrix} \tag{4-9}$$

Thus,

$$C_a(sI-A_a)^{-1}L = C(sI-A)^{-1}B_vL_l/s + C(sI-A)^{-1}L_h \tag{4-10}$$

With the specific structure of A,

$$A = \begin{bmatrix} A_1 & 0_{8x1} \\ A_2 & 0 \end{bmatrix} \tag{4-11}$$

this becomes

$$C_a(sI-A_a)^{-1}L = C\begin{bmatrix} (sI-A_1)^{-1} & 0_{8x1} \\ A_2(sI-A_1)^{-1}(1/s) & 1/s \end{bmatrix}B_vL_l(1/s) + C\begin{bmatrix} (sI-A_1)^{-1} & 0_{8x1} \\ A_2(sI-A_1)^{-1}(1/s) & 1/s \end{bmatrix}L_h \tag{4-12}$$

As s=jω→0, we get

$$C_a(sI-A_a)^{-1}L \approx -C\begin{bmatrix} I_{8x8} \\ A_2/s \end{bmatrix}A_1^{-1}B_{v1}L_l(1/s) \tag{4-13}$$

where

$$B_v = \begin{bmatrix} B_{v1} \\ 0_{1x6} \end{bmatrix} \tag{4-14}$$

and as s=jω→∞,

$$C_a(sI-A_a)^{-1}L \approx CL_h/s \tag{4-15}$$

Choosing

$$L_l = \left(C\begin{bmatrix} I_{8x8} \\ A_2/s \end{bmatrix}A_1^{-1}B_{v1}\right)^{-1}, \text{ with } s=j\omega\rightarrow 0 \tag{4-16}$$

and $$L_h = C^T(CC^T)^{-1} \tag{4-17}$$

we get $C_a(sI-A_a)^{-1}L \approx I/s$, as s=jω→0, and s=jω→∞.

From the Kalman frequency domain equality

$$\sigma_i[I + G_{KF}(s)] = \sqrt{1 + (1/\mu)\sigma_i^2[C_a(sI - A_a)^{-1}L]} \qquad (4\text{-}18)$$

where the Kalman filter loop transfer function matrix is given by

$$G_{KF}(s) = C_a(sI-A_a)^{-1}H \qquad (4\text{-}19)$$

so for $s=j\omega \rightarrow 0$, and $s=j\omega \rightarrow \infty$,

$$\sigma_i[G_{KF}(j\omega)] \approx (1/\mu^{1/2})/\omega \qquad (4\text{-}20)$$

With the choice of L_l and L_h, we have managed to match the singular values of the target filter loop at both low and high frequencies.

Using $\mu = 1/4$ (for a crossover frequency of 2 rad/sec), and $s = j(10^{-6})$ for the calculation of L_l, we obtain the target Kalman filter loop by solving the Filter Algebraic Riccati Equation

$$A_a\Sigma + \Sigma A_a^T + LL^T - (1/\mu)\Sigma C_a^T C_a \Sigma = 0 \qquad (4\text{-}21)$$

The Kalman filter gain is given by,

$$H = (1/\mu)\Sigma C_a^T \qquad (4\text{-}22)$$

and the Kalman filter loop transfer function matrix is given by equation 4-19.

The numerical value of H can be found in Appendix F. The resulting singular value plot of the target loop transfer function is shown in Figure 4.2.

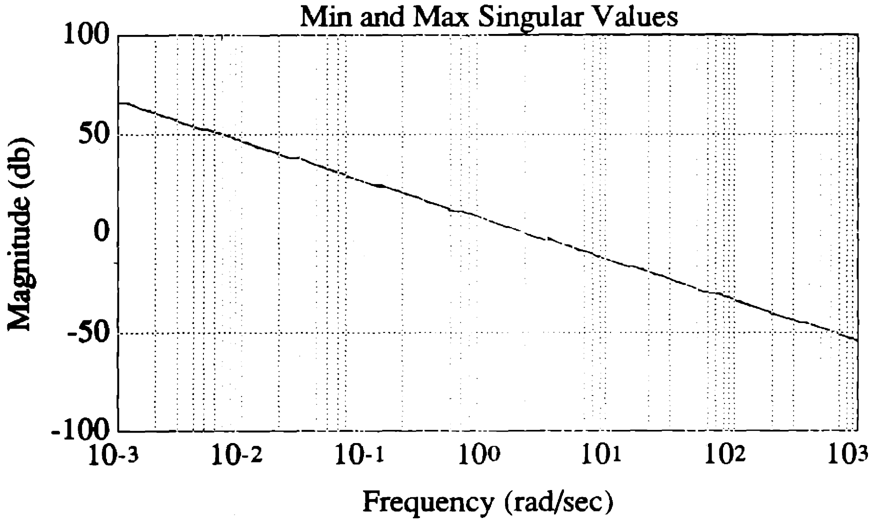

Figure 4.2 Singular Value Plot of the Target Loop of the Linear Design

In the loop transfer recovery step, ρ is chosen to be 10^{-8} to recover the target loop up to a decade above the crossover frequency. The gain matrix G in the LQG/LTR controller is computed from the Control Algebraic Riccati Equation

$$KA_a + A_a^TK + C_a^TC_a - (1/\rho)KB_aB_a^TK = 0 \qquad (4\text{-}23)$$

and $$G = (1/\rho)B_a^TK \qquad (4\text{-}24)$$

The numerical value of the G matrix can be found in Appendix F, and the singular value plot of the recovered loop is shown in Figure 4.3

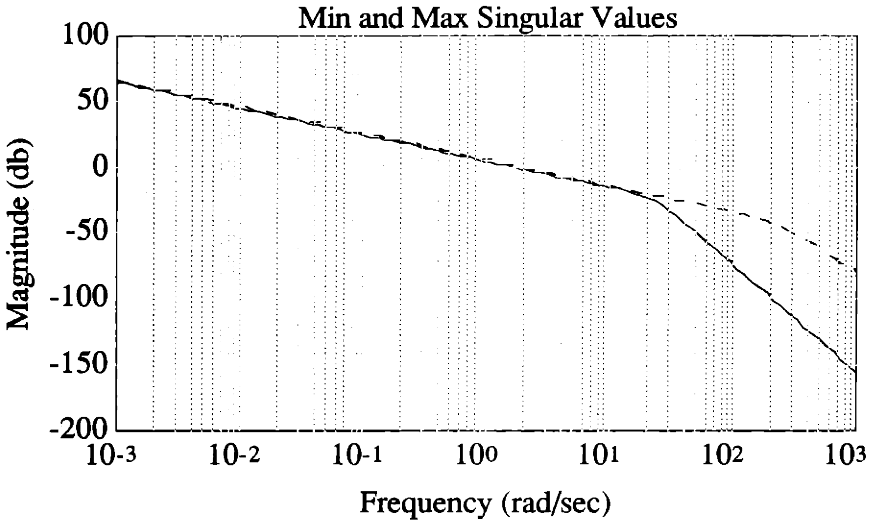

Figure 4.3 Singular Value Plot of the Recovered Loop of the Linear Design

By absorbing the integrators in the plant inputs into the LQG/LTR controller, the state space description of the LQG/LTR controller $K_v(s)$ is given by

$$\dot{z} = (A_a - B_aG - HC_a)z - He \qquad (4\text{-}25)$$

$$\dot{v} = -Gz \qquad (4\text{-}26)$$

The physical control is given by **u** = Tv, with T given by equation 4-6.

4.2.3 Step Responses of the LQG/LTR Linear Design Simulated with Nominal Linear Model

Time simulations for unit (in scaled output units) step responses were performed using the linear nominal model. The step response (in scaled output units) for unit command in V_t is shown in Figure 4.4. The step responses for unit command in α, β, and θ look very similar to the one shown for V_t.

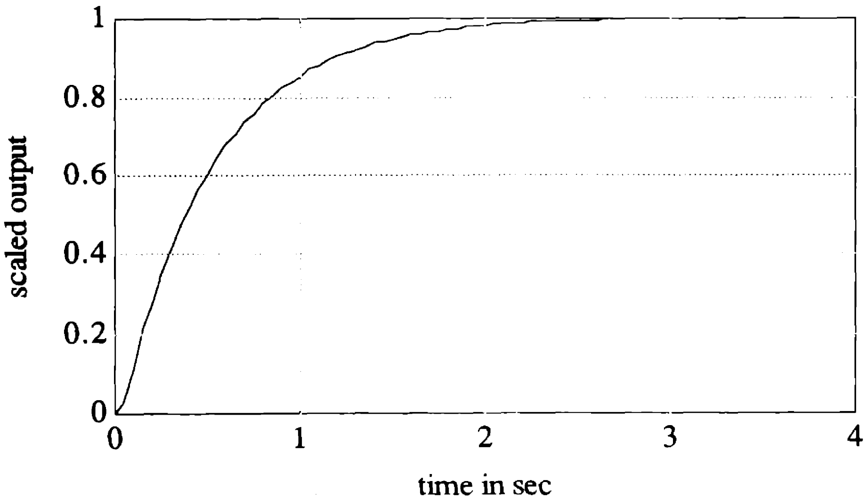

Figure 4.4 Step Response for Unit Command in V_t for the Linear Design (Simulated with Nominal Linear Model)

The step response for unit command (in scaled unit) in ψ shows a little bump for ϕ initially, indicating a little coupling between ψ and ϕ. The step response is shown in Figure 4.5. The step response for unit command (in scaled unit) in ϕ looks similar to Figure 4.5, but with the roles of ψ and ϕ interchanged.

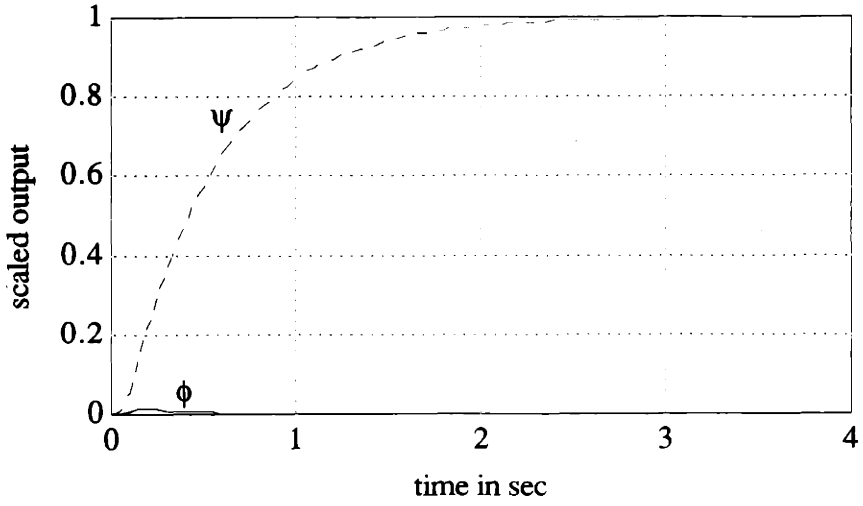

Figure 4.5 Step Response for Unit Command in ψ for the Linear Design (Simulated with Nominal Linear Model)

With the weighting matrix for the control chosen to be
$W = \text{diag}(1/14^2, 1/14^2, 1/30^2, 1/30^2, 1/25^2, 1/25^2, 1/30^2, 1/30^2, 1/12^2, 1/12^2)$,
the control actions corresponding to the unit step commands are shown in Figure 4.6 to Figure 4.11.

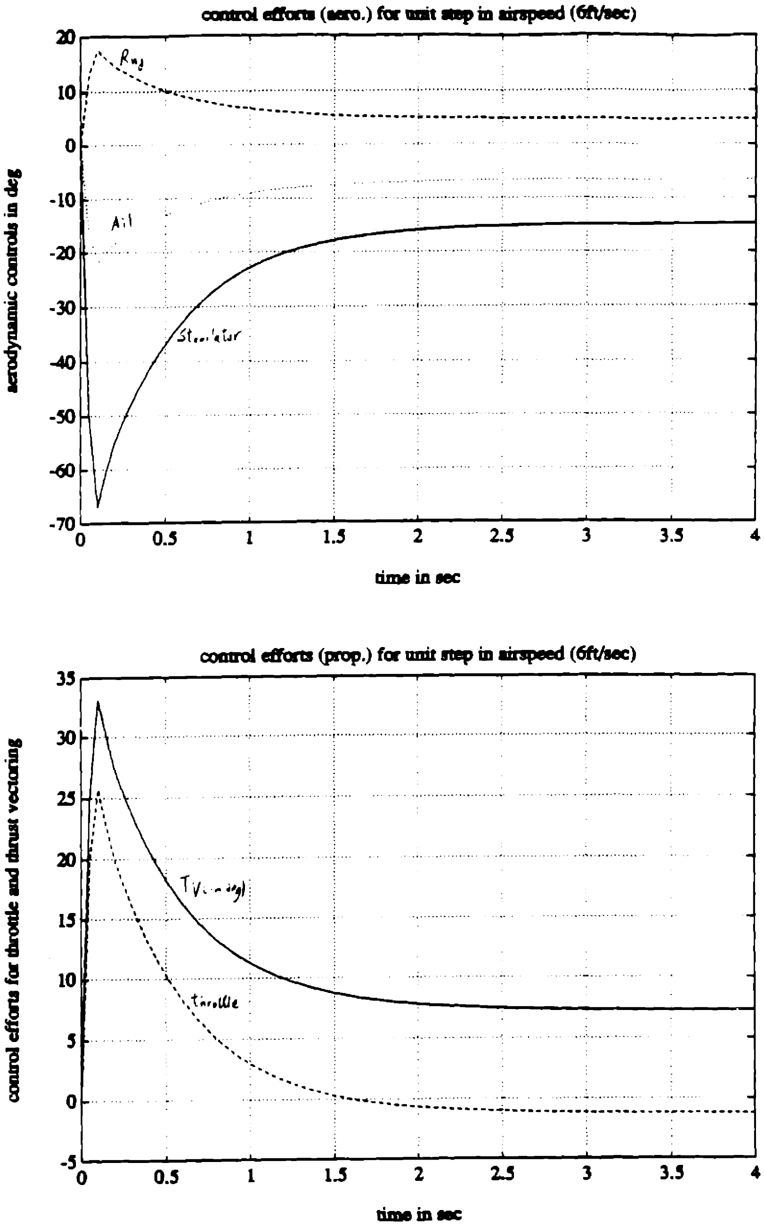

control efforts (aero.) for unit step in airspeed (6ft/sec)

control efforts (prop.) for unit step in airspeed (6ft/sec)

Figure 4.6 Control Actions for Unit Step Command in V_t (6 ft/sec)

for the Linear Design

(Simulated with Nominal linear Model)

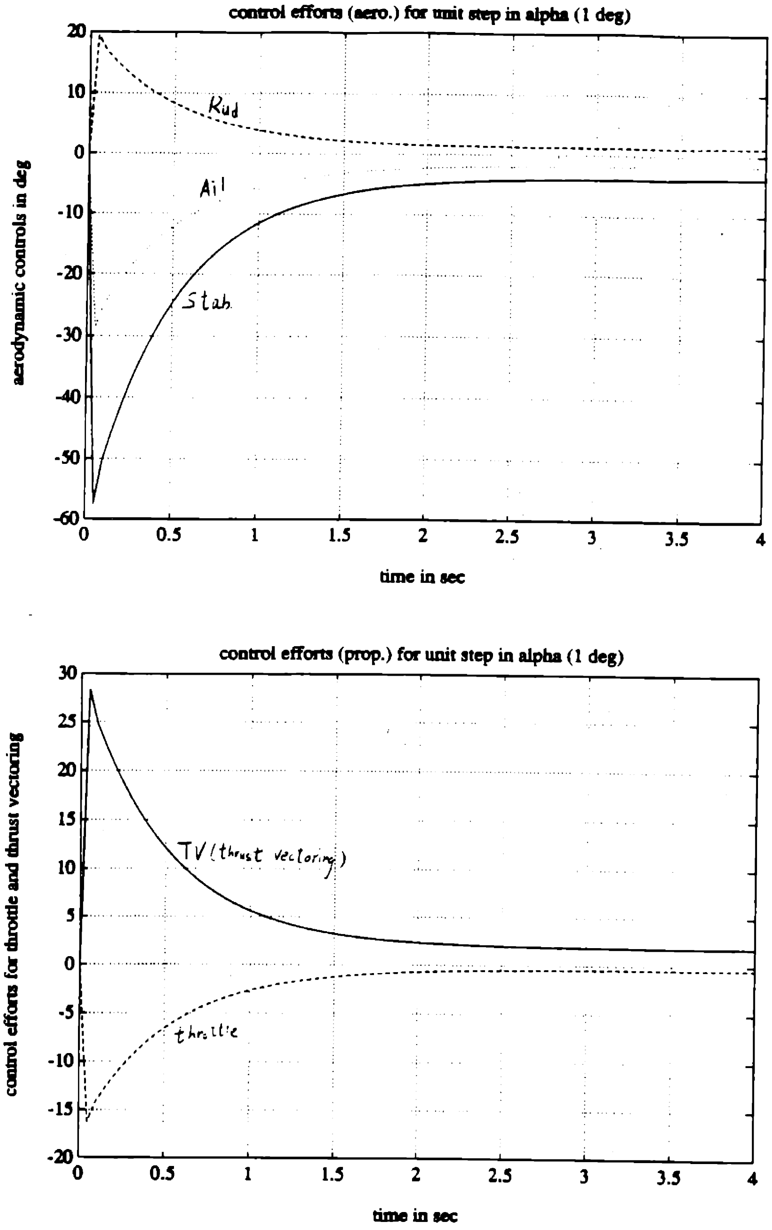

Figure 4.7 Control Actions for Unit Step Command in α (1 deg)

for the Linear Design

(Simulated with Nominal Linear Model)

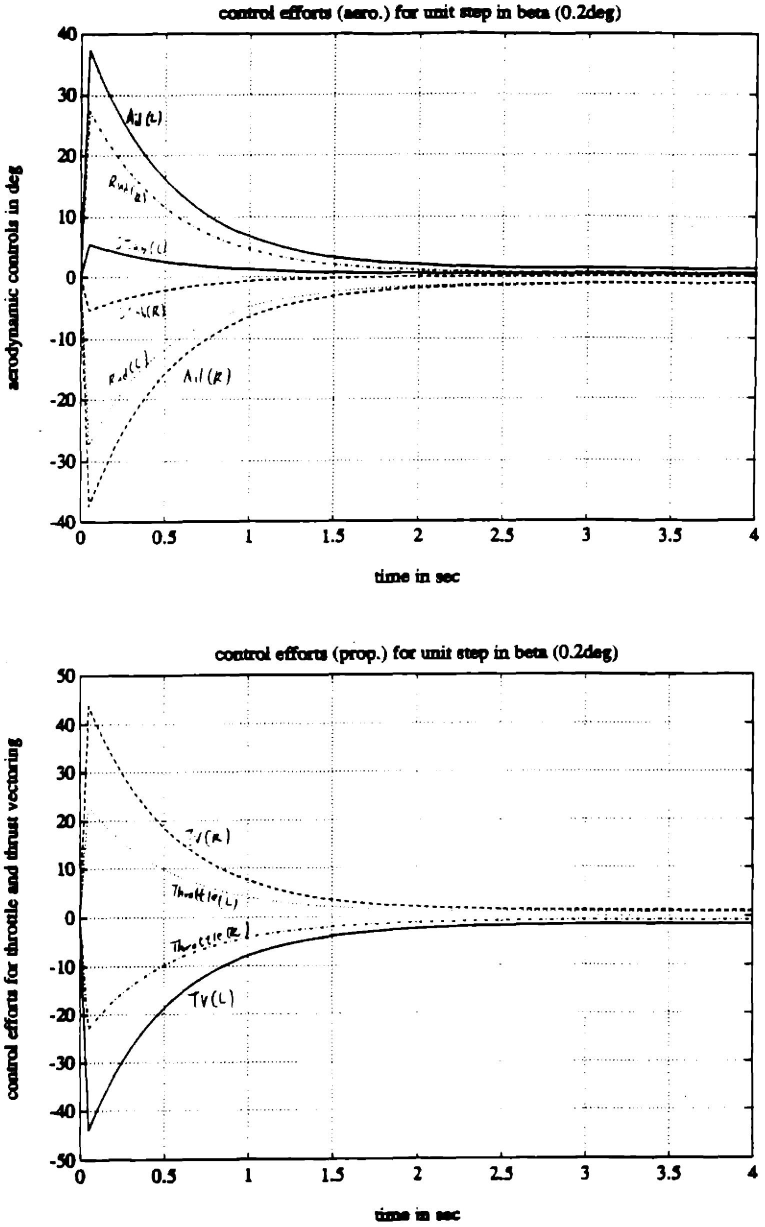

Figure 4.8 Control Actions for Unit Step Command in β (0.2 deg)

for the Linear Design

(Simulated with Nominal Linear Model)

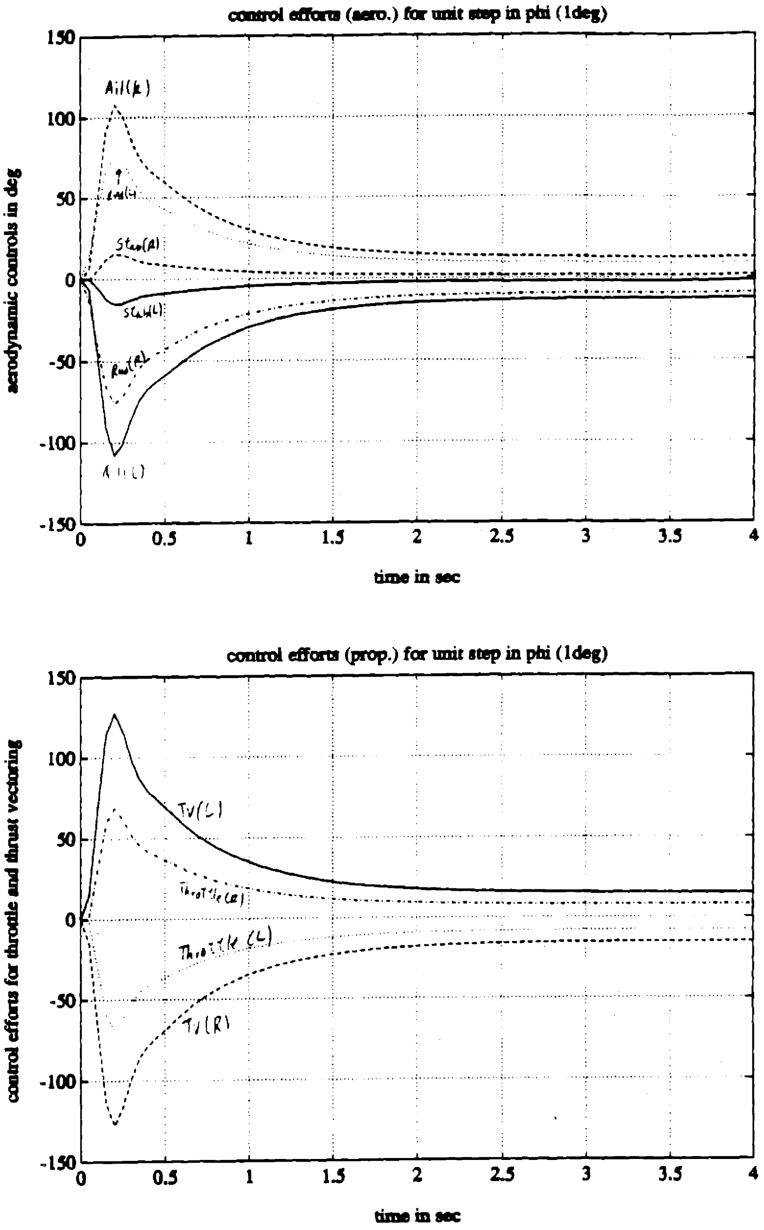

Figure 4.9 Control Actions for Unit Step Command in ϕ (1 deg)

for the Linear Design

(Simulated with Nominal Linear Model)

control efforts (aero.) for unit step in theta (1deg)

control efforts (prop.) for unit step in theta (1deg)

Figure 4.10 Control Actions for Unit Step Command in θ (1 deg)

for the Linear Design

(Simulated with Nominal Linear Model)

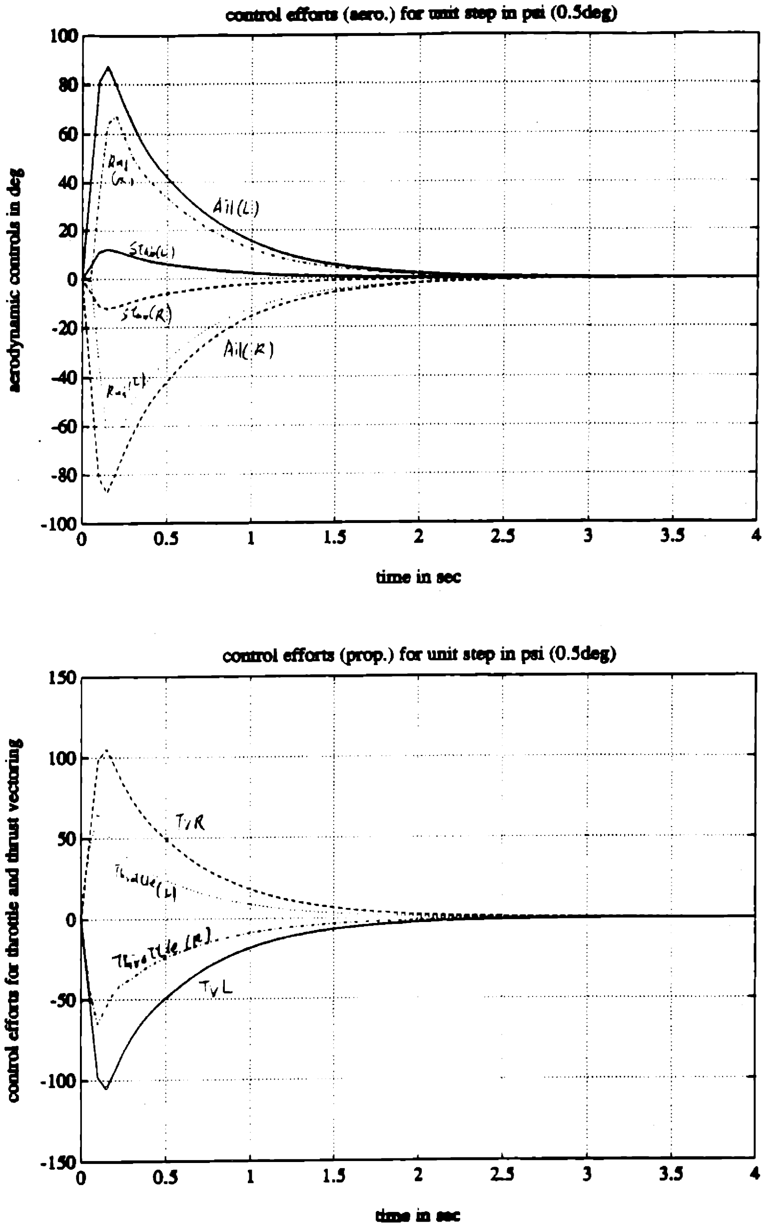

Figure 4.11 Control Actions for Unit Step Command in ψ (0.5 deg)
for the Linear Design
(Simulated with Nominal Linear Model)

One interesting observation is that when we turn off the thrust vectoring by imposing large weights on DTVL and DTVR (the control inputs corresponding to thrust vectoring), the aerodynamic controls exhibit large impulsive actions. This demonstrates the limitations of the aerodynamic controls at high α. The corresponding time simulations (using the nominal linear model) for the controls are shown in Figure 4.12 to Figure 4.17.

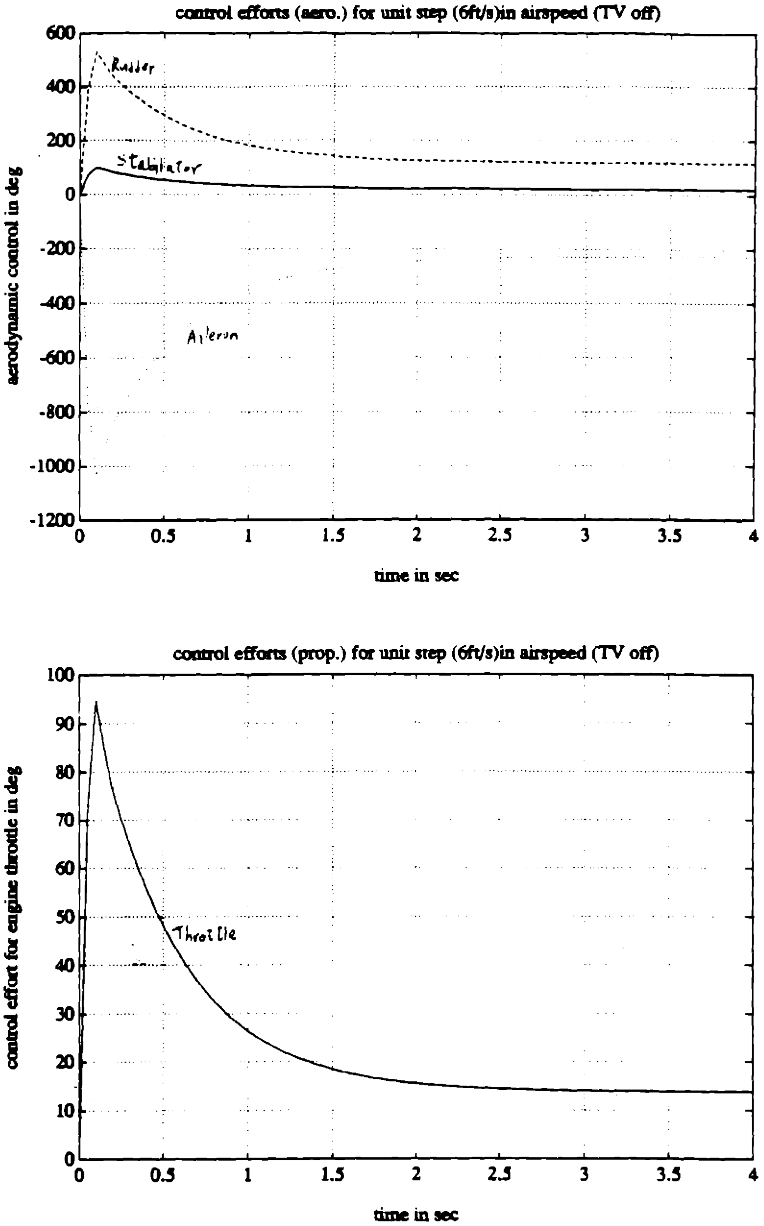

Figure 4.12 Control Actions for Unit Step Command in V_t (6 ft/sec) for the Linear Design (Simulated with Nominal Linear Model, Thrust Vectoring Off)

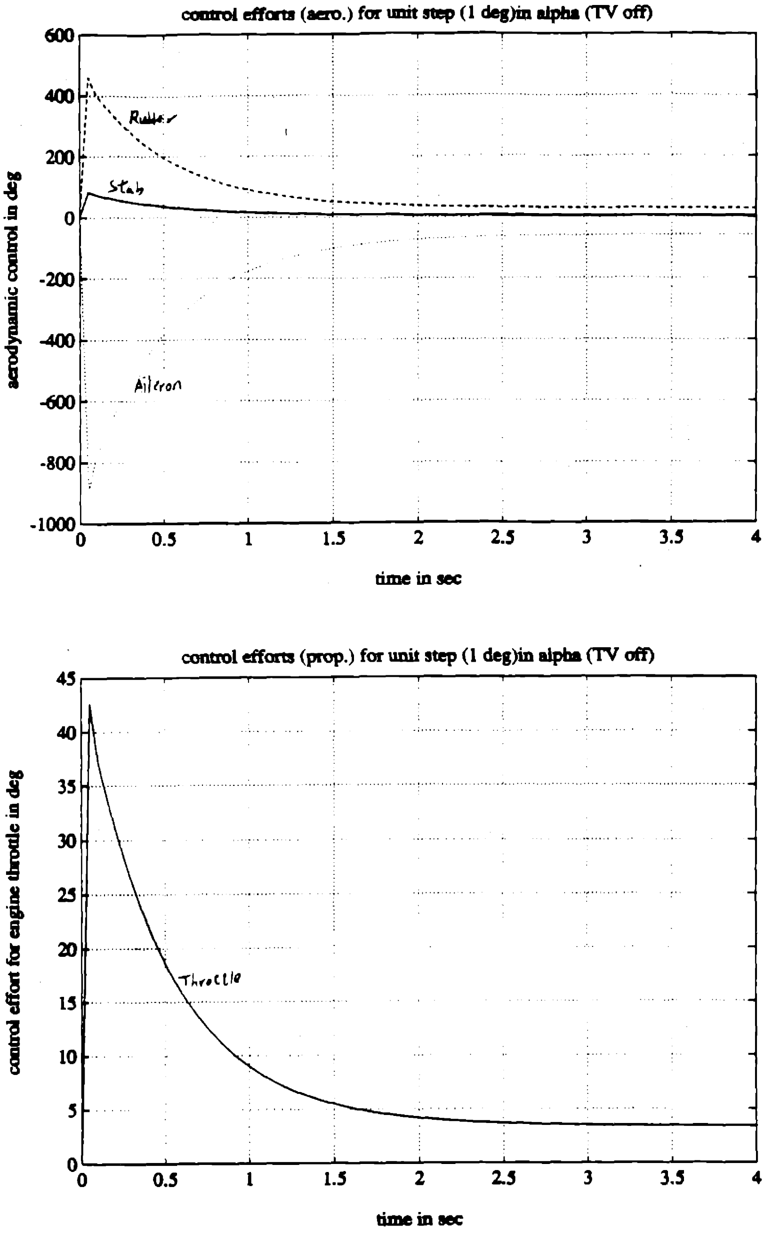

Figure 4.13 Control Actions for Unit Step Command in α (1 deg) for the Linear Design (Simulated with Nominal Linear Model, Thrust Vectoring Off)

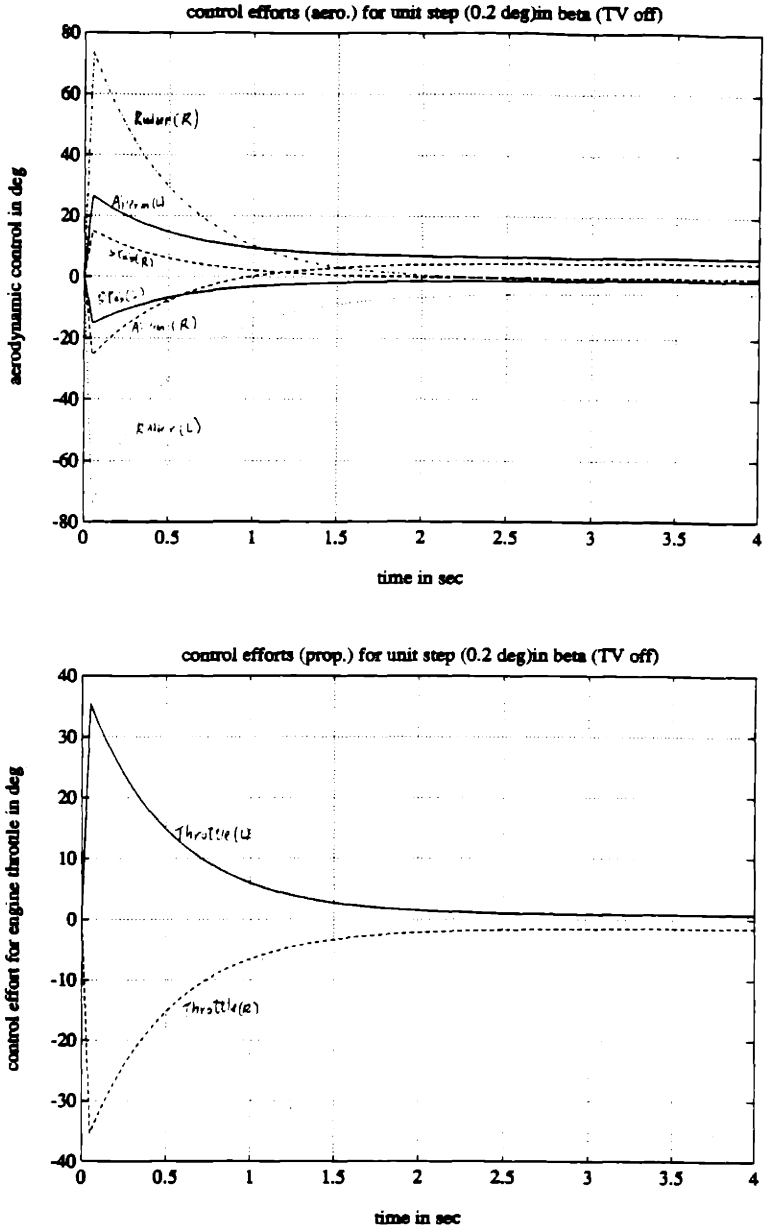

Figure 4.14 Control Actions for Unit Step Command in β (0.2 deg)

for the Linear Design

(Simulated with Nominal Linear Model, Thrust Vectoring Off)

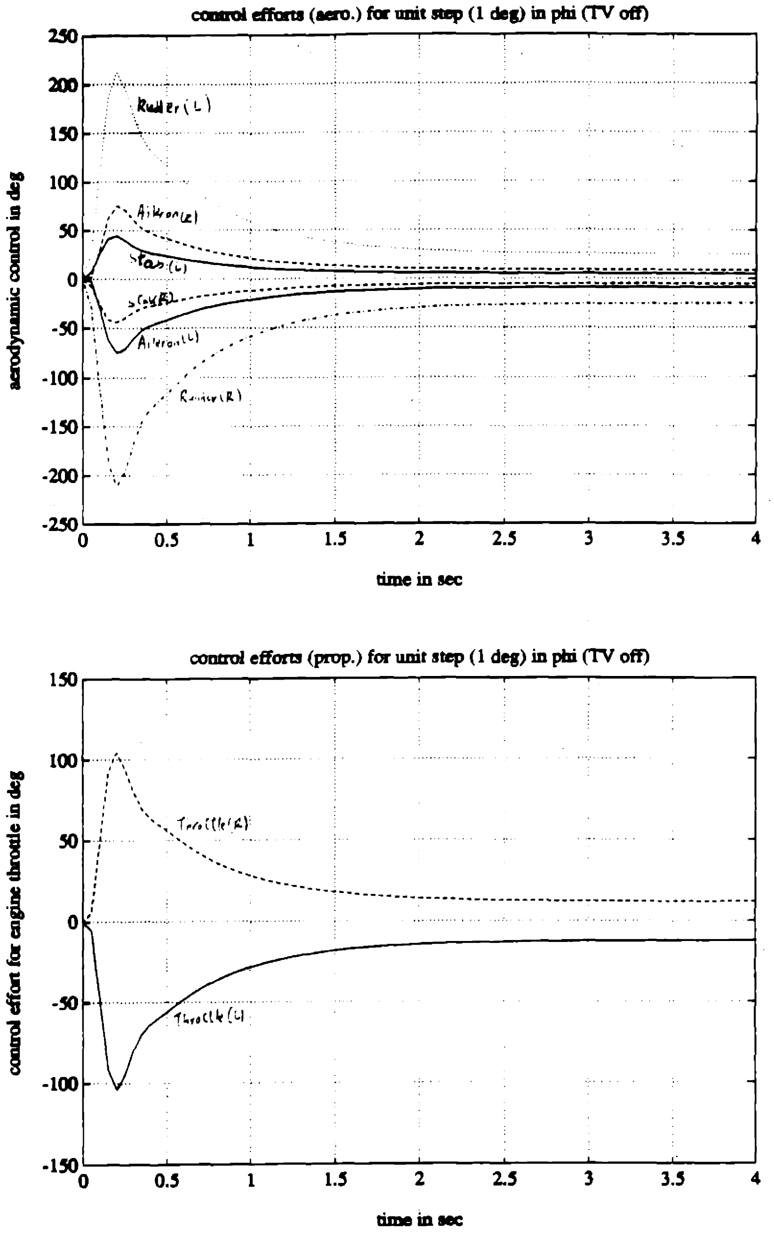

Figure 4.15 Control Actions for Unit Step Command in ϕ (1 deg) for the Linear Design (Simulated with Nominal Linear Model, Thrust Vectoring Off)

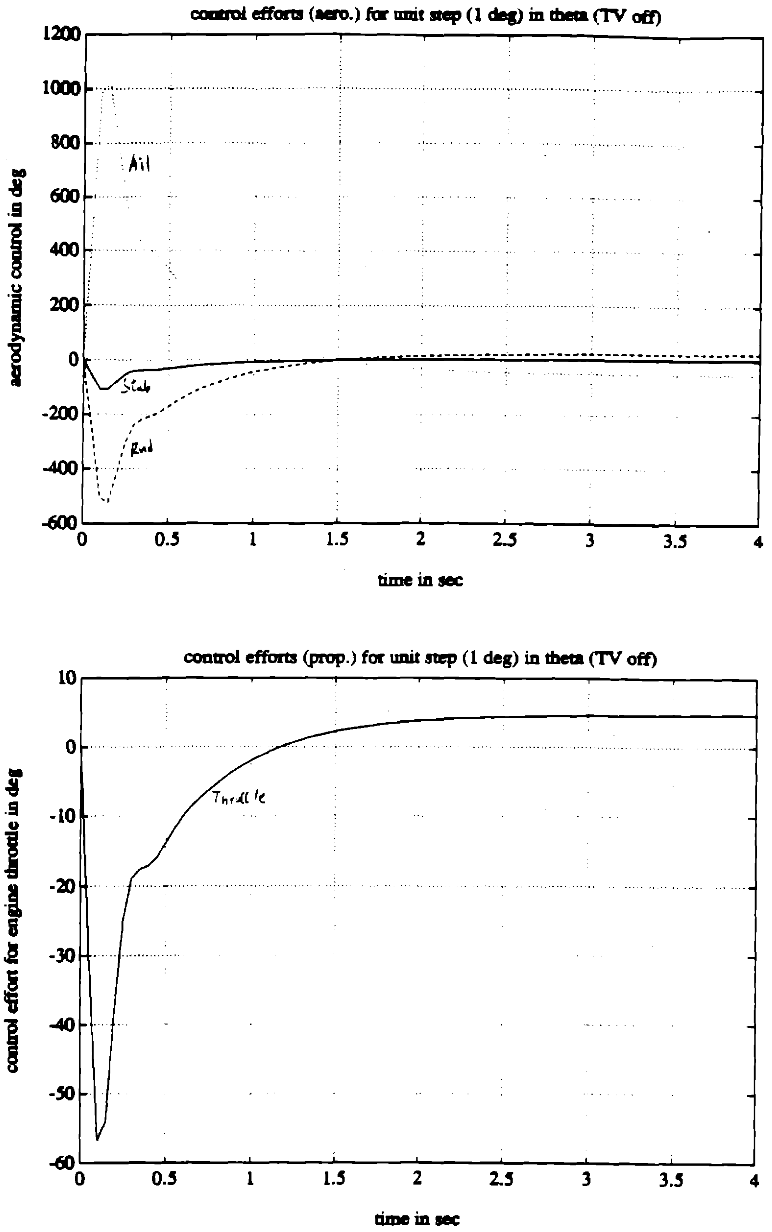

Figure 4.16 Control Actions for Unit Step Command in θ (1 deg)

for the Linear Design

(Simulated with Nominal Linear Model, Thrust Vectoring Off)

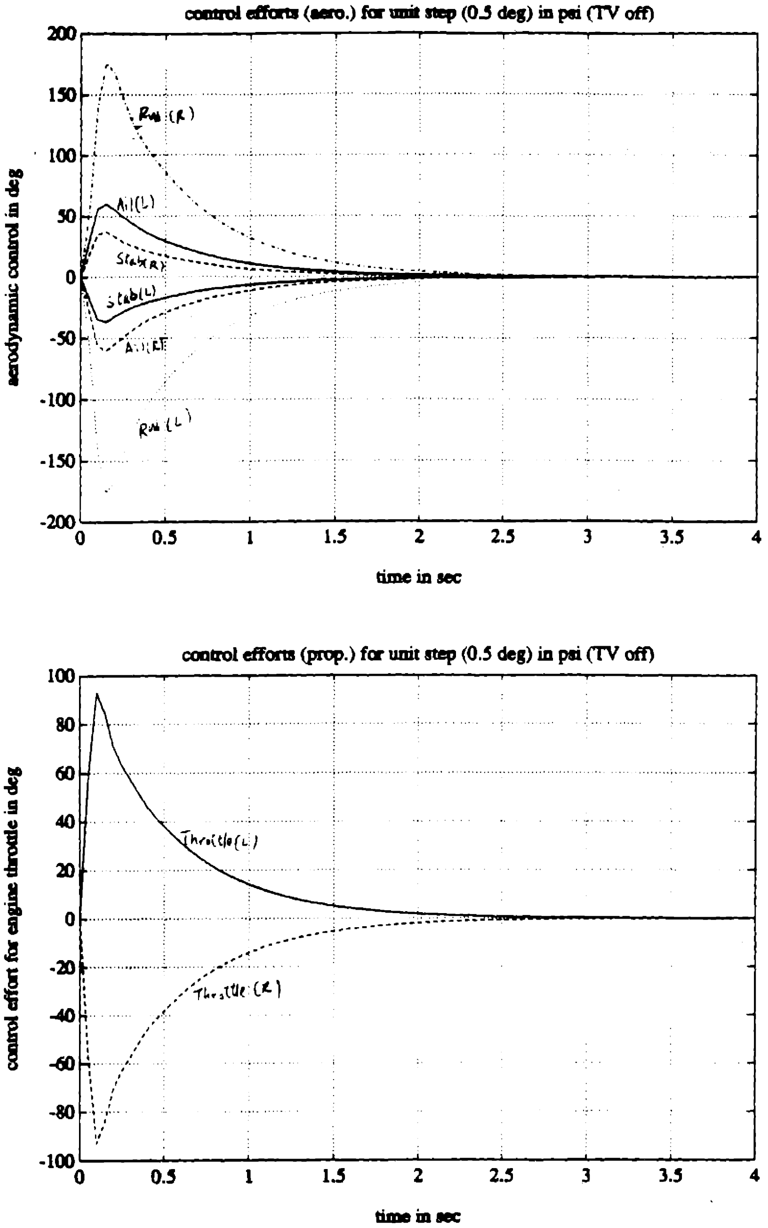

Figure 4.17 Control Actions for Unit Step Command in ψ (0.5 deg) for the Linear Design (Simulated with Nominal Linear model, Thrust Vectoring Off)

4.3 Designs Based on the Nonlinear Model (Inner-Loop/Outer-Loop Controller)

4.3.1 Structure of the Nonlinear Controller Designs

The nonlinear control designs are based on the inner-loop/outer-loop (IL/OL) controller structure introduced in Section 3.2. The inner-loop compensator utilizes the nonlinear technique of input-output linearization to transform the nonlinear physical system into a linear system, around which the outer-loop controller is designed. The inner-loop controller component has been described in some detail in Chapter 3. The outer-loop designs are discussed in the upcoming sections. Because of the simple structure of the input-output linearized system, we can actually apply single-input–single-output (SISO) design techniques for the outer-loop controller. As a result, the first design is based on state feedback and pole placement techniques, applied to the decoupled single-integrator (1/s) subsystems and the decoupled double-integrator ($1/s^2$) subsystems. A second design for the outer-loop compensator is an LQG/LTR controller augmented with integrators to the input channels.

4.3.2 Designs of the Outer-Loop Controller

4.3.2.1 Outer-Loop Pole-Placement Controller with Static State-Feedback

With the input-output linearization performed by the inner-loop compensator, the resulting linearized system is actually reduced to six decoupled simple subsystems. For the outputs, V_t, α, and β, the dynamics just consists of a single integrator.

$$\dot{V}_t = v_1 \tag{4-27}$$

$$\dot{\alpha} = v_2 \tag{4-28}$$

$$\dot{\beta} = v_3 \tag{4-29}$$

For the other outputs, θ, ϕ, and ψ, the subsystems are just double integrators.

$$\ddot{\theta} = v_4 \tag{4-30}$$

$$\ddot{\phi} = v_5 \tag{4-31}$$

$$\ddot{\psi} = v_6 \tag{4-32}$$

For the subsystems in equations 4-27 to 4-29, we can just use proportional control to achieve pole placement with the control law

$$v = ke \tag{4-33}$$

where v is the control, k is the gain of the controller and the error signal e is given by the difference between the reference command r and the output y, $e = r - y$. This control law results in a stable closed-loop pole at $s = -k$. The block diagram of the closed-loop system is shown in Figure 4.18.

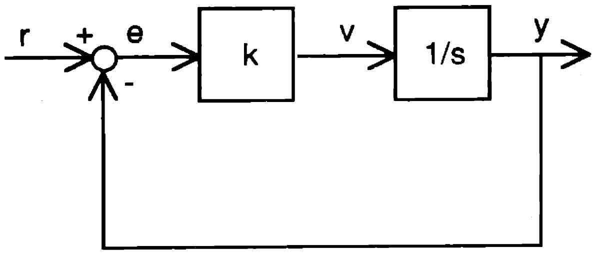

Figure 4.18 Block Diagram of the Single-Integrator System with Proportional Control

For the subsystems in equations 4-30 to 4-32, we can place the closed-loop poles as a double pole pair at $s = -k$ by choosing

$$v = -2k\dot{y} + k^2 e \tag{4-34}$$

The block diagram of the resulting closed-loop system is shown in Figure 4.19.

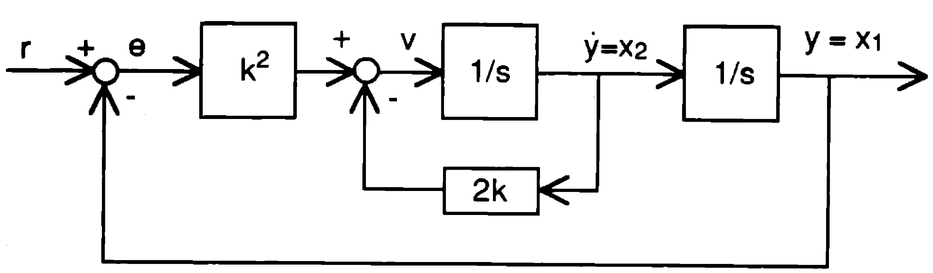

Figure 4.19 Block Diagram of the Double-Integrator System with State Feedback Control

Figures 4-20 and 4-21 are the closed-loop step response (with zero initial conditions) of the 1/s and $1/s^2$ subsystems connected with the corresponding control as in 4-33 and 4-34. Applying 4-33 and 4-34 to the input-output linearized system, we finally get

$$\dot{V}_t = v_1 = -kV_t + kr_1 \tag{4-35}$$

$$\dot{\alpha} = v_2 = -k\alpha + kr_2 \tag{4-36}$$

$$\dot{\beta} = v_3 = -k\beta + kr_3 \tag{4-37}$$

$$\ddot{\theta} = v_4 = -2k\dot{\theta} + k^2(r_4 - \theta) \tag{4-38}$$

$$\ddot{\phi} = v_5 = -2k\dot{\phi} + k^2(r_5 - \phi) \tag{4-39}$$

$$\ddot{\psi} = v_6 = -2k\dot{\psi} + k^2(r_6 - \psi) \tag{4-40}$$

with all the closed-loop poles placed at s = -k.

In equations 4-35 to 4-40, we have chosen all the k's in the different channels to be the same. However, this does not have to be so. We may desire a different closed-loop bandwidth for each individual output. The choice of the desired bandwidth depends on the flight operation requirements and the limits imposed by the controls, such as saturation limits and rate limits. Since the six output channels are decoupled in equations 4-35 to 4-40, the different requirements can be easily accommodated by choosing the k for each individual channel appropriately, taking into account the distinct characteristics of the corresponding channel.

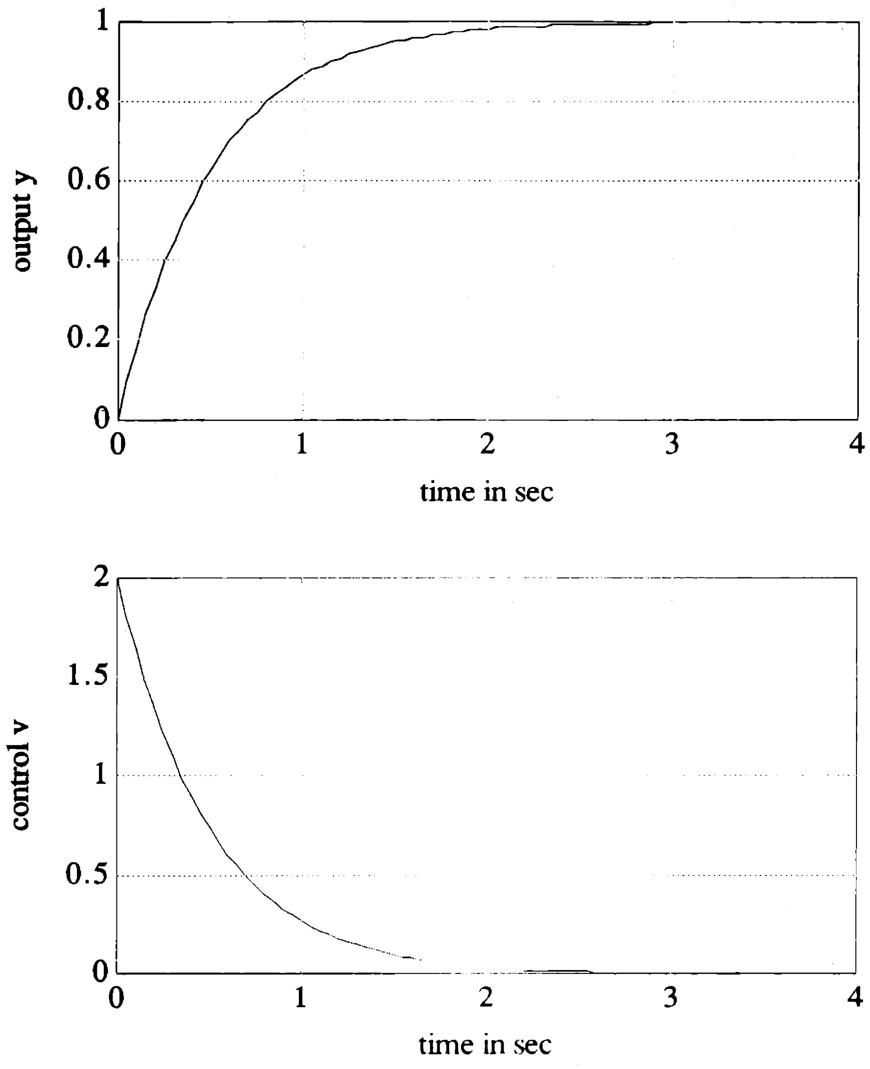

Figure 4.20 Closed-Loop Step Response of the Single-Integrator System with Proportional Control

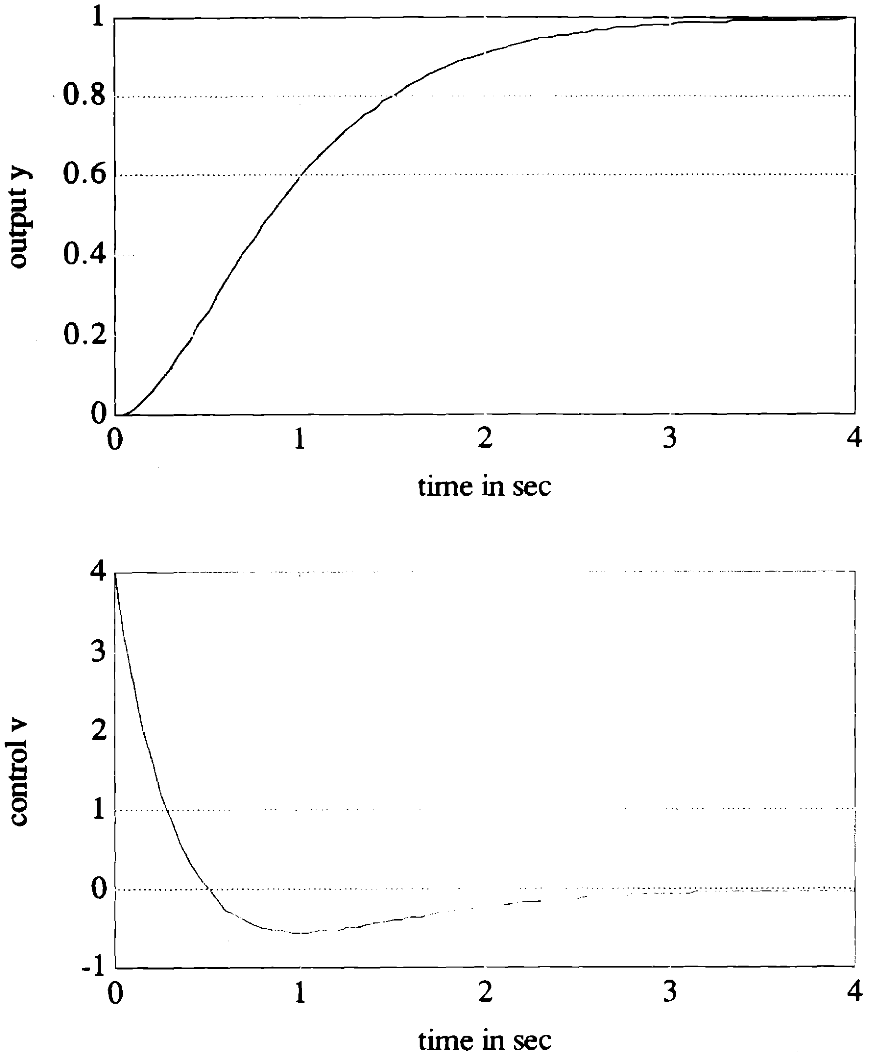

Figure 4.21 Closed-Loop Step Response of the Double-Integrator System with State Feedback Control

4.3.2.2 Outer-Loop LQG/LTR Controller

The input-output linearized system is given by

$$\dot{z} = A_l z + B_l v \tag{4-41}$$

$$y = C_l z \tag{4-42}$$

with

$$A_l = \begin{bmatrix} 0&0&0&0&0&0&0&0&0 \\ 0&0&0&0&0&0&0&0&0 \\ 0&0&0&0&0&0&0&0&0 \\ 0&0&0&0&1&0&0&0&0 \\ 0&0&0&0&0&0&0&0&0 \\ 0&0&0&0&0&0&1&0&0 \\ 0&0&0&0&0&0&0&0&0 \\ 0&0&0&0&0&0&0&0&1 \\ 0&0&0&0&0&0&0&0&0 \end{bmatrix}, \; B_l = \begin{bmatrix} 1&0&0&0&0&0 \\ 0&1&0&0&0&0 \\ 0&0&1&0&0&0 \\ 0&0&0&0&0&0 \\ 0&0&0&1&0&0 \\ 0&0&0&0&0&0 \\ 0&0&0&0&1&0 \\ 0&0&0&0&0&0 \\ 0&0&0&0&0&1 \end{bmatrix}$$

$$C_l = \begin{bmatrix} 1&0&0&0&0&0&0&0&0 \\ 0&1&0&0&0&0&0&0&0 \\ 0&0&1&0&0&0&0&0&0 \\ 0&0&0&1&0&0&0&0&0 \\ 0&0&0&0&0&1&0&0&0 \\ 0&0&0&0&0&0&0&1&0 \end{bmatrix}$$

and

$$z = [V_t, \alpha, \beta, \theta, \dot{\theta}, \phi, \dot{\phi}, \psi, \dot{\psi}]^T$$

$$y = [V_t, \alpha, \beta, \theta, \phi, \psi]^T$$

$$v = [v_1, v_2, v_3, v_4, v_5, v_6]^T$$

Once again, we augment the input channels with integrators, and design the controller around the augmented system $[A_a, B_a, C_a]$, just as in the case of the linear design in Section 4.2.

In the target loop design, with the particular structure of A_a for the augmented system, we pick

$$L_l = s\begin{bmatrix} I_{3x3} & 0_{3x3} \\ 0_{3x3} & sI_{3x3} \end{bmatrix}, \quad \text{with } s = j\omega \rightarrow 0 \qquad (4\text{-}43)$$

to match the singular values at low frequencies,

and $\quad L_h = C_l^T(C_lC_l^T)^{-1}$ (4-44)

to match the singular values at high frequencies.

Using $\mu = 1/4$ (for a crossover frequency of 2 rad/sec), $s = j(10^{-3})$ for the calculation of L_l, and $\rho = 10^{-8}$, the resulting singular value plots for the target loop and the recovered loop are shown in Figure 4.22 and Figure 4.23 respectively.

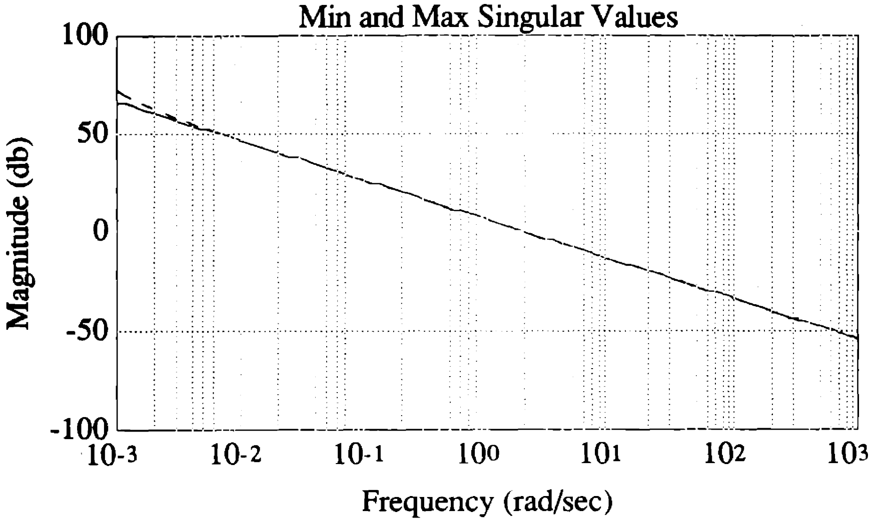

Figure 4.22 Singular Value Plot of the Target Loop of the Outer-Loop LQG/LTR design

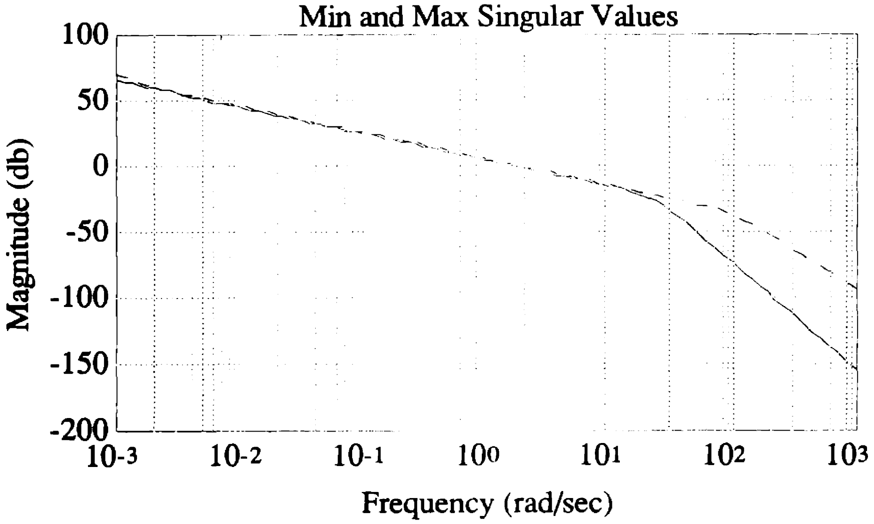

Figure 4.23 Singular Value Plot of the Recovered Loop of the Outer-Loop LQG/LTR design

The state space description of the LQG/LTR controller takes the form as in equations 4-25 and 4-26. The numerical values of the G and H matrices of the LQG/LTR controller can be found in Appendix F. Step responses of the closed-loop system (with zero initial conditions) for the α and θ channels, simulated with the nominal design model, are included in Figure 4-24 and Figure 4-25.

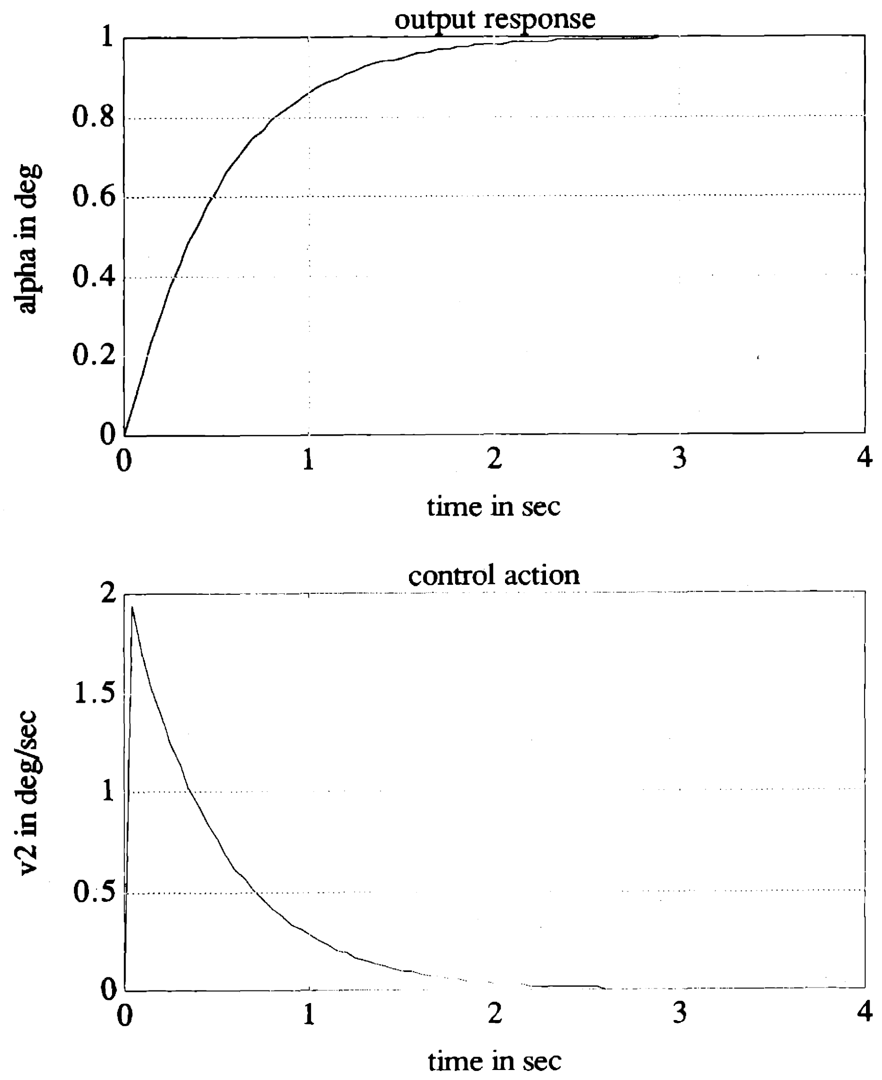

Figure 4.24 Closed-Loop Step Response in the α-Channel of the Outer-Loop LQG/LTR Design (Simulated with Nominal Design Model)

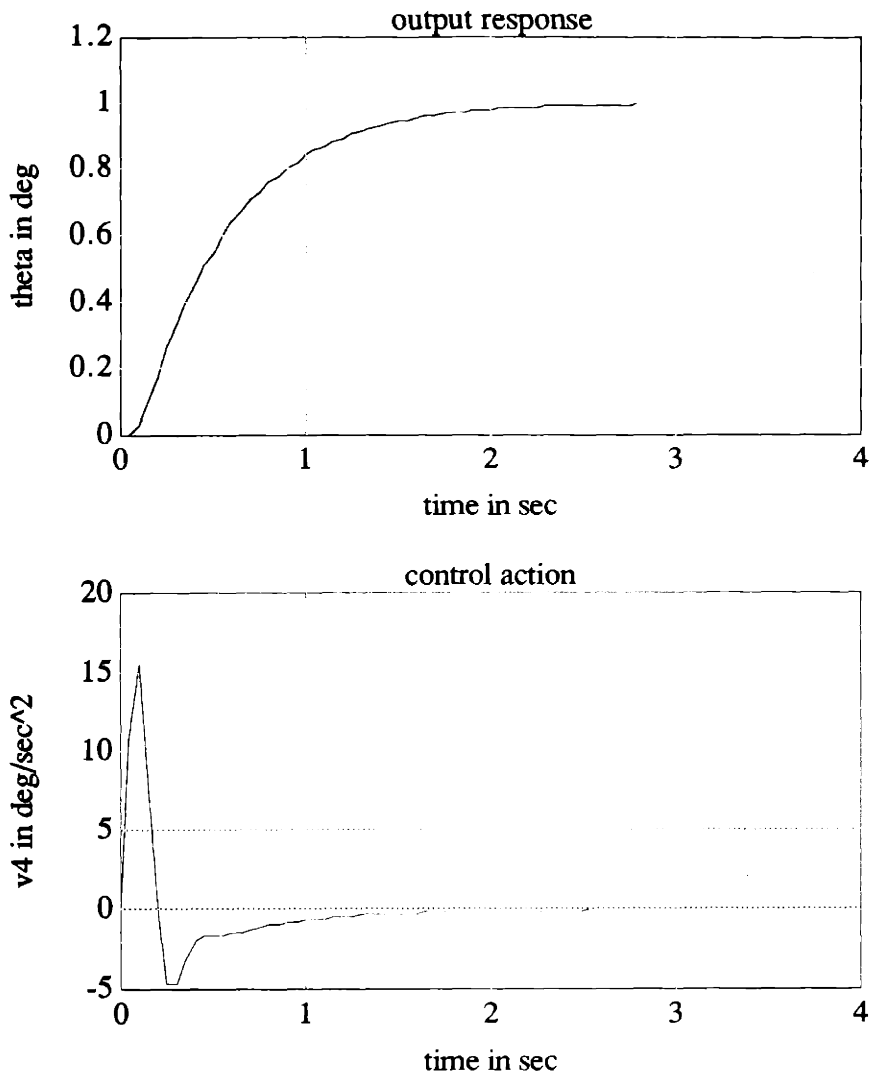

Figure 4.25 Closed-Loop Step Response in the θ-Channel of the Outer-Loop LQG/LTR Design (Simulated with Nominal Design Model)

4.5 Summary

This chapter provides a description of the overall controller designs. The developments of the linear and nonlinear designs are covered in some detail. Time history results simulated with the nominal design models are included to establish an upper bound for the performance level of the controllers when used with the "real" nonlinear system.

CHAPTER 5

EVALUATION AND COMPARISON OF THE CONTROLLER DESIGNS

5.1 Introduction

In this chapter, we are going to compare and evaluate the controller designs we developed in the previous chapter. In the comparison of the controller designs, the LQG/LTR design based on the trim point linear model is referred to as Design 1. The nonlinear design with the outer-loop pole-placement controller using state feedback is referred to as Design 2. Lastly, the nonlinear design with the outer-loop LQG/LTR controller is referred to as Design 3.

5.2 Stability of the Closed-Loop Systems

The least we should ask for in any design is stability of the closed-loop system. All the designs described above provide closed-loop stability for the nominal design model. However, because of modelling errors, this may not be the case if we hook up the controllers with the real system. As a preliminary verification for the controller designs, the controllers are hooked up with the nonlinear simulation code of the vehicle dynamics, and time simulations are performed commanding the controller to regulate the airplane around the trim point ($h = 15000$ ft, $\alpha = \theta = 35^\circ$), where the designs are based on.

For the LQG/LTR design based on the trim point linear model, nothing interesting happens if we start the simulation with the states and controls at the trim settings. With zero error signals, we have zero output (δu) from the LQG/LTR controller and the controls remain at the trim settings, so the plane just stays at the trim point. On the other hand, there is a different story for the nonlinear designs in the absence of the outer-loop controller. Because of parametric uncertainties and modelling errors, the linearizing controls computed by the inner-loop compensator are actually different from the trim control settings. As a result, even if the initial states of the aircraft are at the trim settings, the aircraft will not stay at the trim point because the time derivative of the state vector is actually nonzero at t=0.[1] In addition, we learn from the linear model of the inner-loop compensated system in Section 3.4 that the inner-loop compensated system is actually unstable. Consequently, regulating control from the outer-loop compensator is needed to remain in the neighborhood around the trim point. Time simulation results of the regulators based on Design 2 and Design 3 are shown in figures 5.1 and 5.2.

---

[1] The **d** vector in equation 3-18a is nonzero.

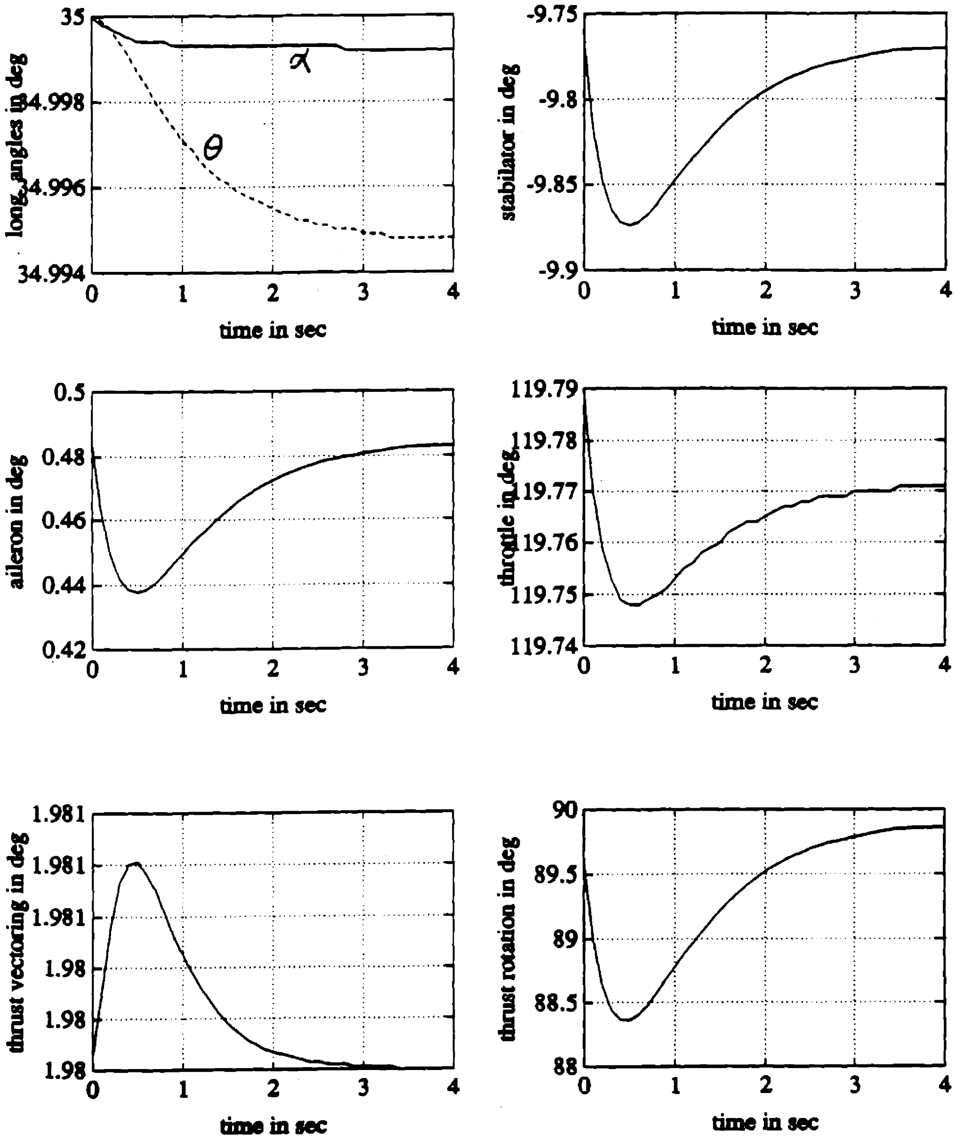

Figure 5.1 Regulation Response of Design 2

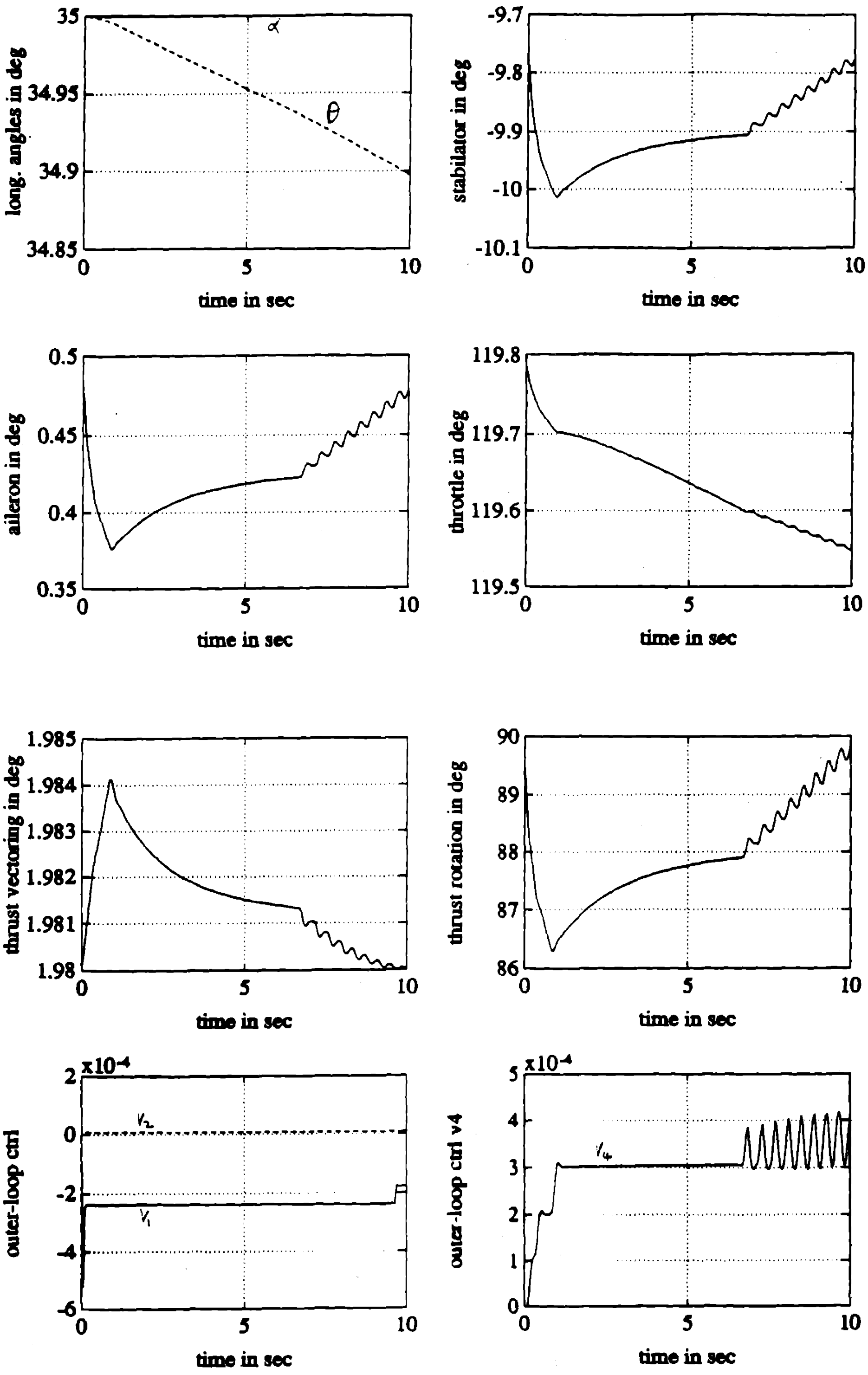

Figure 5.2 Regulation Response of Design 3

As we see in Figure 5.1 and Figure 5.2, Design 2 holds on to the trim point gracefully (though with a very little offset) while Design 3 fails to maintain a steady pitch angle at all. Upon closer inspection of Design 3, we find that the reason for the poor performance may be due to the inexact cancellations of poles and zeros very close to the origin. Using the nominal design model (we are not considering the nonlinearity in the real system yet), we find that the closed-loop system has four poles very close to the origin, namely at $s = -0.001 \pm j(1.2904 \times 10^{-6})$, $-0.001 \pm j(3.9372 \times 10^{-6})$, -0.001, and -9.9898×10^{-6}. The six closed-loop zeros that are supposed to cancel these poles are located at $s = -9.9911 \times 10^{-4} \pm j(2.4315 \times 10^{-5})$, $-9.9911 \times 10^{-4} \pm j(2.4315 \times 10^{-5})$, and $-9.9911 \times 10^{-4} \pm j(2.4315 \times 10^{-5})$. The inexact pole-zero cancellations leave us with a residual long tail in the closed-loop responses if the modes corresponding to these slow-moving closed-loop poles are excited. We can see this effect by looking at the regulation response with a perturbed $\dot{\theta}$, simulated with the nominal design model.

With $\dot{\theta} = -1$, and the rest of the states equal to zero at time $t = 0$, we get the following time response by commanding the states back to zero,

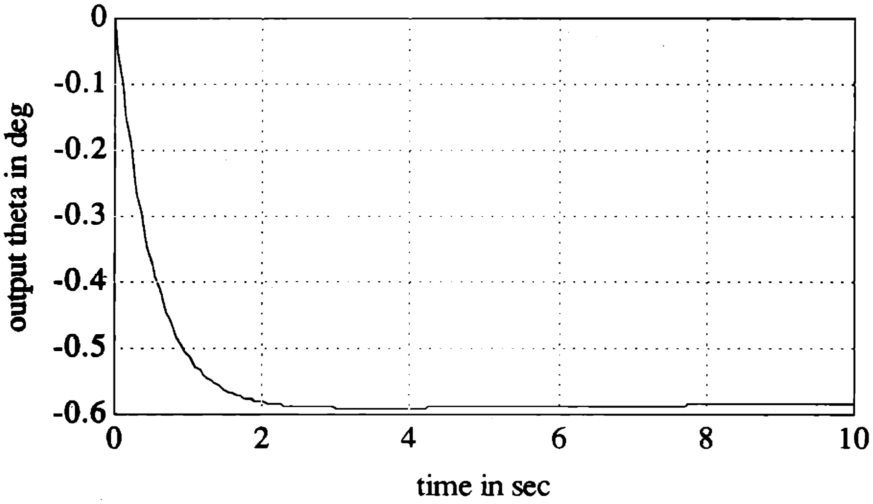

Figure 5.3 Regulator Response of Design 3 with Perturbed $\dot{\theta}$ at $t = 0$ (Simulated with Linear Nominal Design Model)

The same effect is also observed in the step response of θ, if $\dot{\theta}$ is perturbed from zero at $t = 0$. With $\dot{\theta} = -1°/\text{sec}$ and the rest of the states equal to zero at $t = 0$ sec, we get the following time response of θ by issuing a step command in θ of 1°. There is a long and slowly-rising tail trying to climb up to the commanded level in θ.

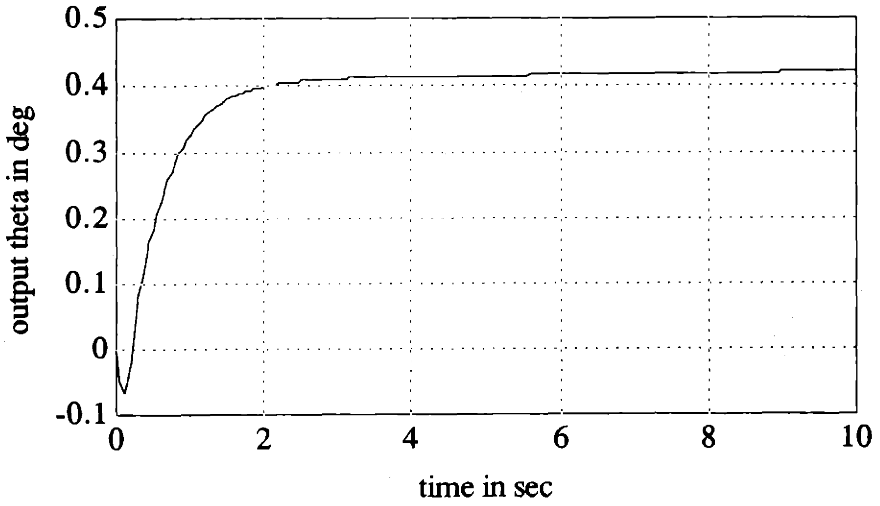

Figure 5.4 Step Response of Design 3

with Perturbed $\dot{\theta}$ at $t = 0$

(Simulated with Linear Nominal Design Model)

As a result, Design 3 does not seem to fare well even in the absence of modelling errors. With the parametric uncertainties and modelling errors in performing the input-output linearization, the resulting input-output linearized system is far from the nominal design model. Design 3, handicapped with the inexact pole-zero cancellations, fails to handle the perturbation in the pitching moment (through nonzero $\ddot{\theta}$ in the offset vector **d** in equation 3-18a). It is not even able to maintain a constant pitch angle. The augmenting integrators in Design 3 are intended for extra robustness against modelling errors and perturbations, since we do not really need them for the type-1 (single-integrator) and type-2 (double-integrator) systems we are dealing with. The outer-loop LQG/LTR design with augmented integrators seems to be a misguided effort and rather an overkill. The target loop design is not handled very well with the way we match the singular values at low frequencies, which in turn causes the inexact pole-zero cancellations. It seems that Design 2 using state feedback for the outer-loop control is more robust to modelling uncertainties, resulting from the imperfect input-output linearization, than a dynamic controller (e.g. Design 3) which only has access to the output variables. The dynamic controller structure is less robust to the modelling uncertainties probably because of the way it achieves approximate plant inversion through pole-zero cancellations. In the presence of parameter uncertainties and modelling errors, the pole-zero cancellations will be inexact and the resulting closed-loop system may exhibit drastic difference from the nominal design. Consequently, from this point on, we limit the comparison mainly between Design 1 and Design 2.

5.3 Comparison of the Linear and Nonlinear Designs through Time Simulations of Tracking Response

The ultimate way to evaluate and compare the designs is to put them into the flight control system and take the plane out for flight tests. Obviously, this may be costly or even dangerous. The next best thing is to hook up the controller designs with a reasonably accurate model of the nonlinear dynamics and perform time simulations for the desired maneuvers. This is exactly how we evaluate and compare the controller designs in this section. The time simulation is based on the nonlinear model of the vehicle dynamics provided by NASA/Langley and a fourth-order Runge-Kutta integration scheme. The nonlinear model used for the simulation includes nonlinear effects in the aerodynamics of the vehicle, inertial couplings, nonlinearity in thrust vectoring and dynamics of the twin turbofan engines. Dynamics of the control surface actuators and sensor noise are assumed to be negligible.

The first maneuver (maneuver 1) under consideration is a 0.2 deg step command in θ from the trim level flight at h = 15000 ft , $\alpha = 35^\circ$. To avoid saturation in the controls from the discontinuous step command, the reference step command is passed through a prefilter with transfer function $G_{pf}(s) = 2/s+2$ before reaching the controllers. The results of the time simulation are shown in Figure 5.5 to Figure 5.7. The discontinuities of σ (thrust vectoring angle) and η (thrust rotation angle) appearing in the time simulations are due to the sign convention we pick to limit the values of the angles to within ±90°. Positive σ corresponds to upward deflection of the thrust to provide a force in the -z direction (the z axis is pointing down). Positive η corresponds to clockwise rotation of the thrust vector about the x-axis after first being deflected up and down with an angle described by σ. Readers can refer back to Figure 2.6 for the definitions of σ and η. The thrust rotation angle is not shown for Design 1 in the time simulation because η is kept zero for all time for Design 1. In addition, the time histories for the airspeed are omitted because the airspeed remains pretty constant around the trim value.

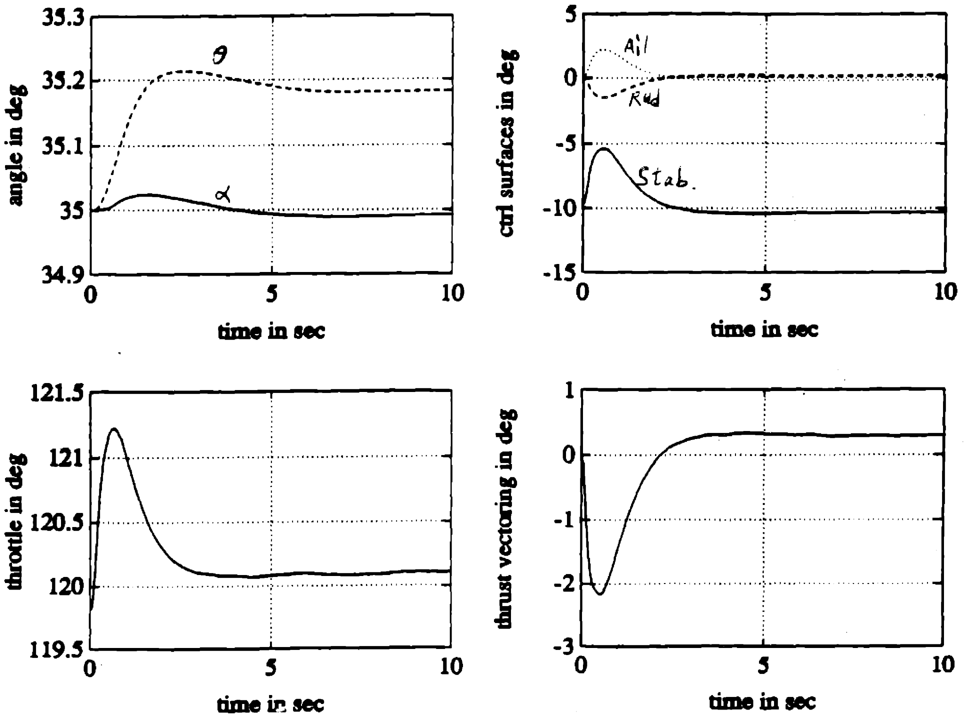

Figure 5.5 Tracking Response of 0.2 deg Step in θ for Design 1

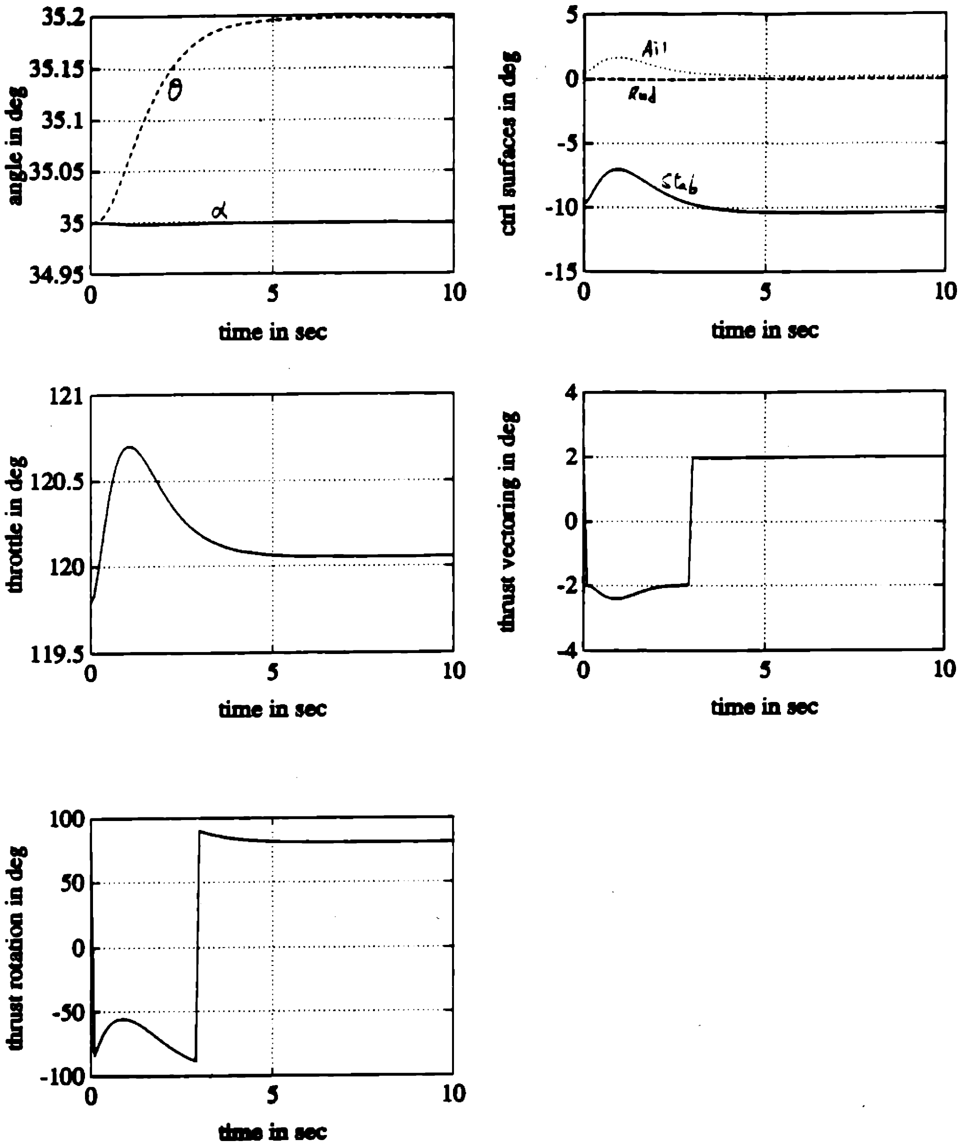

Figure 5.6 Tracking Response of 0.2 deg Step in θ for Design 2

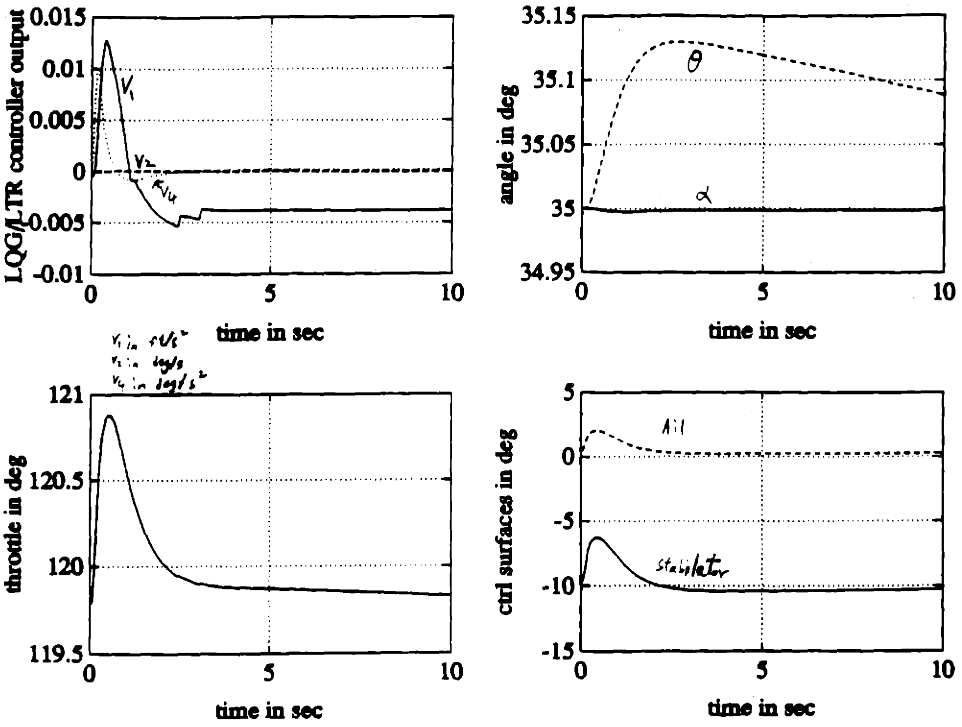

Figure 5.7 Tracking Response of 0.2 deg Step in θ for Design 3

From Figure 5.5 and Figure 5.6, we see that both Design 1 and Design 2 do a decent job in tracking the reference command. However, looking at the time histories of the outputs and the controls, one cannot argue with the statement that the nonlinear design (Design 2) does perform better. Design 2 tracks the command more accurately with gentler control actions. It also maintains a smaller tracking offset at the end of the time simulation.

We have learned in the previous section that Design 3 has trouble in controlling the pitch angle. It is not surprising to see the poor tracking response presented in Figure 5.7 for a step command in θ. Actually, the time history plot of θ is reminiscent to Figure 5.4, the step response simulated with the nominal design model starting with a perturbed $\dot{\theta}$ at t = 0. We speculate that the perturbation in $\ddot{\theta}$ caused by the imperfect input-output linearization seems to build up a nonzero $\dot{\theta}$ at the beginning of the simulation. The accumulating effects of the modelling error and disturbance in the pitching motion prove critical and the controller never has a chance to recover control of θ. The controller just fails as time goes on.

Next, we are going to switch our comparison to a lateral maneuver (maneuver 2). This time we will try a 0.1° step in heading ψ. Once again, the reference command is generated by passing the step through a prefilter, $G_{pf}(s) = 2/s+2$, to avoid control saturation. The simulation results are shown in Figure 5.8 to Figure 5.10.

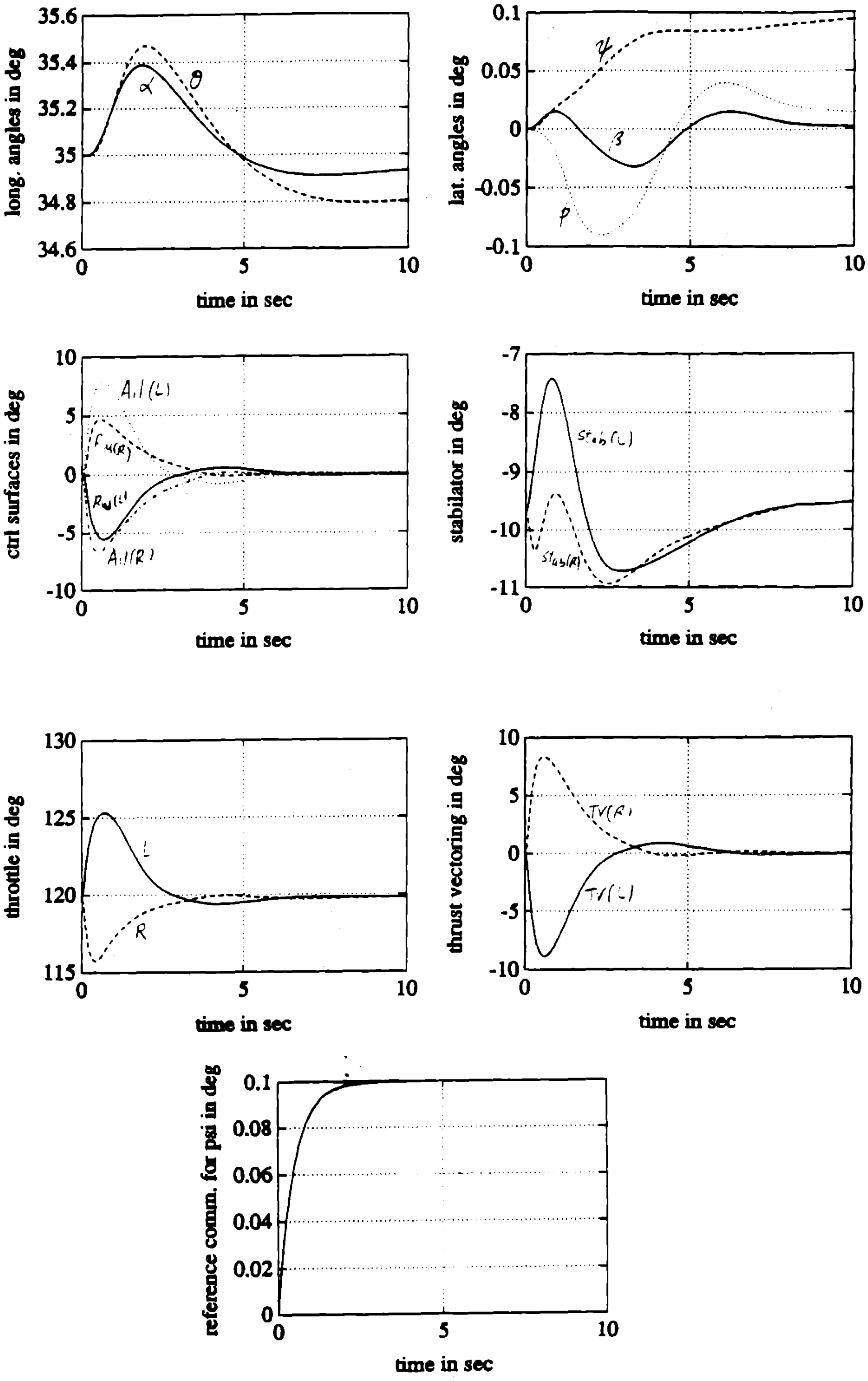

Figure 5.8 Tracking Response of 0.1 deg Step in ψ for Design 1

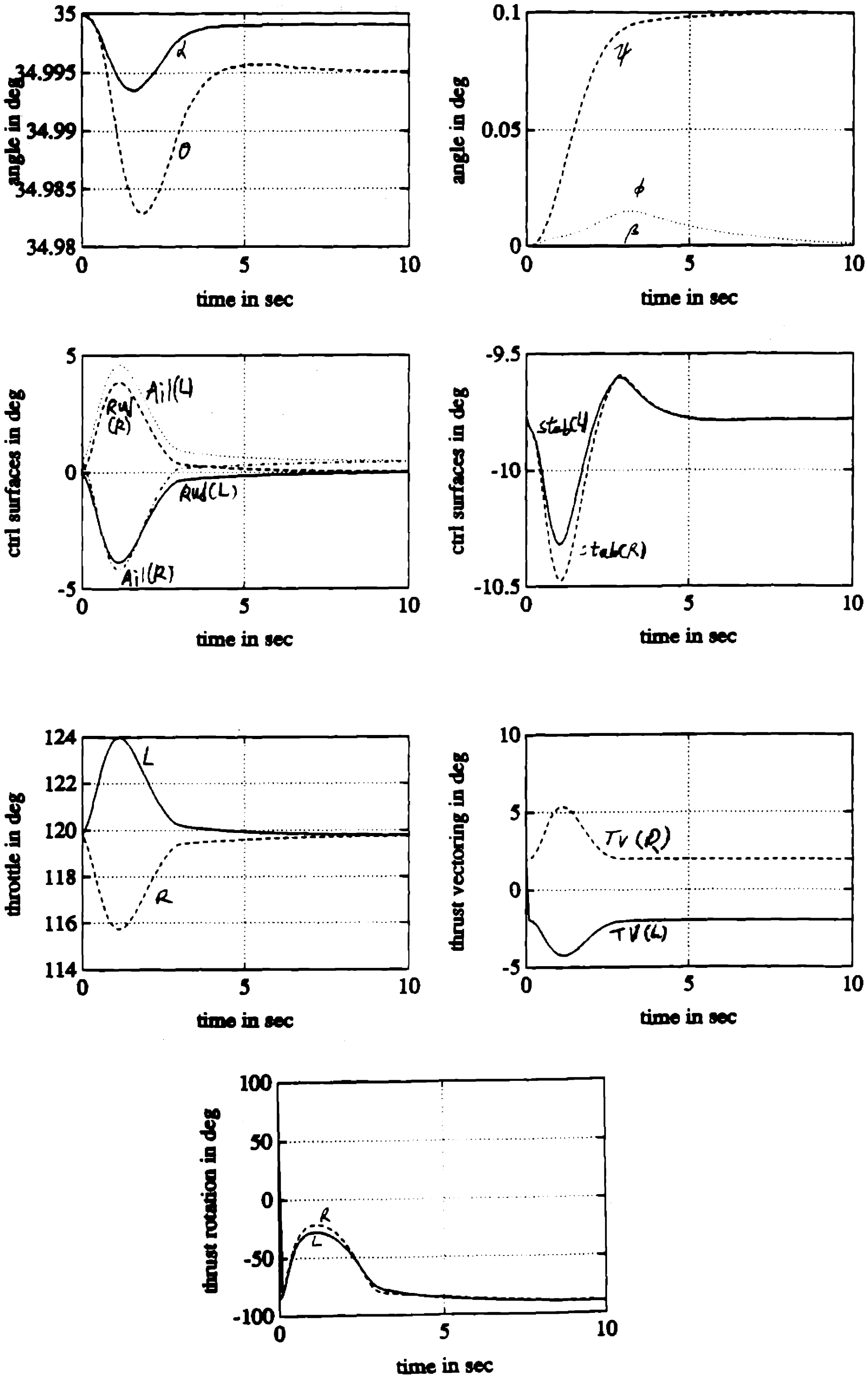

Figure 5.9 Tracking Response of 0.1 deg Step in ψ for Design 2

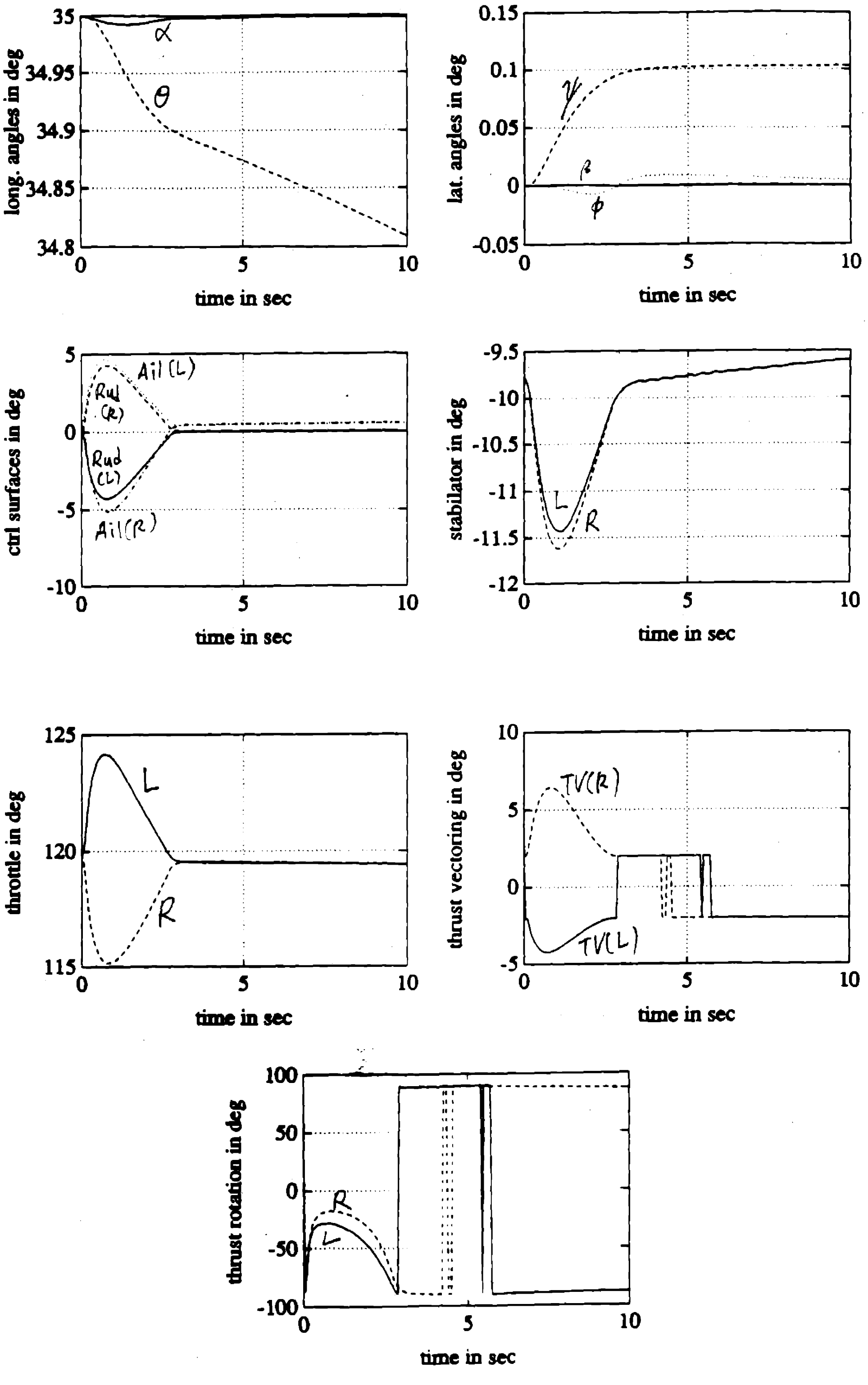

Figure 5.10 Tracking Response of 0.1 deg Step in ψ for Design 3

Looking at figures 5.8 and 5.9, the difference in performance between Design 1 and Design 2 is more prominent than in the previous pitch maneuver. For Design 1, the tracking response of the lateral variables are barely acceptable. The longitudinal variables demonstrate relatively large fluctuations from the desired levels and offsets in α and θ from the commanded levels are easily noticeable at the end of the simulation. On the other hand, Design 2 looks marvelous compared to Design 1 in terms of both the output and control time histories. Tracking is more accurate and the control action is small. This difference in performance may be explained by the fact that the linear model for the vehicle dynamics used in Design 1 is obtained at a trim point with no angular motions (level flight). By linearizing around the trim with $\beta = \phi = P = Q = R = 0$, a lot of the coupling terms in the equations of motion disappear, and the effects of the inertial coupling are thus not included in the linear model. Besides, in Design 1, we are limiting the thrust vectoring to remain in a up-and-down fashion, which may hamper its capability for lateral control somewhat. However, the omission of the inertial couplings seems to be by far the more important factor. Design 3 seems to perform adequately for the lateral outputs, but it loses control on θ as expected from our previous experience. This demonstrates again the importance of the nonlinear inertial couplings in the control of lateral motion. Both designs, including the effects of the couplings, fare better than Design 1 which ignores the coupling in the linear design model.

The final pair of maneuvers are intended to study the effects of the α–nonlinearities on the controllers. Starting from the level trim flight at h = 15000 ft, and α=35°, we first command the aircraft to another level trim at h = 15000 ft, and α=34.5° (maneuver 3a). This corresponds to commanding V_t form 211.231 ft/sec to 212.661 ft/sec, α from 35° to 34.5°, and θ from 35° to 34.5°. Once again the reference commands are generated by passing the step commands through the prefilter, $G_{pf}(s) = 2/s+2$, to avoid control saturations. Results of the time simulation are shown in Figure 5.11 to Figure 5.13.

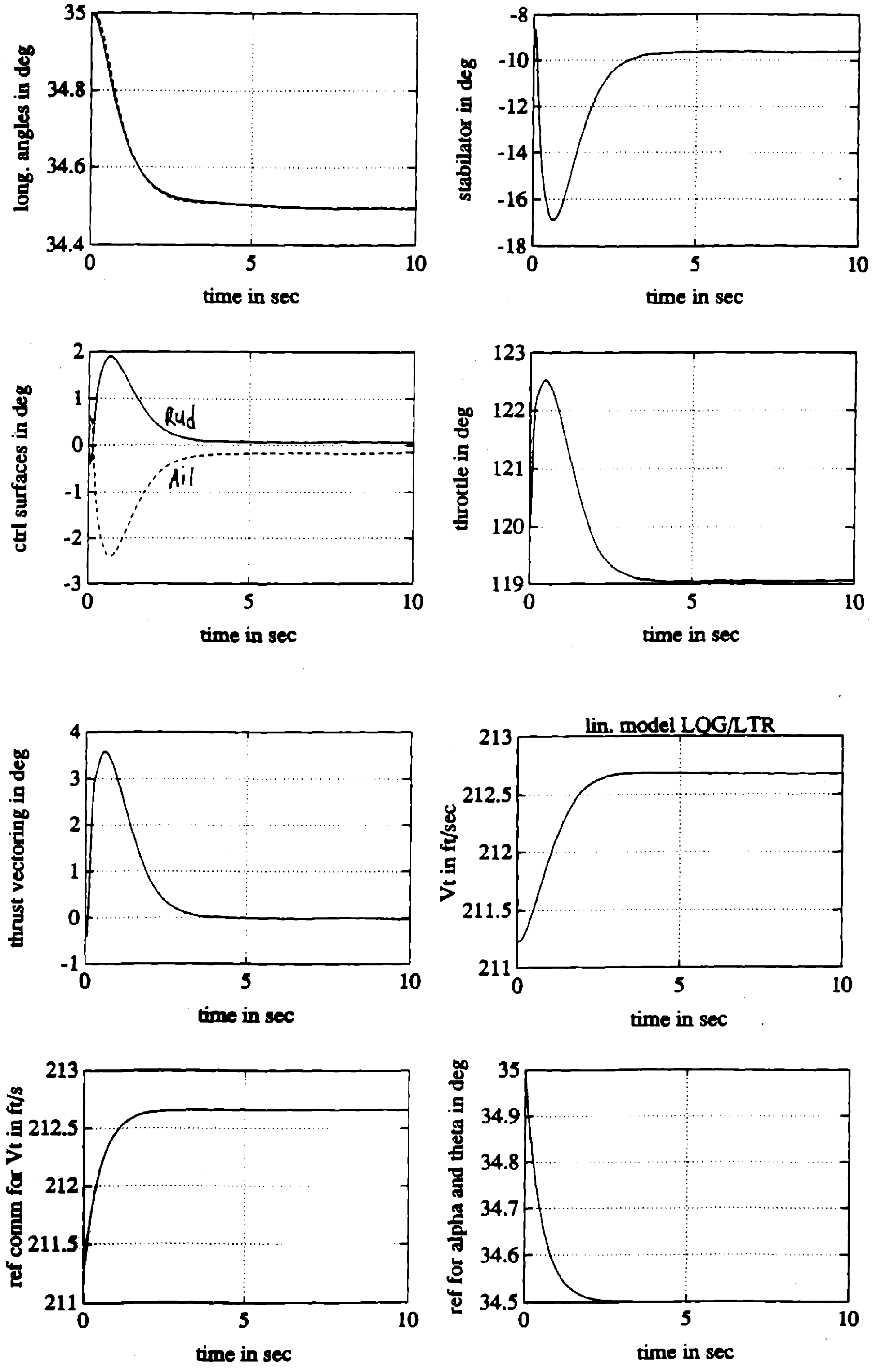

Figure 5.11 Tracking Response to Maneuver 3a for Design 1

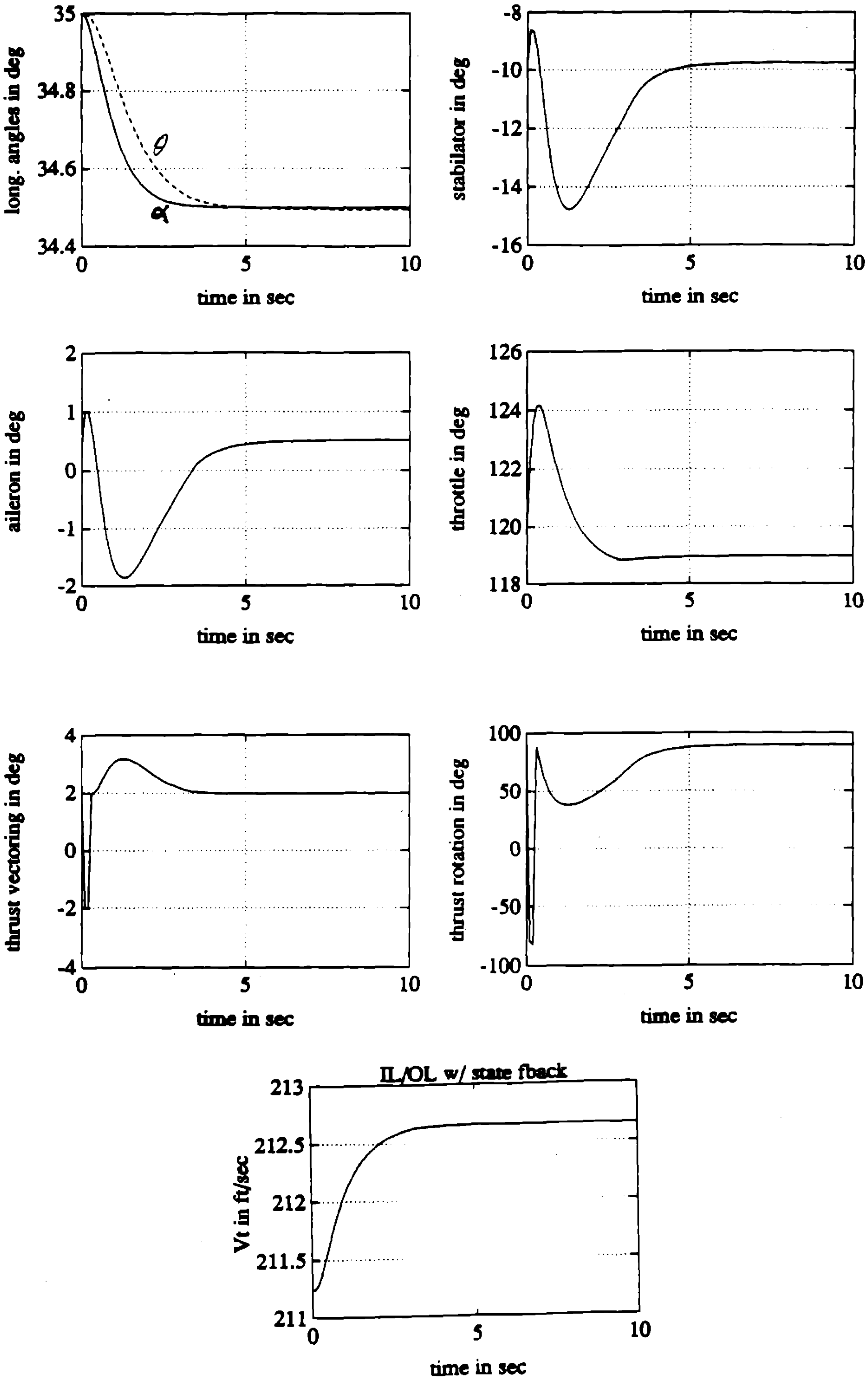

Figure 5.12 Tracking Response to Maneuver 3a for Design 2

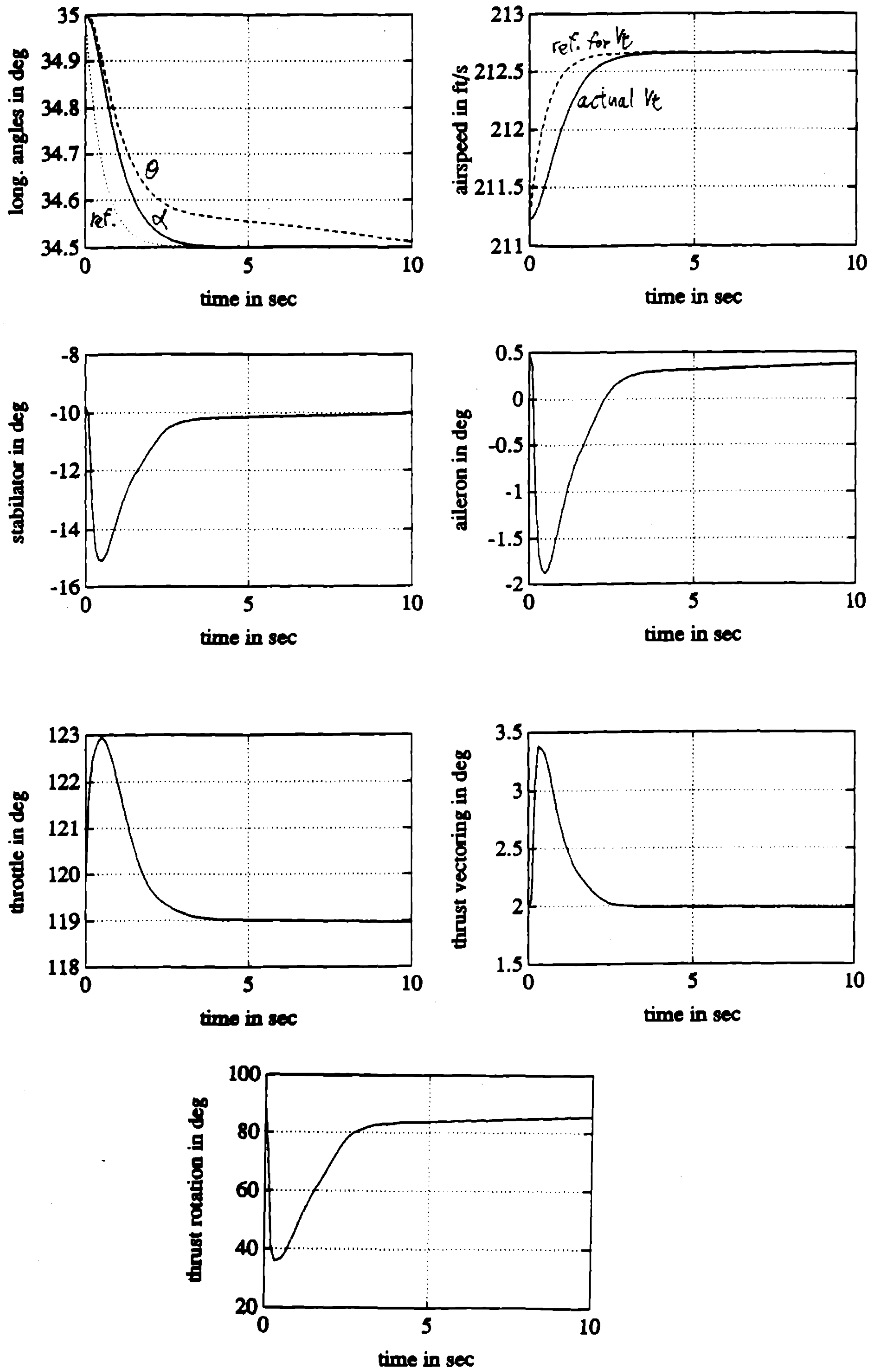

Figure 5.13 Tracking Response to Maneuver 3a for Design 3

The next maneuver (maneuver 3b) is similar to the last one, but it covers a bigger transition in α. In this maneuver, we command the aircraft to switch from the level trim at h = 15000 ft, and α=35° to another level trim at h = 15000 ft , and α=33°. This corresponds to commanding V_t from 211.231 ft/sec to 217.603 ft/sec, α from 35° to 33°, and θ from 35° to 33°. Since this maneuver represents a bigger transition than the previous one, we are decreasing the bandwidth of the reference command prefilter to avoid the anticipated control saturation. The transfer function of the prefilter used here is $G_{pf2}(s) = 0.4/s+0.4$. The results of the time simulation are presented in Figure 5-14 to Figure 5-16.

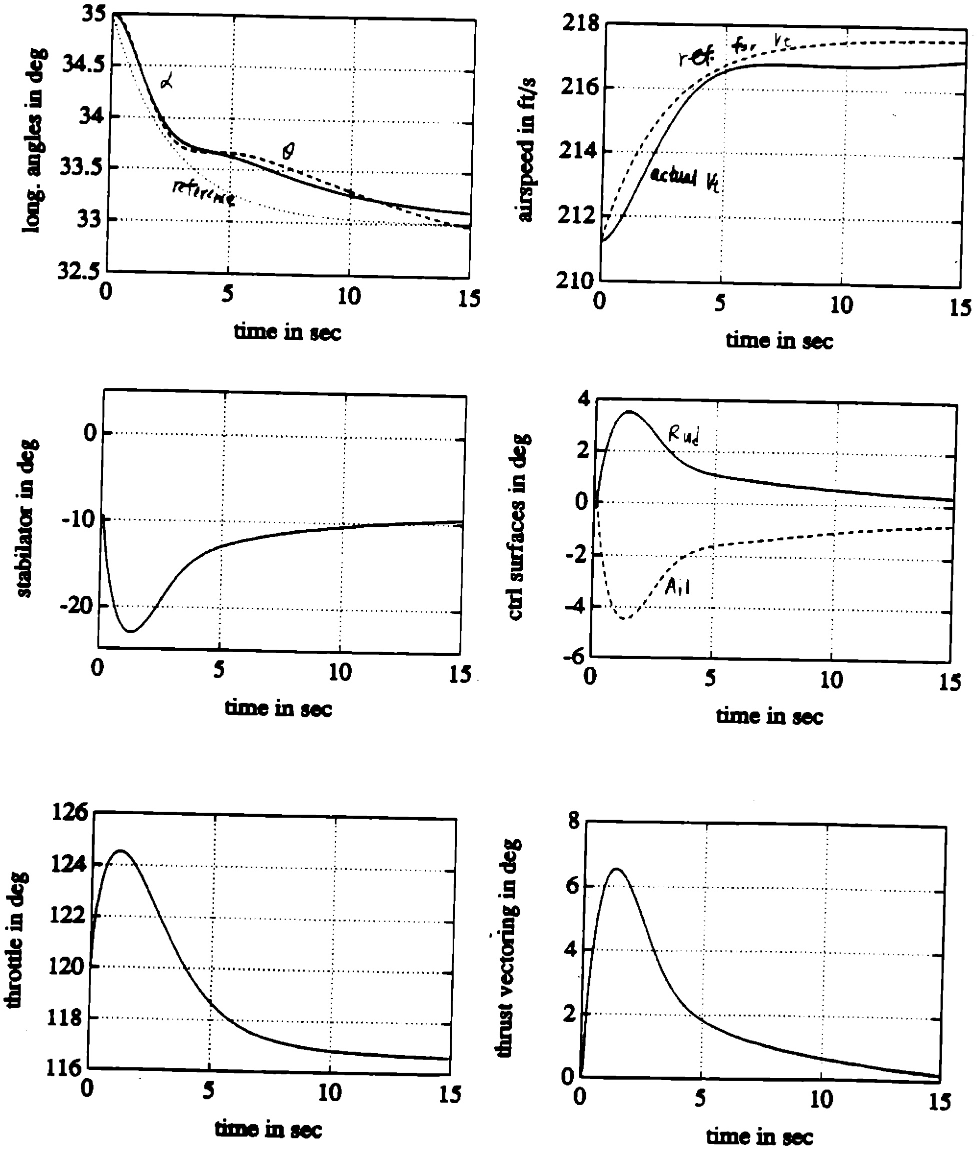

Figure 5.14 Tracking Response to Maneuver 3b for Design 1

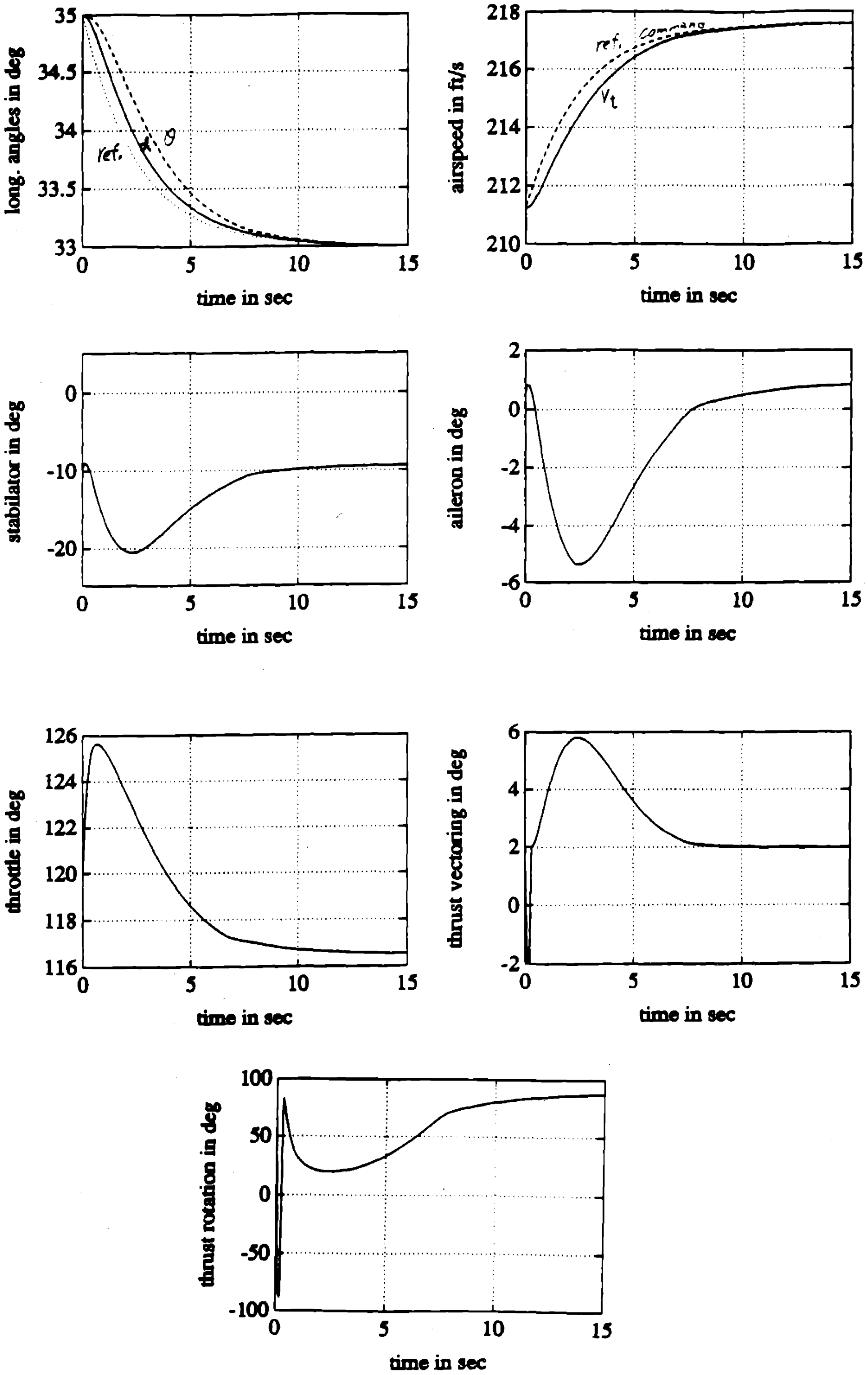

Figure 5.15 Tracking Response to Maneuver 3b for Design 2

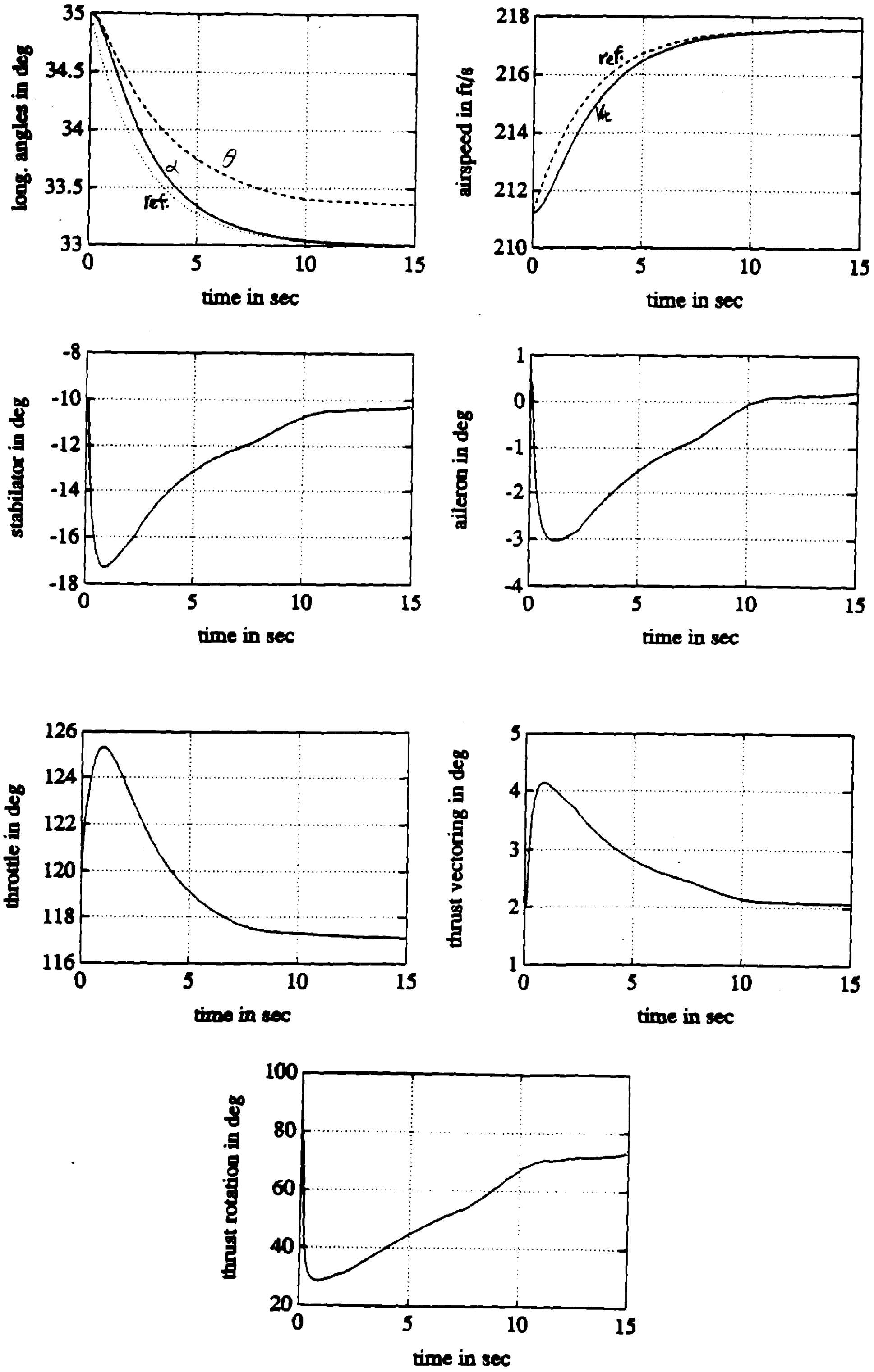

Figure 5.16 Tracking Response to Maneuver 3b for Design 3

In maneuver 3a, both Design 1 and Design 2 do well in the tracking response. The time histories for the outputs and controls are very similar in both designs. For Design 3, we expect the same problem in the pitching control while the response in α looks very good. In this maneuver, the airplane is still very close to the trim point about which the controllers are designed. In maneuver 3b, we are forcing the vehicle to venture outside farther from the design trim point, and the effects of the α-nonlinearities on the aerodynamics are more prominent than in maneuver 3a. Indeed, we see the performance of Design 1 deteriorated considerably in maneuver 3b than in maneuver 3a, while Design 2 seems hardly affected by this larger excursion in α during the maneuver. The large tracking errors of Design 1 in maneuver 3b really show the limitation of the linear trim point model of the vehicle dynamics. A merely 2-degree maneuver in α is enough to demonstrate the small validity region of the linear design model and the resulting drastic deterioration of off-design performance of the linear controller based on it. Although Design 3 has difficulty in controlling θ, it does not seem to be particularly affected by the α-nonlinearities. The problem with Design 3 is with the outer-loop. The inner-loop controller has performed its fair share in handling the α-nonlinearities. Consequently, we see that the nonlinear designs really have an edge over the design based on the trim point linear model.

5.4 Summary

The controller designs are evaluated and compared in this chapter using time simulation with the "real" nonlinear model of the vehicle obtained from NASA/Langley. The nonlinear designs are found to have an edge over the design based on the trim point linear model. However, Design 3 is hampered by a flawed outer-loop design which makes it an outcast in the comparison. A better LQG/LTR design (or other dynamic controller design) may be needed for the outer-loop design in Design 3 to allow for a fairer comparison, or dynamic controllers may be inherently unsuitable for the outer-loop design. A more thorough study is needed to substantiate this speculation. On the other hand, Design 2 proves to be the winner in the evaluation and comparison when hooked up with the "real" nonlinear model. The outer-loop pole-placement design of the decoupled systems using state feedback is found to be not only simple and elegant but also robust to the uncertainties and disturbances caused by the imperfect input-output linearization.

CHAPTER 6

CONCLUSIONS AND FUTURE RESEARCH

6.1 Conclusions

The goal of this thesis has been an exploration of the nonlinear design alternatives combining the nonlinear inversion/feedback linearization techniques and the robustness motivated inner-loop/outer-loop controller structure, while a comparison is also drawn to a baseline LQG/LTR design based on a trim point linear model. The substantial effort spent in understanding the nonlinear dynamics of the vehicle has proven to be well worthwhile when the superiority in performance of the nonlinear inner-loop/outer-loop controller design is demonstrated in the time simulation performed with the "real" nonlinear model of the vehicle provided by NASA/Langley. To achieve a similar level of performance using gain scheduling techniques with linear designs, one may have to choose a big selection of operation points to carry out designs and tie them together by some kind of gain scheduling algorithm. This does not seem to be a trivial task at all. Besides, given the severe nonlinearities for the vehicle at high α, it is doubtful that a gain-scheduling approach could even be practical. This again justifies our heavy initial investment in understanding the nonlinear dynamics of the vehicle. One may argue that the nonlinear designs require a lot of nontrivial computations in real time. However, with the continued success in the semiconductor industry in developing powerful microprocessors, math-coprocessors, DSP

(Digital Signal Processing) and RISC (Reduced Instruction Set Computer) chips, the computation burden does not seem to be a big problem at all.

The superior performance of the nonlinear design over the traditional linear model based LQG/LTR design provides very encouraging support for the application of nonlinear design methods for flight controls at high angles of attack. The study conducted in this thesis is only the beginning for further research in the area of nonlinear flight controls at high α. A number of issues still need to be addressed. However, judging by the results obtained in this study, nonlinear designs combining the inner-loop/outer-loop controller structure look very promising and seem to be the way to go for the flight control of high-performance vehicle at high α.

6.2 Directions for Future Research

One of the important issues that remain to be addressed is the quantification of the modelling errors, resulting from feedback linearization, and the subsequent robust design of the outer-loop controller. As we saw in Chapter 4 and Chapter 5, Design 3 fares well with the nominal design model, but it fails miserably in time simulation with the "real" nonlinear model. The outer-loop controller in Design 3 is very sensitive to the imperfect input-output linearization. More efforts are needed for the study of the modelling errors facing the outer-loop controller, so we can design the outer-loop controller accordingly. Besides, we mentioned in Chapter 3 that in the nonlinear model used for the input-output linearization (equation 3-6a and 3-6b), the G matrix in equation 3-6a is actually a function of both the state and the control, but we ignored the control dependency when we performed the input-output linearization in the inner-loop controller. It is debatable that we may be able to get better results if we include the control dependency in the inner-loop controller, instead of ignoring the dependency in the first place and designing a robust outer-loop controller to make up for the error in the input-output linearization. So far, there is no current design method that incorporates the control dependency of the G matrix in feedback linearization. Further research in new theory and design methodologies is needed to address this issue.

Another issue that needs further study is the maneuvers we pick to evaluate the controller designs. High-α flights are really pushing the limits of the aircraft. Some maneuvers may be just impossible with the limitations imposed by the aerodynamic characteristics of the aircraft. Besides, in real-life maneuvers, all the outputs are involved at the same time. Well chosen test case maneuvers for the controller evaluation should include good co-ordination among the various output variables. For example, in the bank-to-turn maneuver, both the heading and roll angles are involved, at the very least. The artificial 0.1° heading step in Chapter 5 is picked out of convenience. More realistic maneuvers may provide better information about the controller performance. In addition, the step commands are passed through a prefilter to limit the bandwidth of the reference commands, thus avoiding control saturation. A realistic maneuver should have taken this into account, thus getting rid of the prefilter to avoid control saturation in the simulations. Finally, since we bring up the issue of saturation, further work is needed to study the effects of control saturation (which is nonlinear in nature). In [13], Kapasouris has dealt with saturation explicitly in linear system. One should consider applying or extending the methodology developed there for the nonlinear system that we are dealing with.

APPENDIX A

VARIATION OF THE STABILITY DERIVATIVES WITH THE ANGLE OF ATTACK

A.1 Variation of the Aerodynamic Coefficients with α (Fixed Controls)

The following figures (Figure A.1 to Figure A.3) show the variation of the aerodynamic coefficents with α.

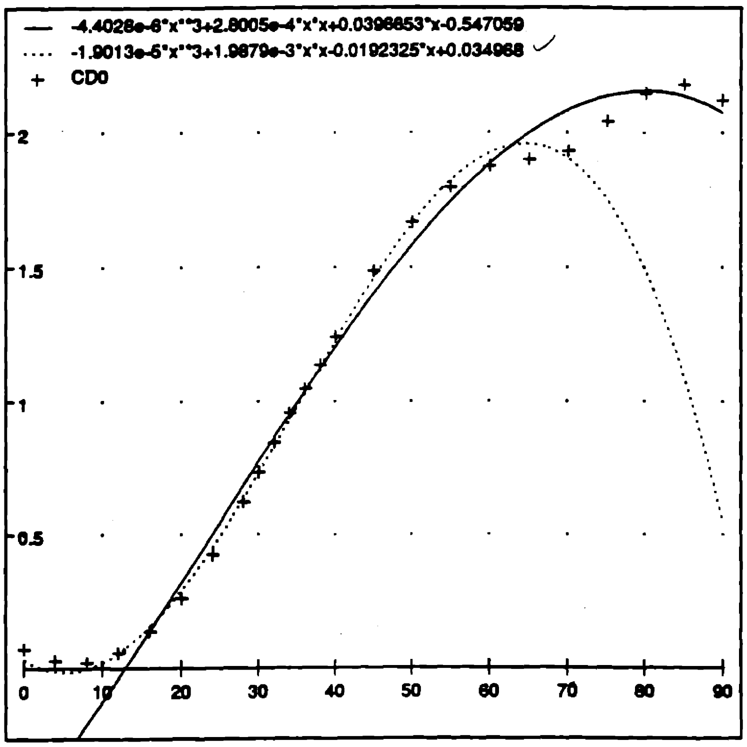

Figure A.1 C_{D0} vs. α

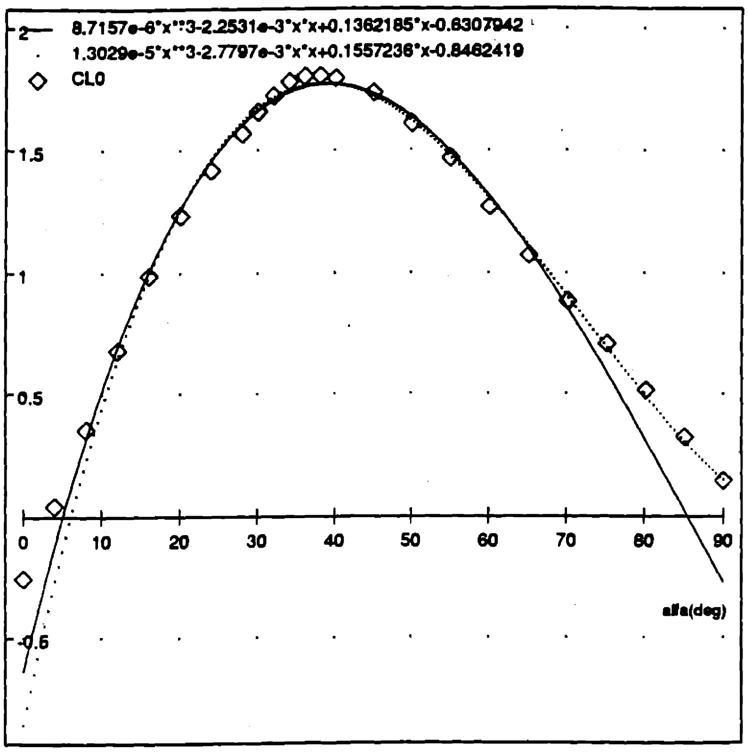

Figure A.2 C_{L0} vs. α

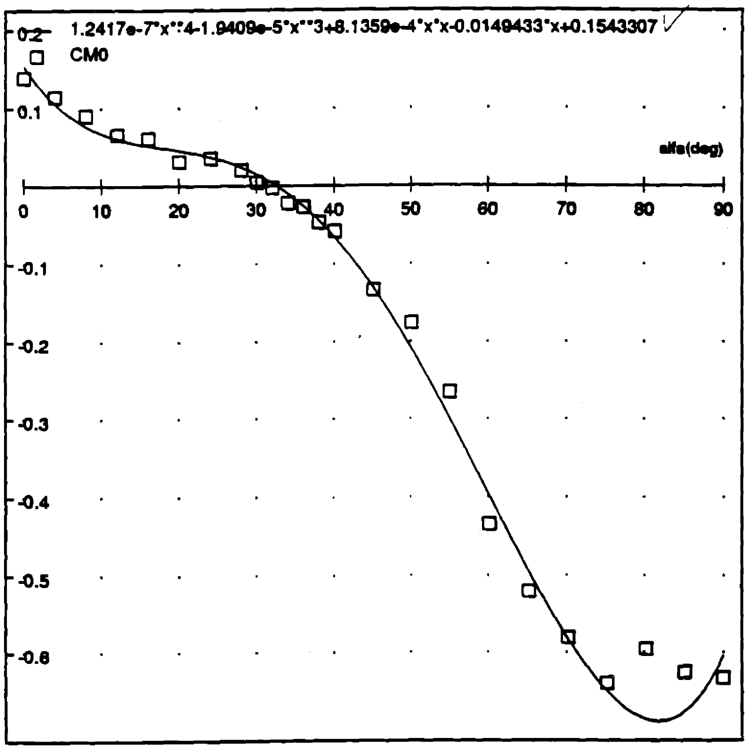

Figure A.3 C_{M0} vs. α

A.2 Variation of the Stability Derivatives Involving the States with α

The figures in this section show the plots of the stability derivatives involving the states vs. α.

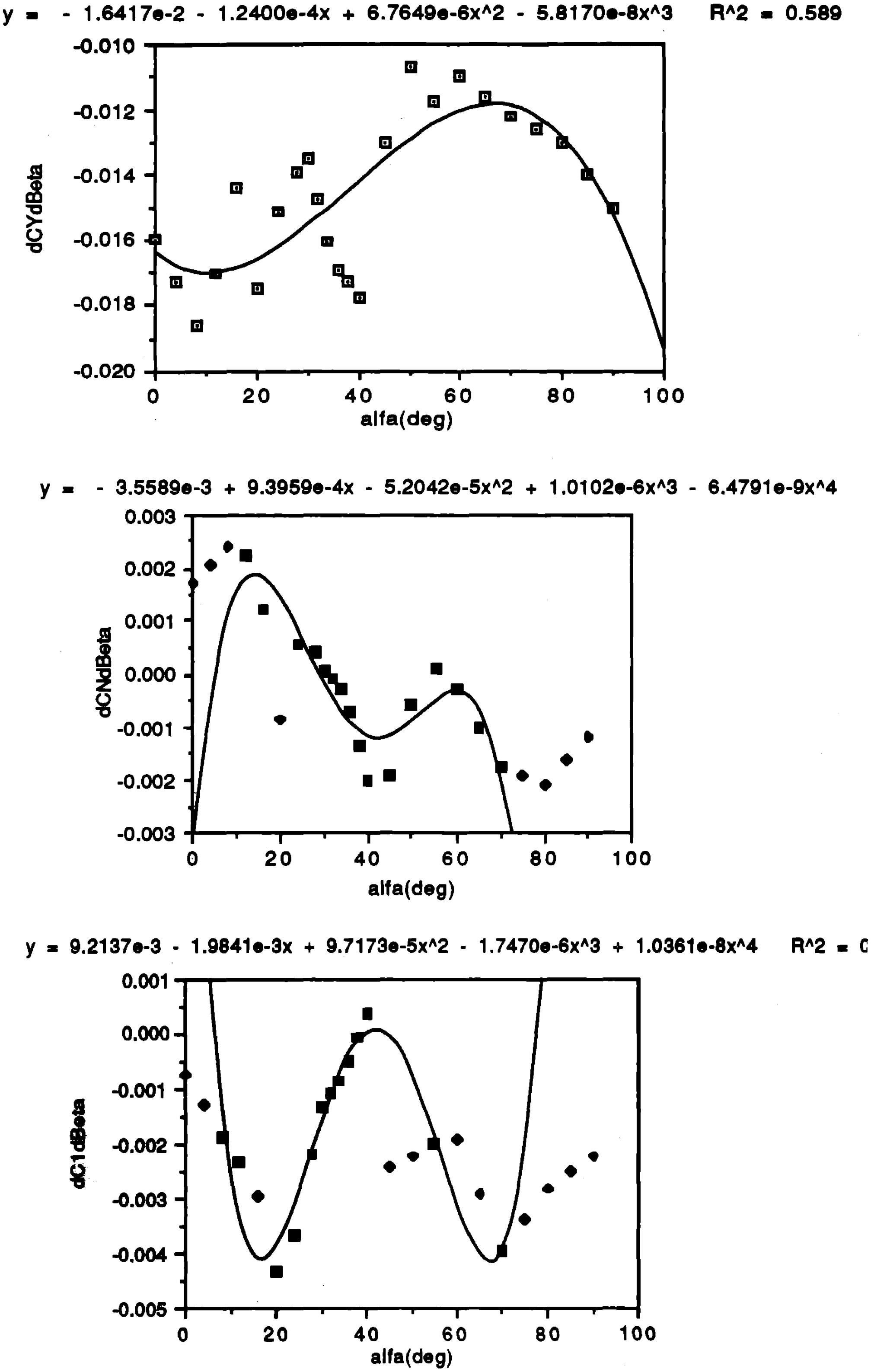

Figure A.4 Plots of the Stability Derivatives Involving β

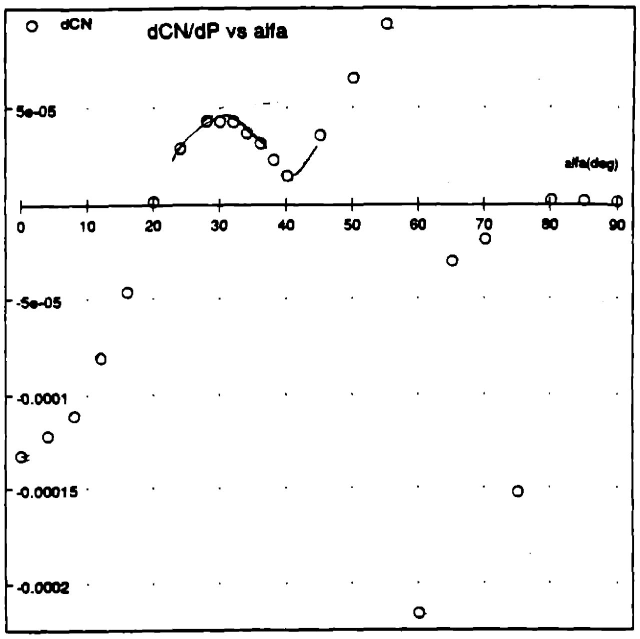

Figure A.5 $\partial C_N/\partial P$ vs. α

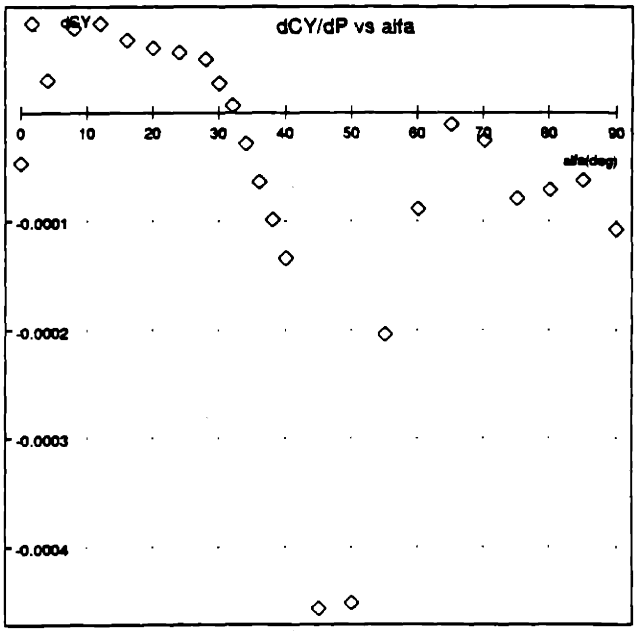

Figure A.6 $\partial C_Y/\partial P$ vs. α

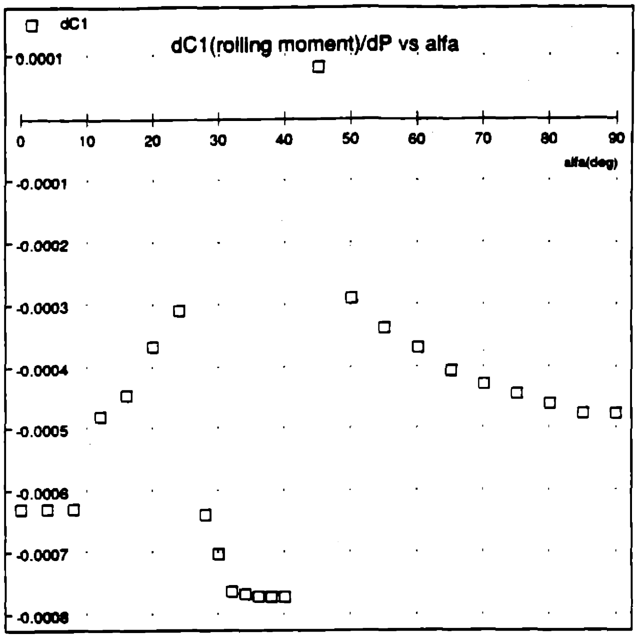

Figure A.7 $\partial C_1/\partial P$ vs. α

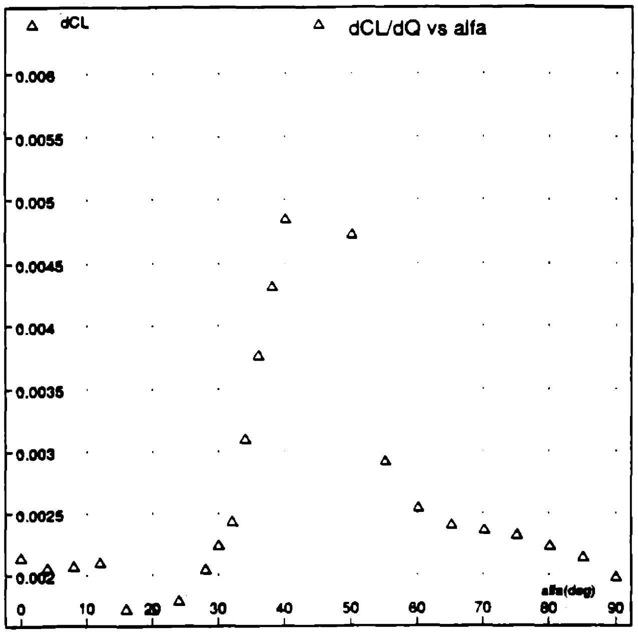

Figure A.8 $\partial C_L/\partial Q$ vs. α

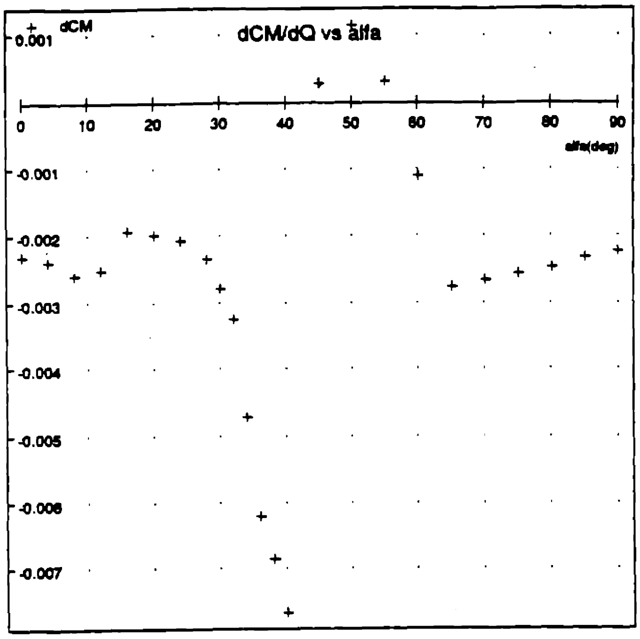

Figure A.9 $\partial C_M/\partial Q$ vs. α

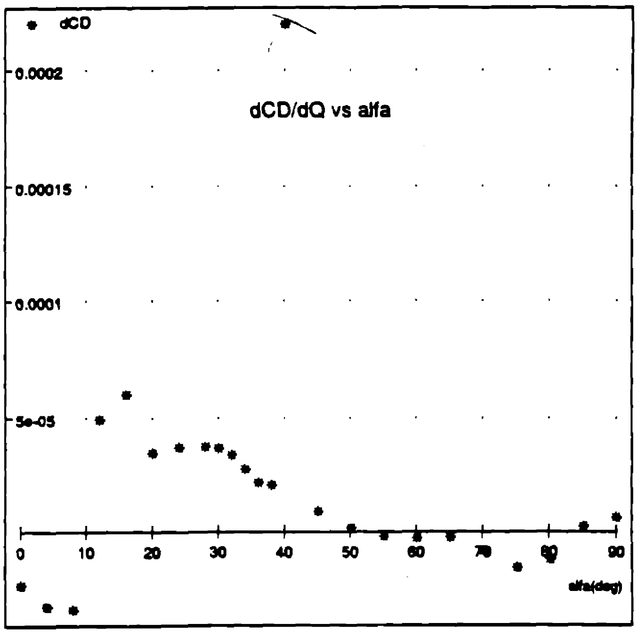

Figure A.10 $\partial C_D/\partial Q$ vs. α

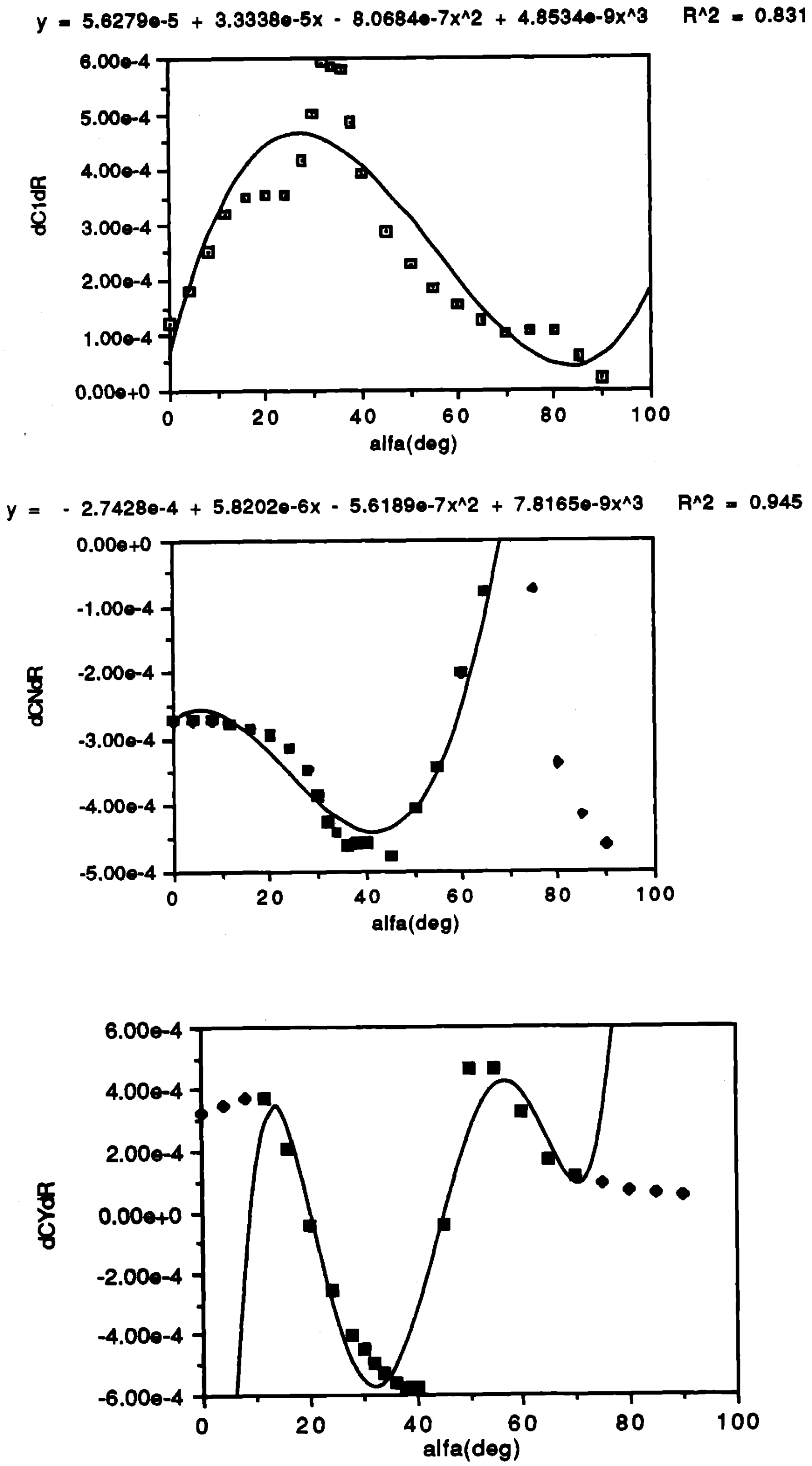

Figure A.11 Plots of the Stability Derivatives Involving R

A.3 Variation of the Stability Derivatives Involving the Controls with α

The following figures show the plots of the stability derivatives involving the aerodynamic controls vs α.

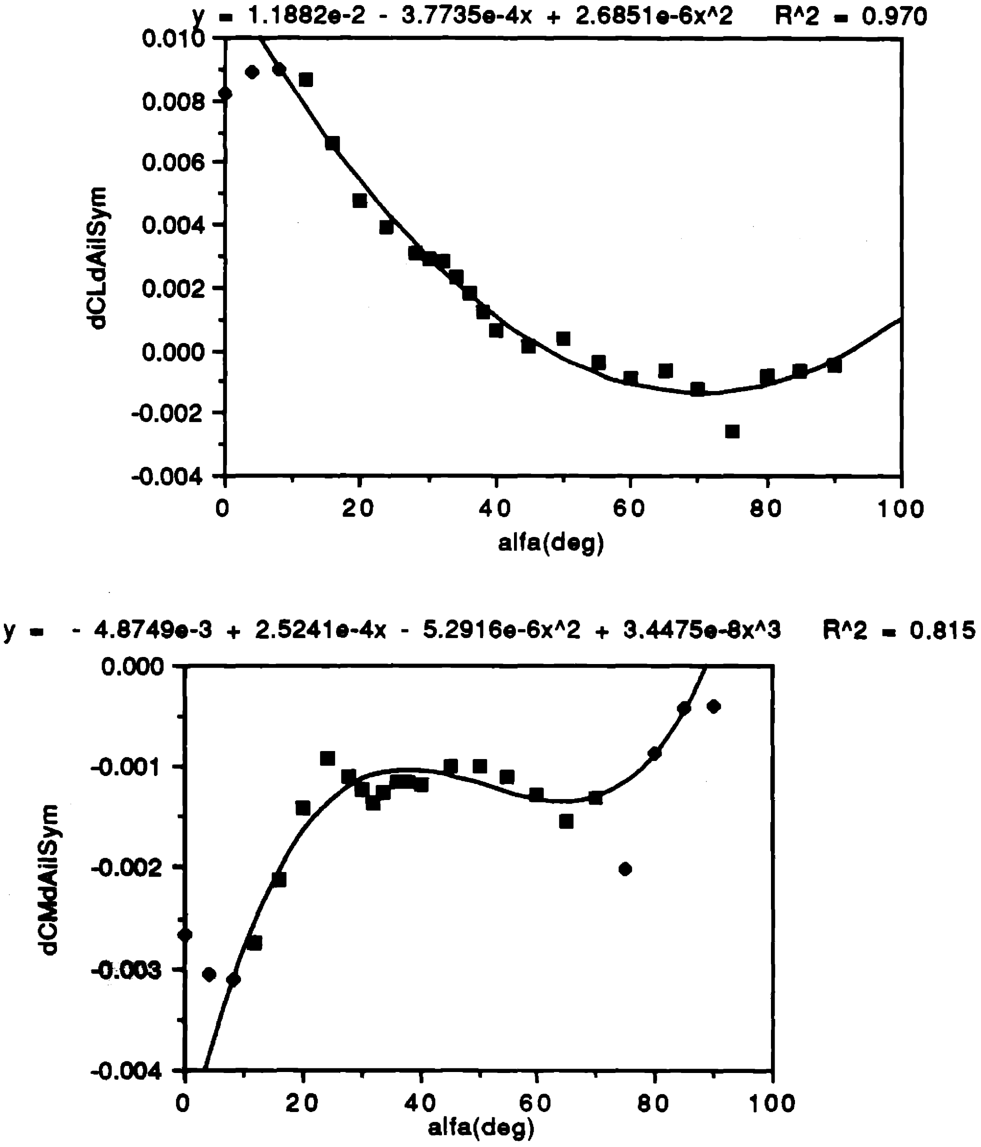

Figure A.12 Plots of the Stability Derivatives involving Ail_{sym}

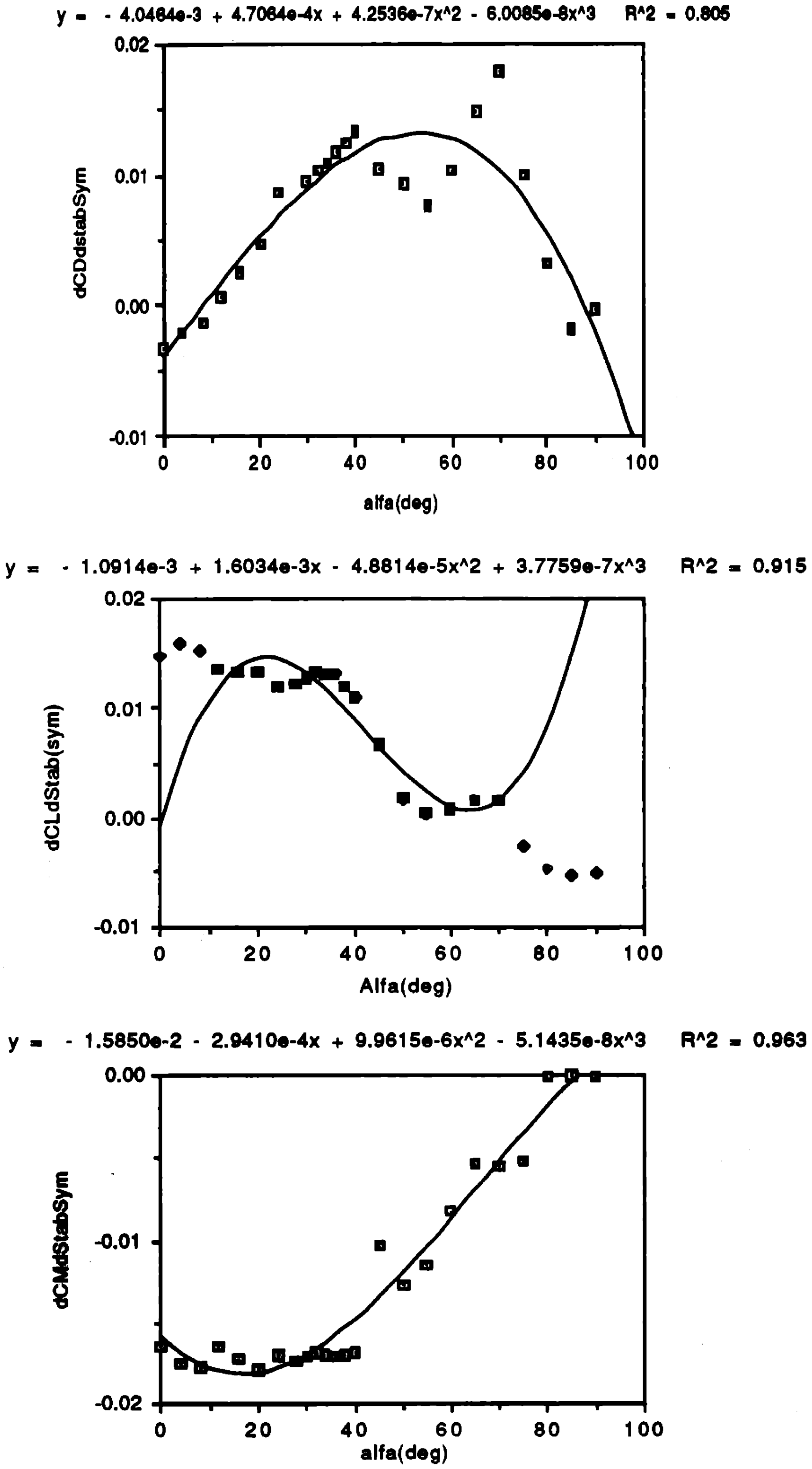

Figure A.13 Plots of the Stability Derivatives involving $Stab_{sym}$

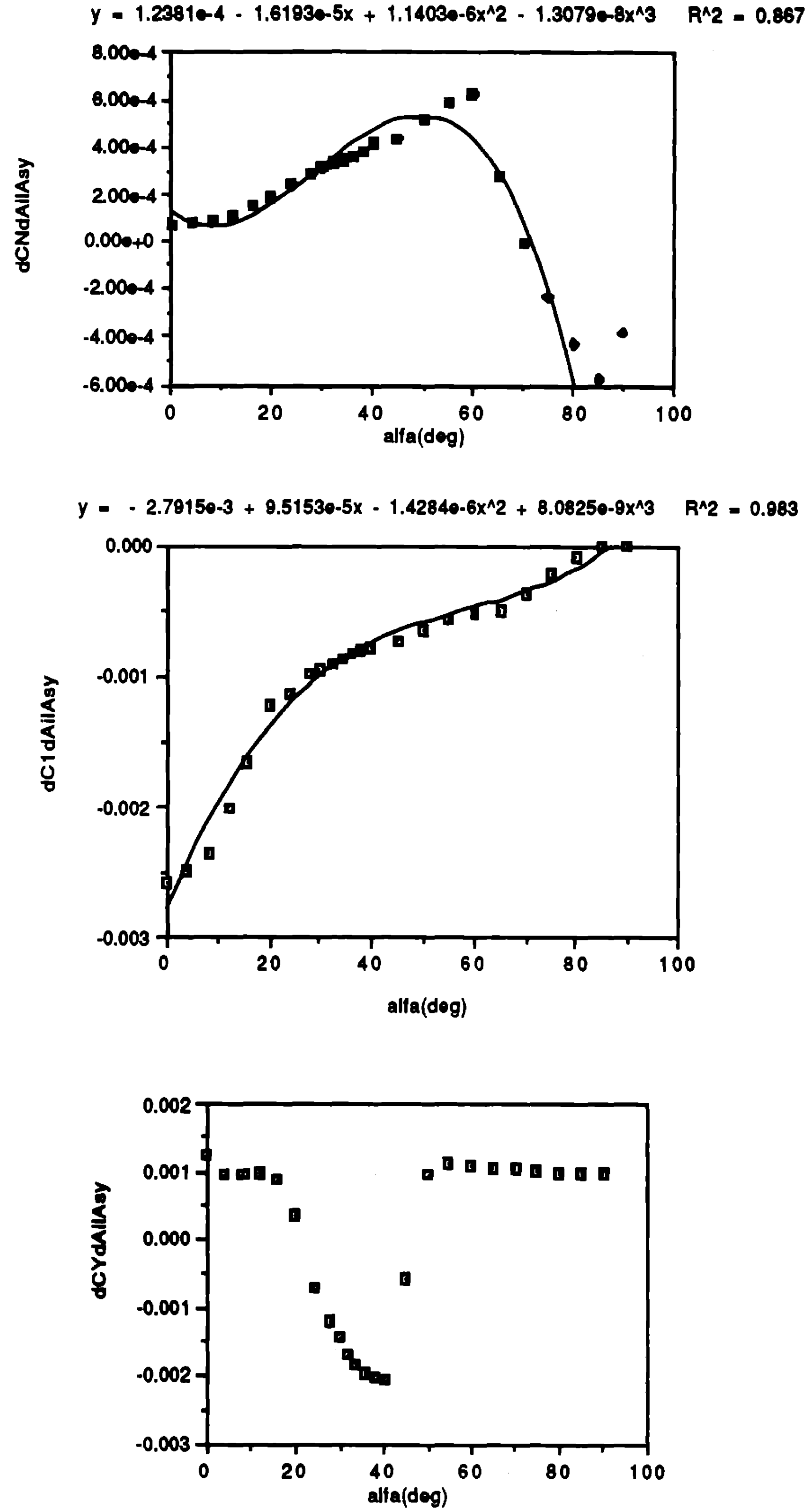

Figure A.14 Plots of the Stability Derivatives involving Ail_{asy}

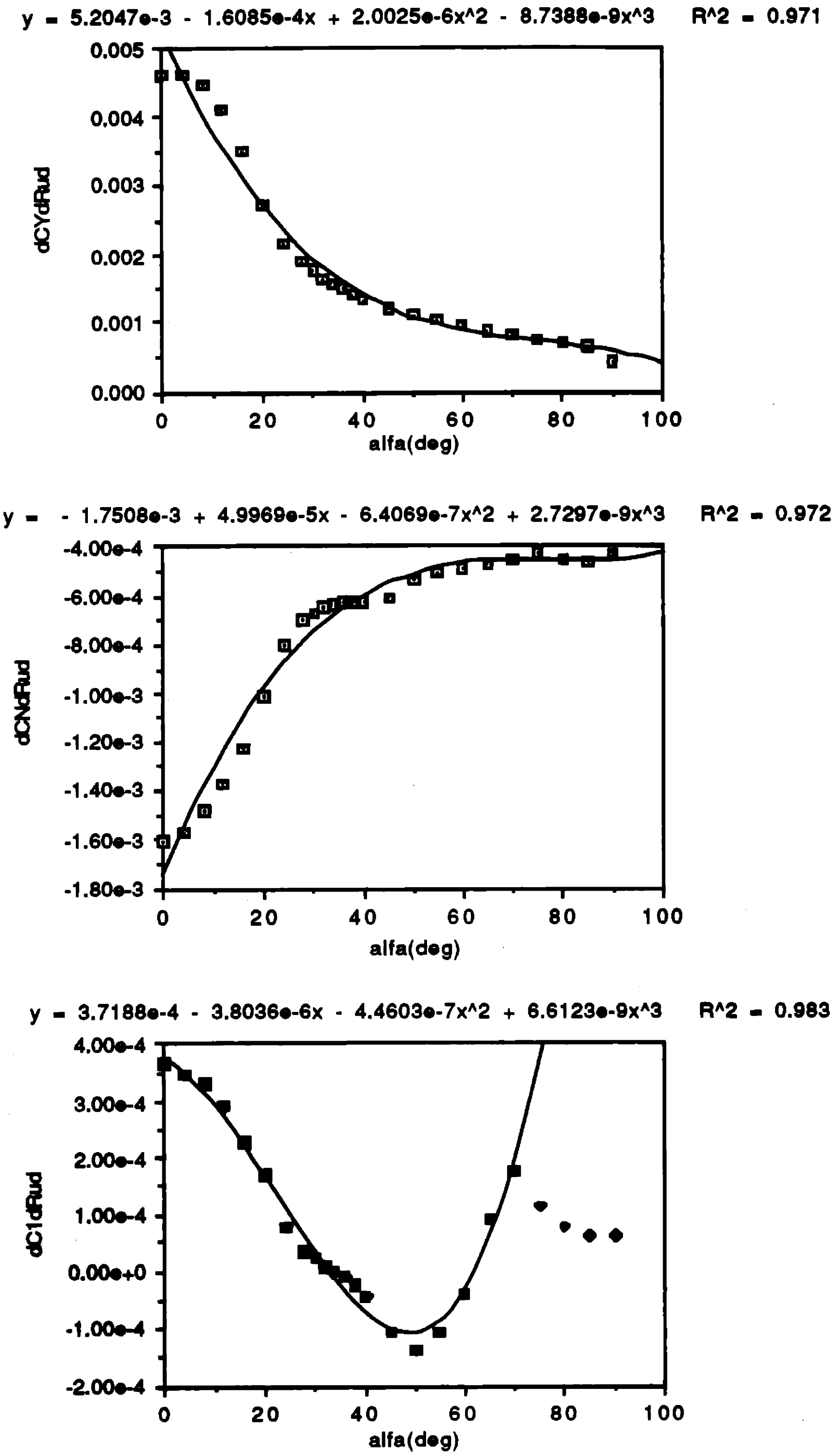

Figure A.15 Plots of the Stability Derivatives involving Rud y = 2.4291e-3 - 9.6536e-5x - 1.5765e-6x^2 + 3.1006e-8x^3 R^2 = 0.945

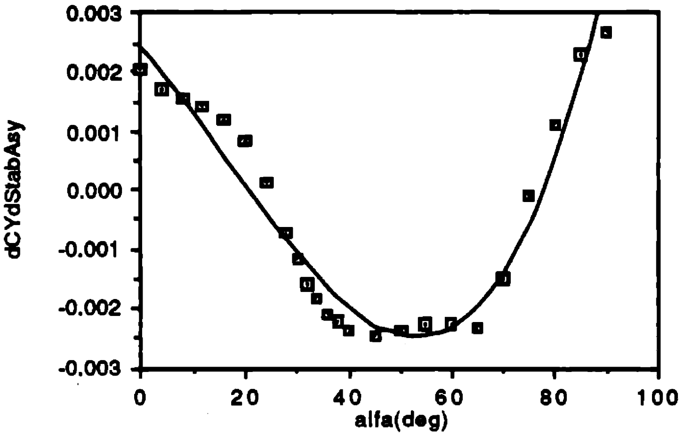

y = - 7.9911e-4 + 4.0899e-6x + 7.3918e-7x^2 R^2 = 0.989

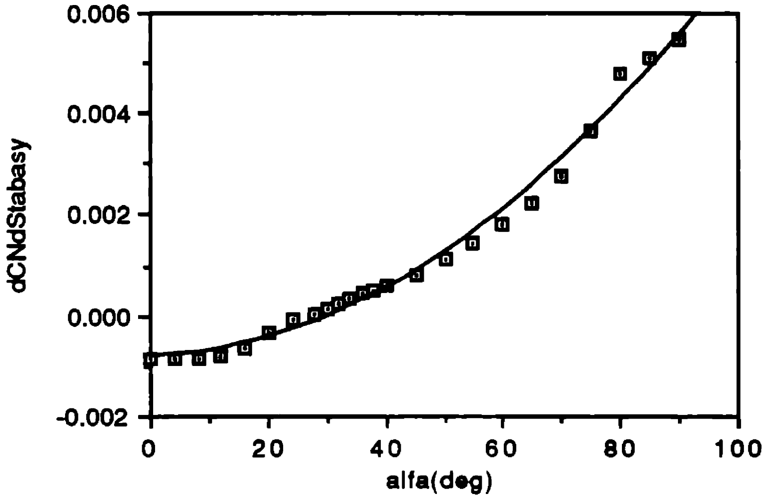

y = - 9.2140e-4 - 6.9644e-5x + 2.1245e-6x^2 - 1.3579e-8x^3 R^2 = 0.978

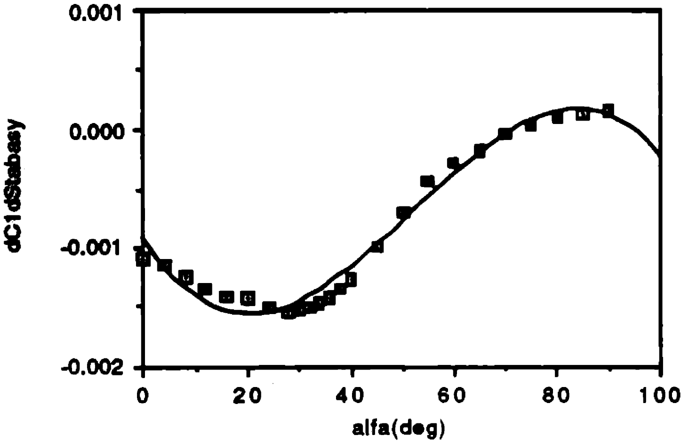

Figure A.16 Plots of the Stability Derivatives involving $Stab_{asy}$

APPENDIX B

TIME SIMULATION RESULTS FOR THE VERIFICATION OF THE NONLINEAR DYNAMICS MODEL

B.1 Time Simulations at Trim Point Number 1

The figures included in this section show the time simulation results of the two analytical models for the nonlinear dyanmics of the F18/HARV described in Section 2.5 at the following trim point,

altitude = 15000 ft
$\alpha = \theta = 35°$
$\beta = \phi = \psi = 0°$
$P = Q = R = 0°/\text{sec}$

(Note: Results from the "true" model obtained from Doug Arbuckle have labels ending in "true". Results from the analytical models described in Section 2.1 have labels ending in "1" and "2", corresponding to model 1 and model 2 respectively.)

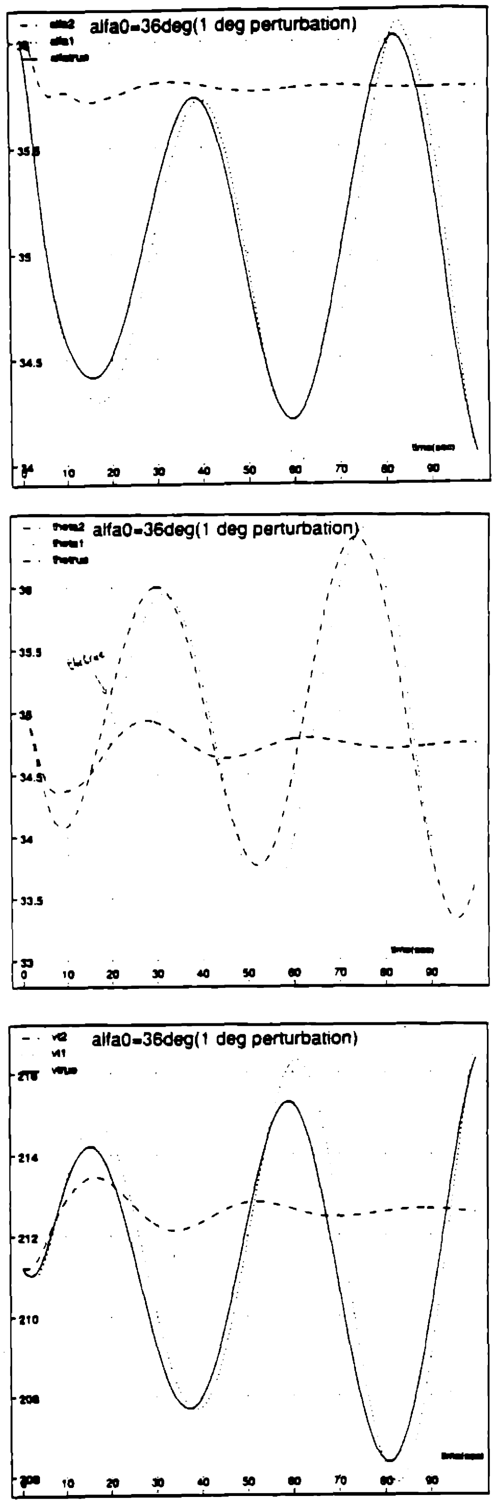

Figure B.1 Plots with α Perturbed by +1 deg from Trim

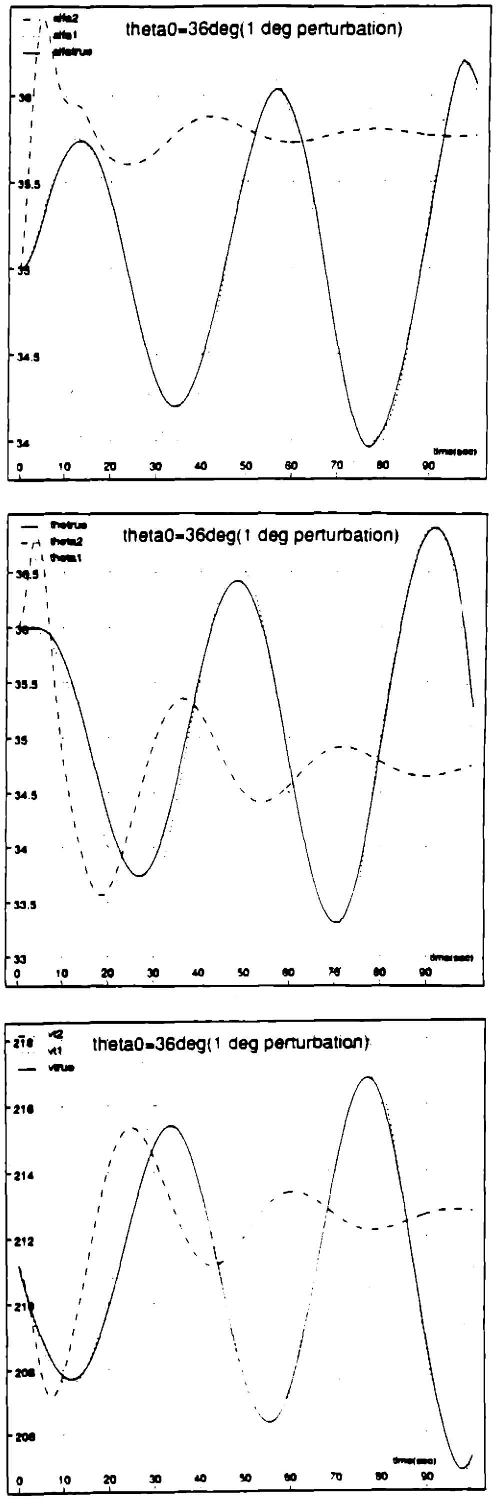

Figure B.2 Plots with θ Perturbed by +1 deg from Trim

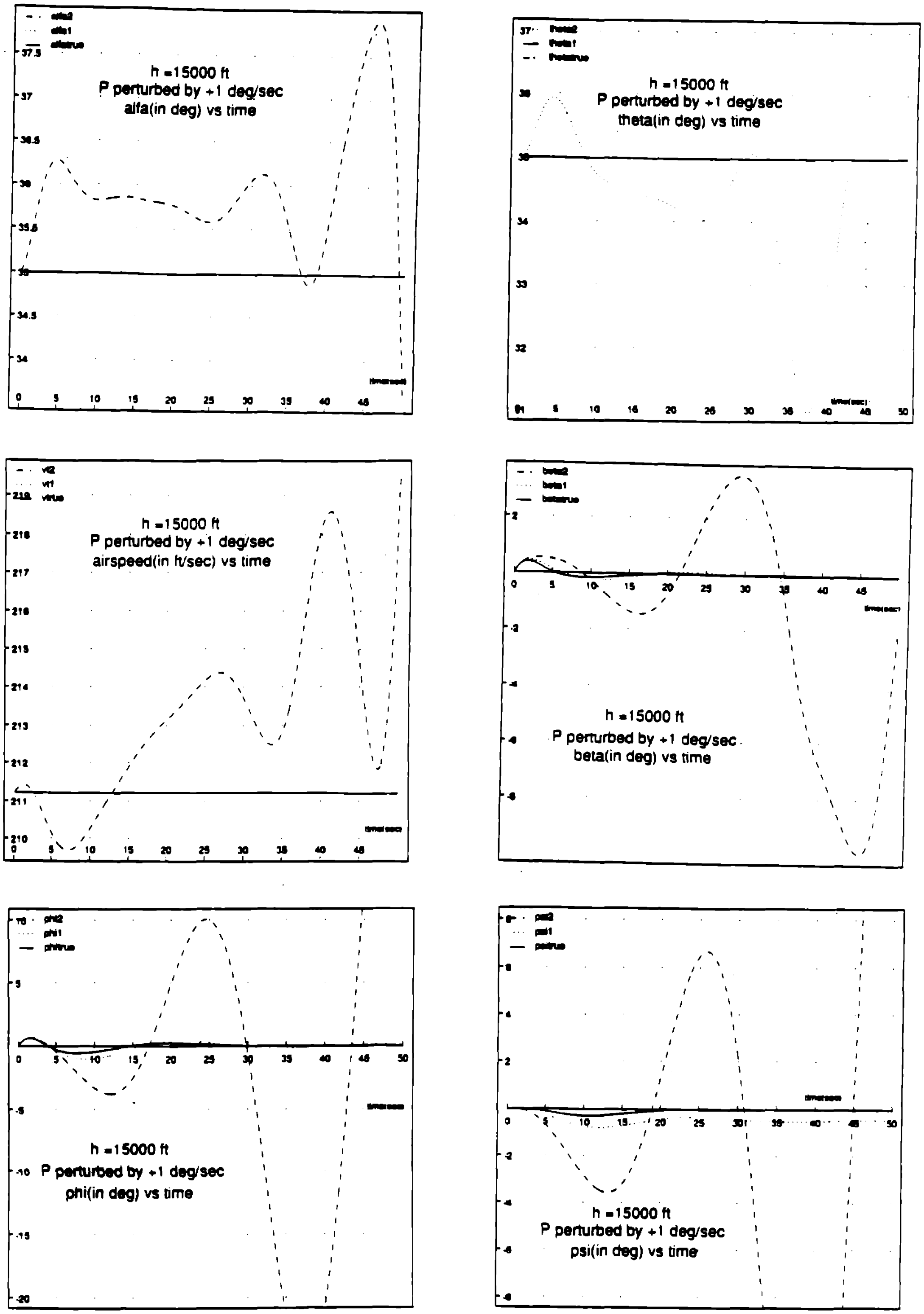

Figure B.3 Plots with P Perturbed by +1 deg/sec from Trim

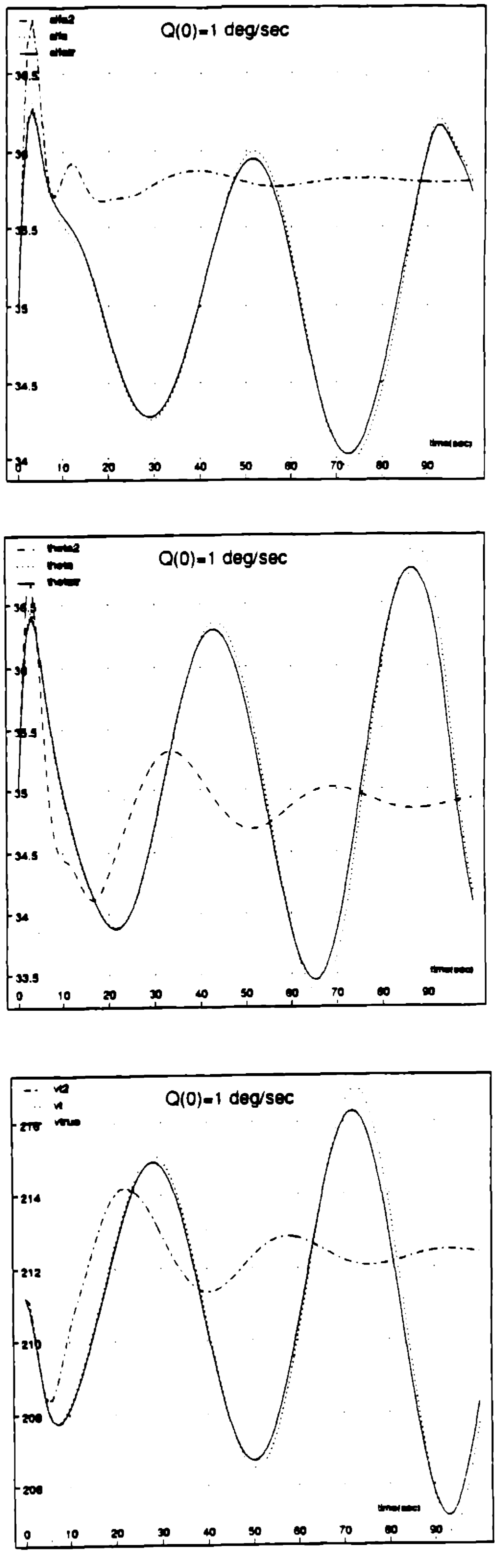

Figure B.4 Plots with Q Perturbed by +1 deg/sec from Trim

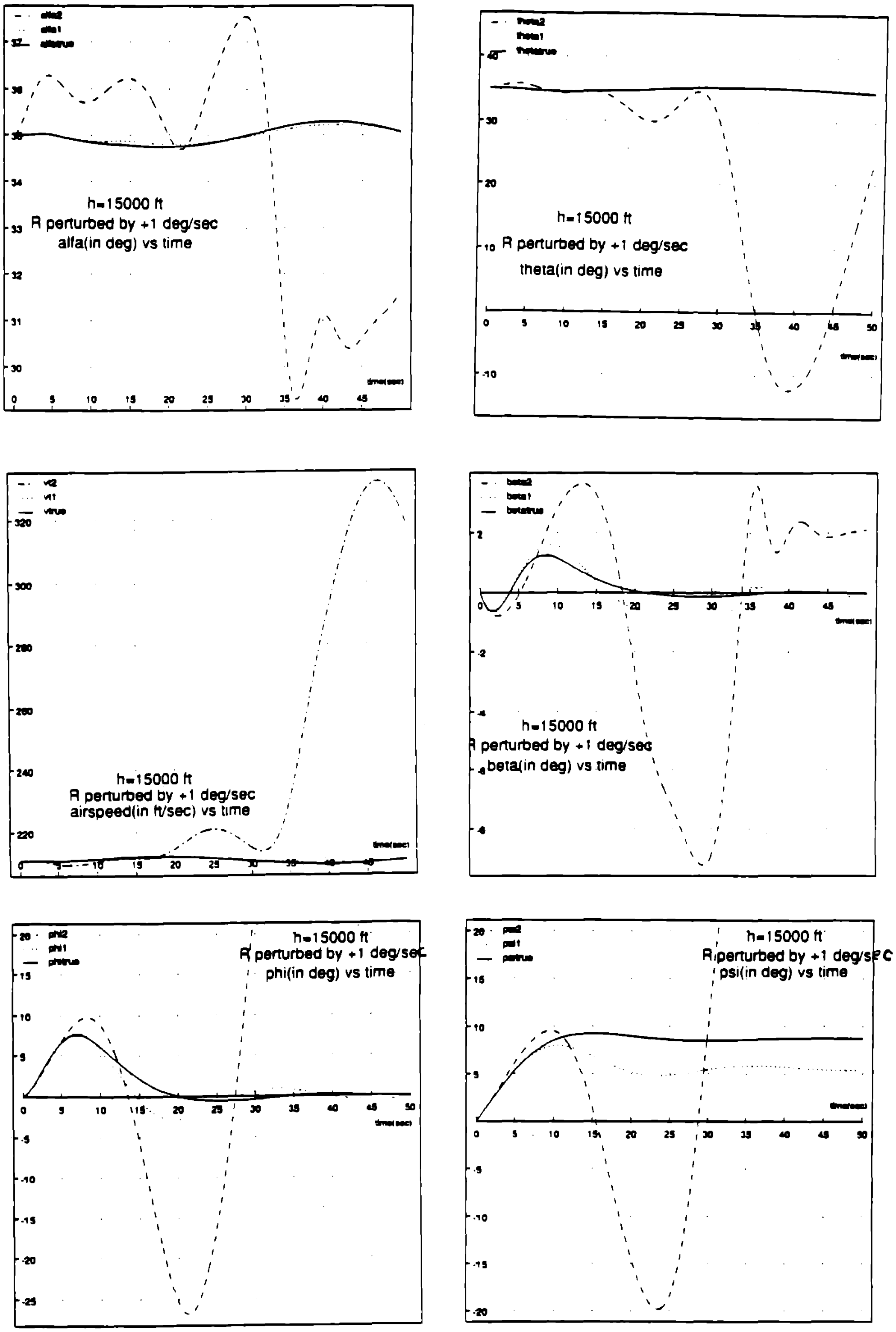

Figure B.5 Plots with R Perturbed by +1 deg/sec from Trim

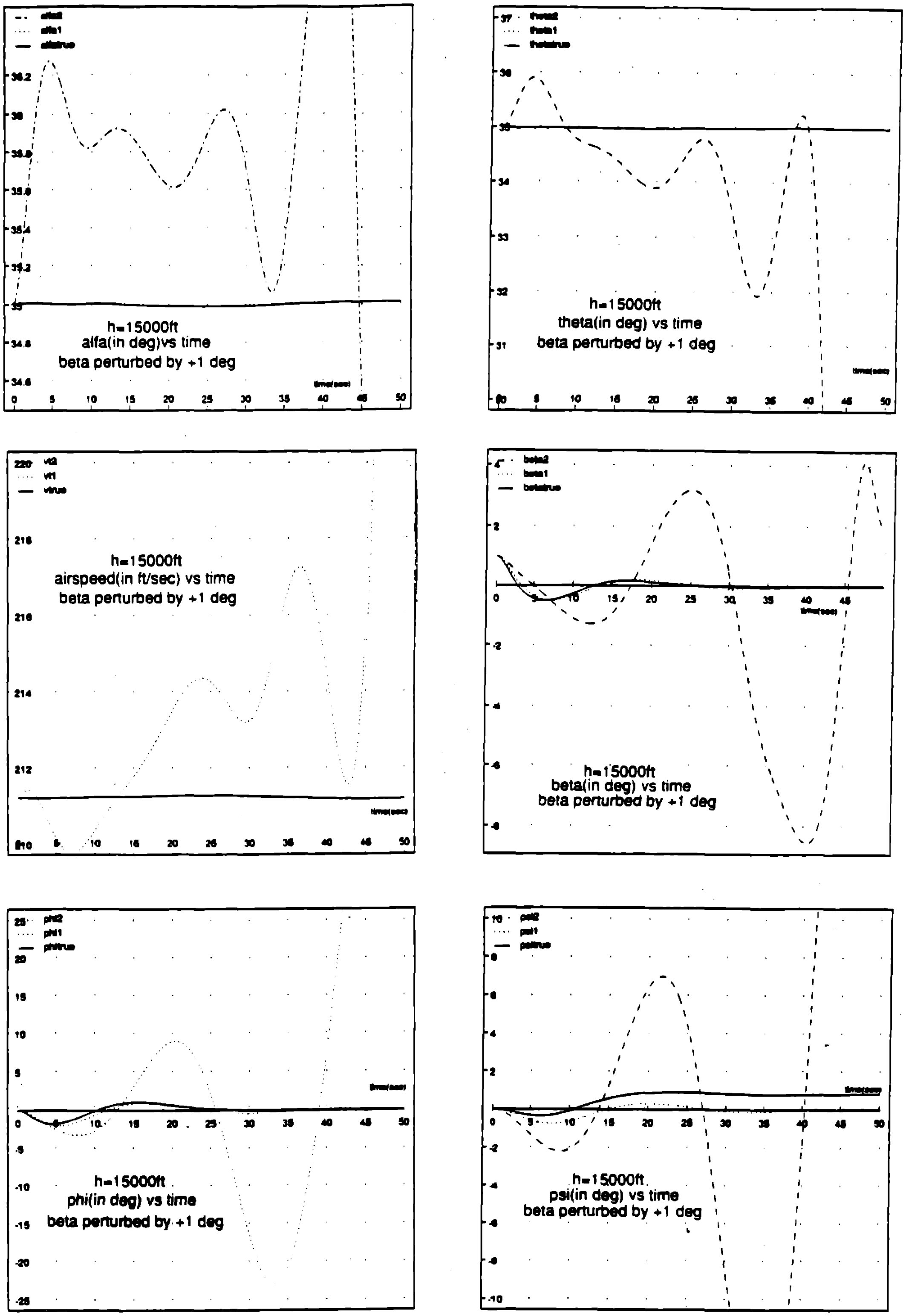

Figure B.6 Plots with β Perturbed by +1 deg from Trim

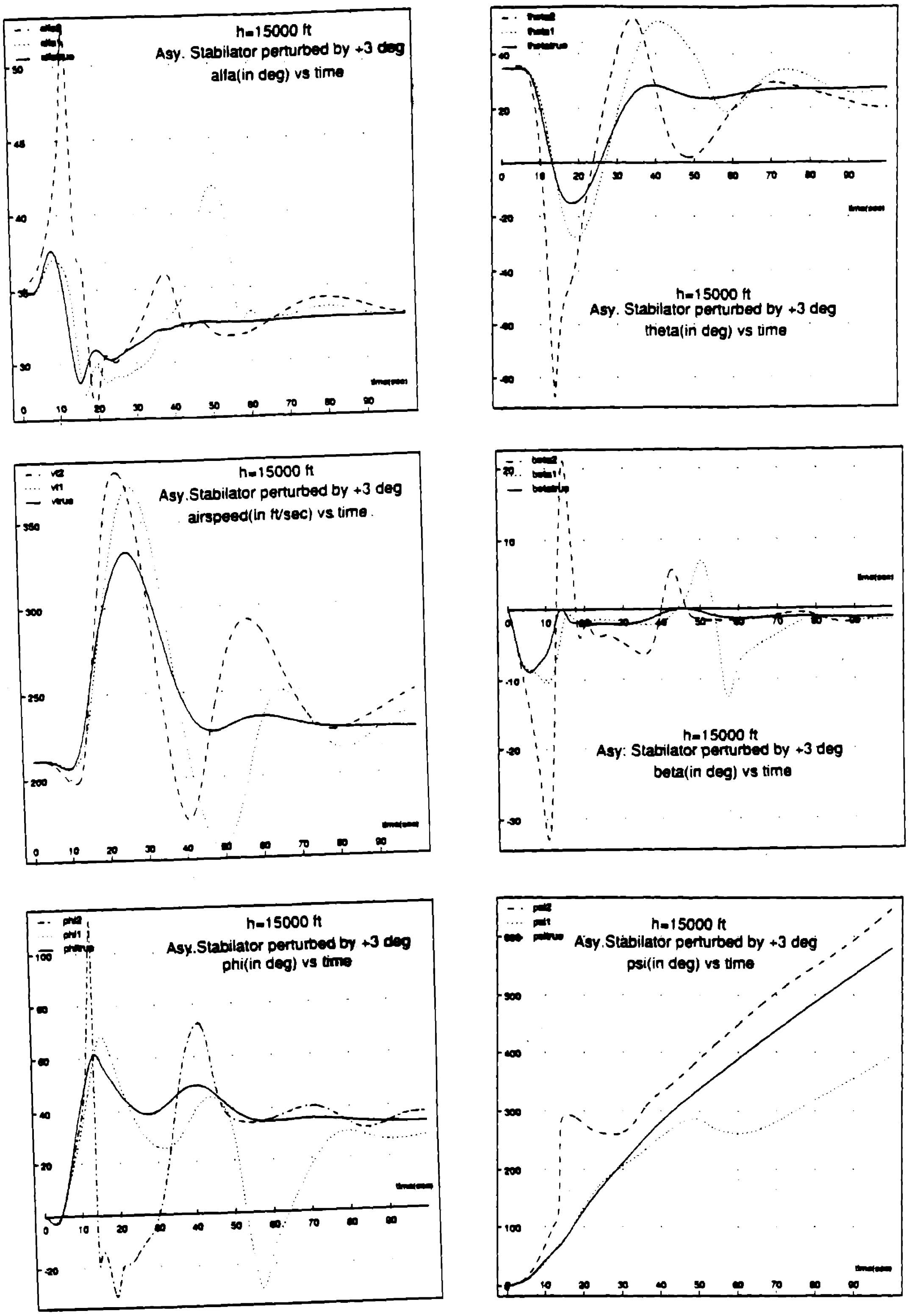

Figure B.11 Plots with Stab$_{asy}$ Perturbed by +3 deg from Trim

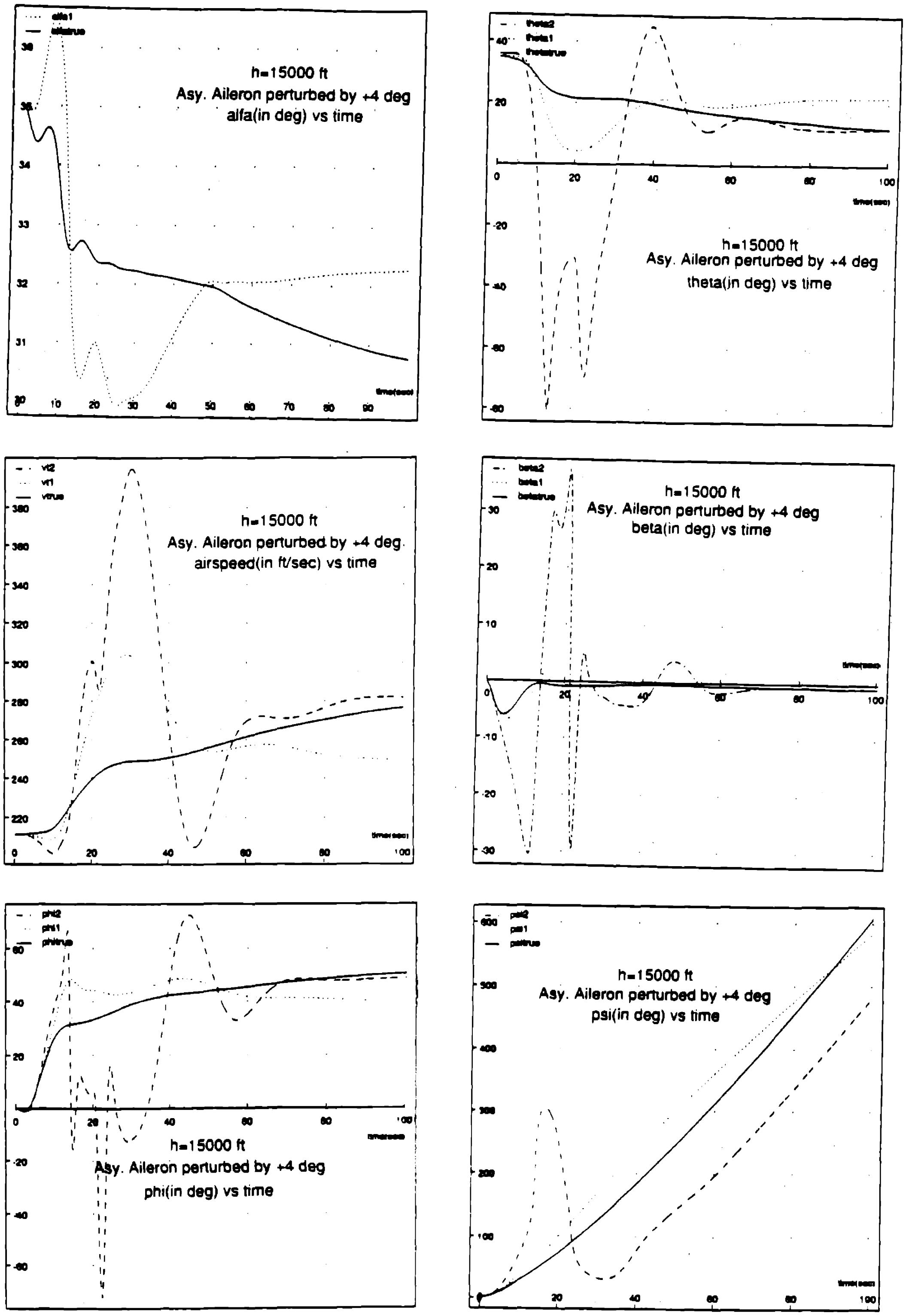

Figure B.12 Plots with Ail$_{asy}$ Perturbed by +4 deg from Trim

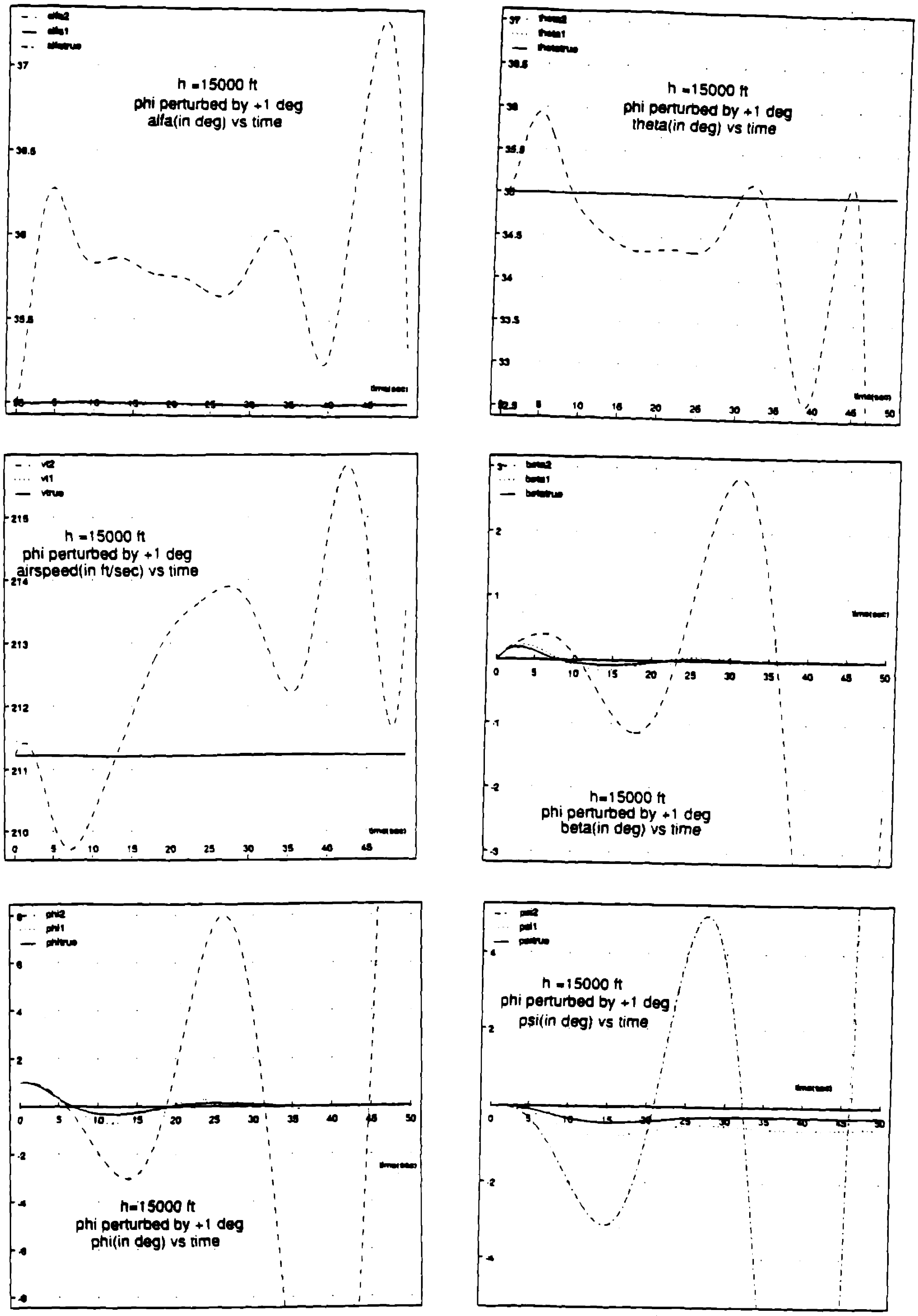

h =15000 ft
phi perturbed by +1 deg
alfa(in deg) vs time

h =15000 ft
phi perturbed by +1 deg
theta(in deg) vs time

h =15000 ft
phi perturbed by +1 deg
airspeed(in ft/sec) vs time

h=15000 ft
phi perturbed by +1 deg
beta(in deg) vs time

h=15000 ft
phi perturbed by +1 deg
phi(in deg) vs time

h =15000 ft
phi perturbed by +1 deg
psi(in deg) vs time

Figure B.7 Plots with ϕ Perturbed by +1 deg from Trim

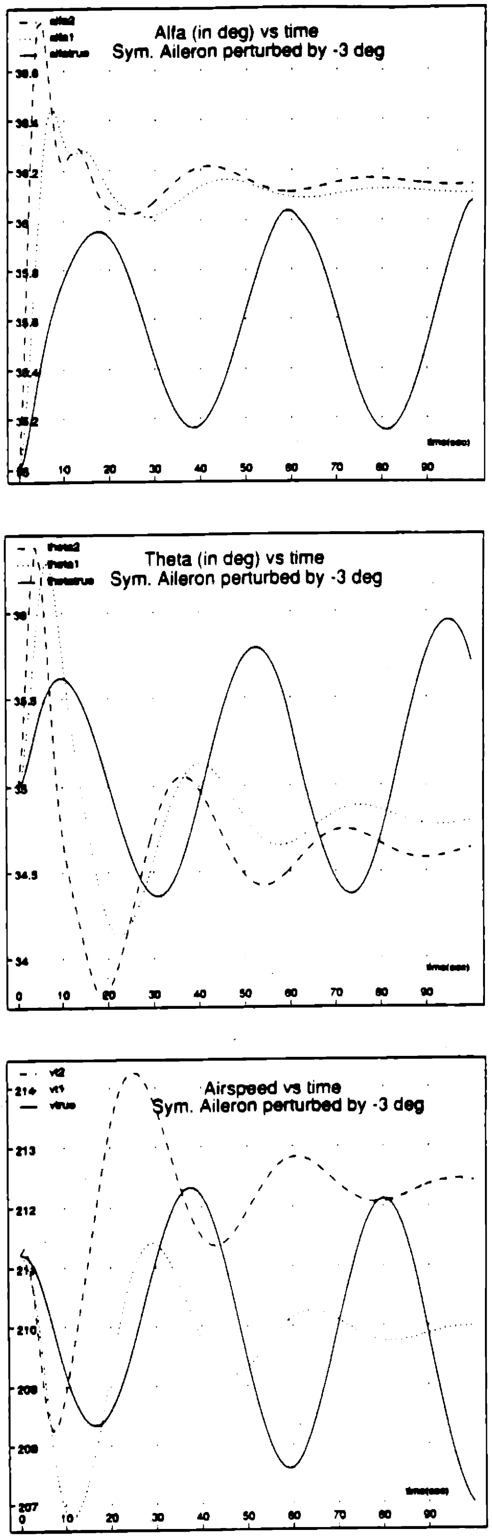

Figure B.8 Plots with Ail$_{sym}$ Perturbed by -3 deg from Trim

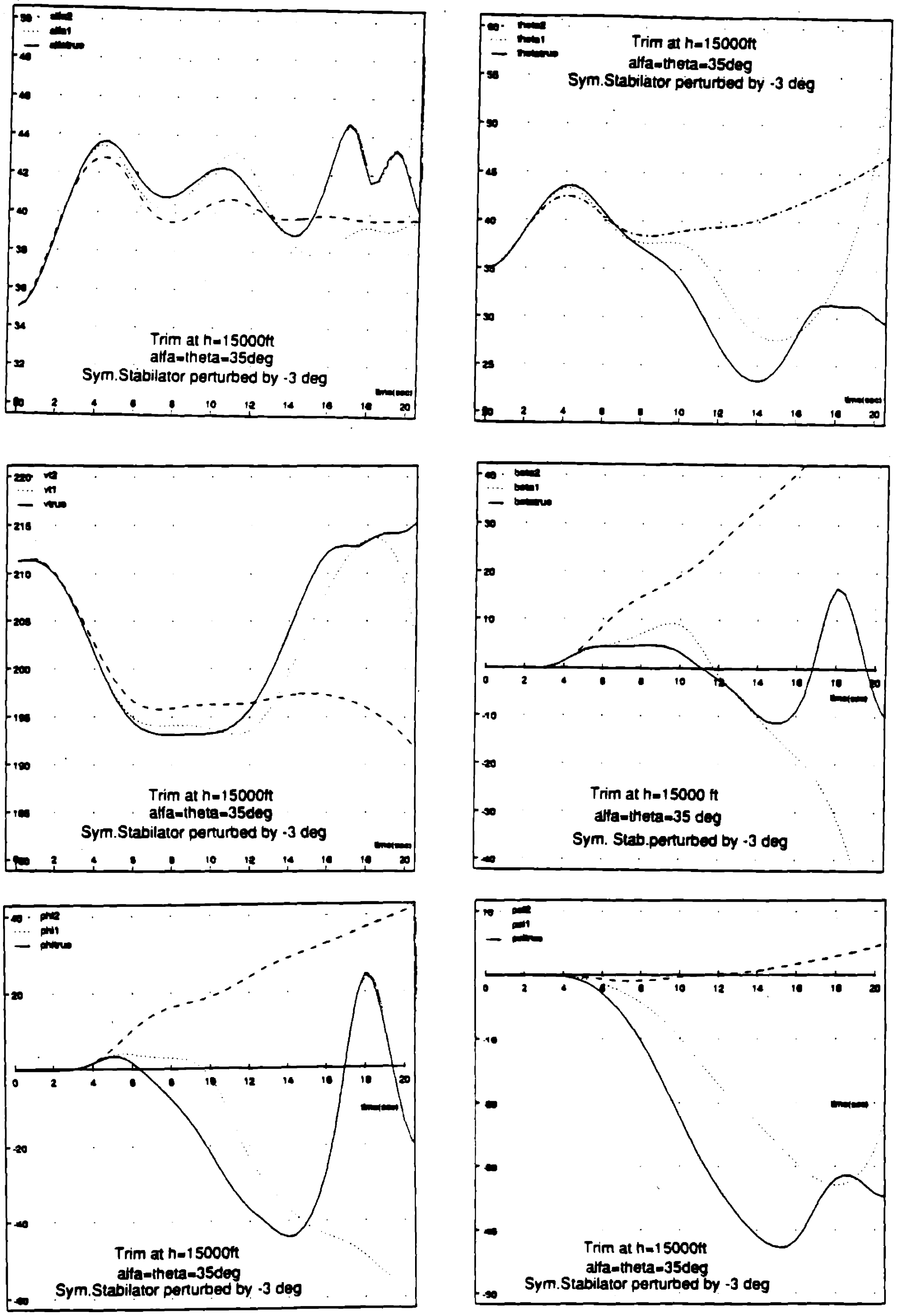

Figure B.9 Plots with Stab_{sym} Perturbed by -3 deg from Trim

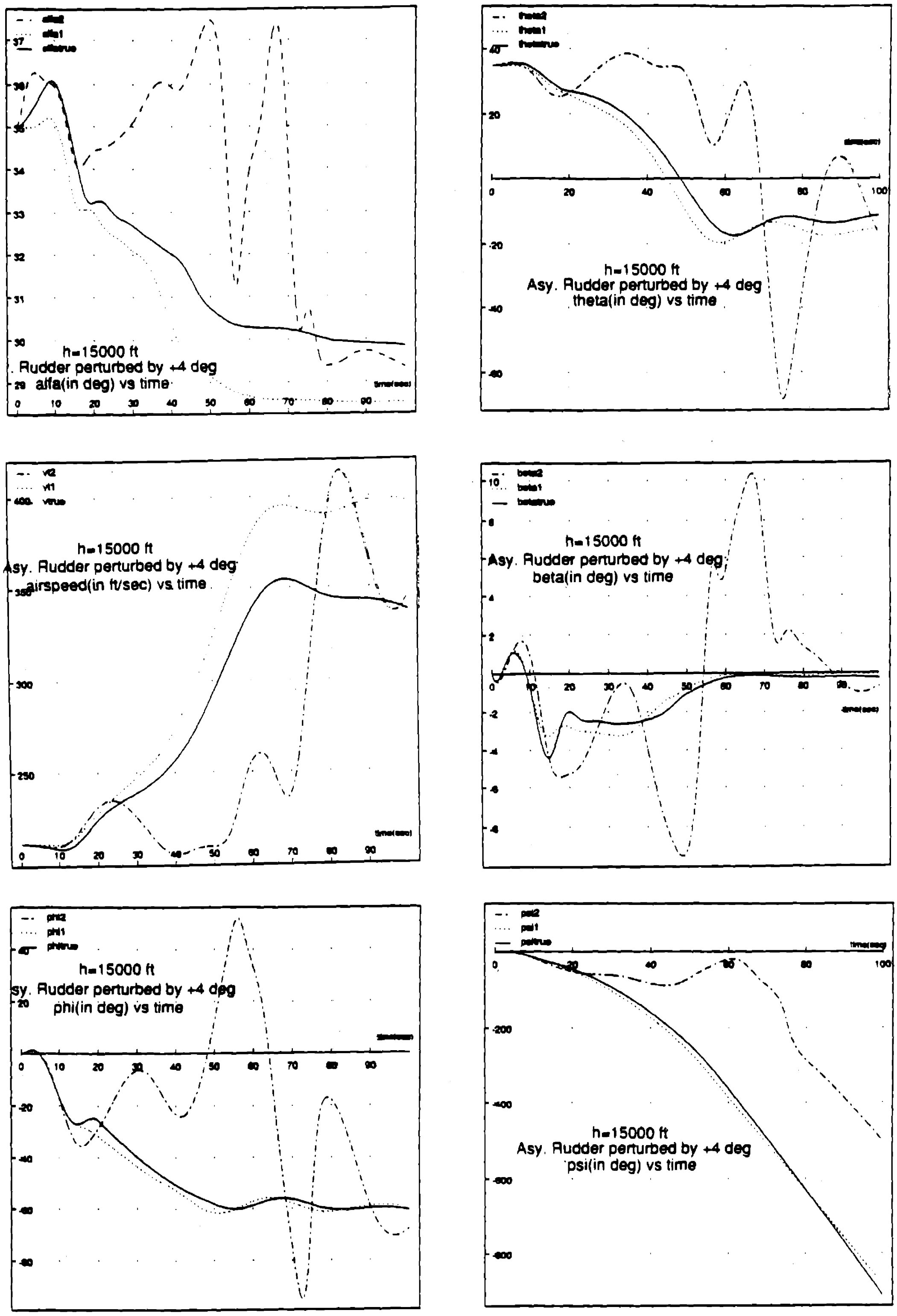

Figure B.10 Plots with Rud Perturbed by +4 deg from Trim

B.2 Time Simulations at Trim Point Number 2

The following figure shows the simulation results at the second trim point,

altitude = 5000 ft

$\alpha = \theta = 50^\circ$

$\beta = \phi = \psi = 0^\circ$

$P = Q = R = 0^\circ/\text{sec}$

(Note: This is a very hard trim point. It is highly unstable. No explicit perturbation is introduced to initiate the time simulation. The imprecise representation of the trim is enough to set the system adrift from the trim. Even the results from the "true" model do not stay at the equilibrium point because of the inevitable minor offsets of the controls from the exact trim settings.)

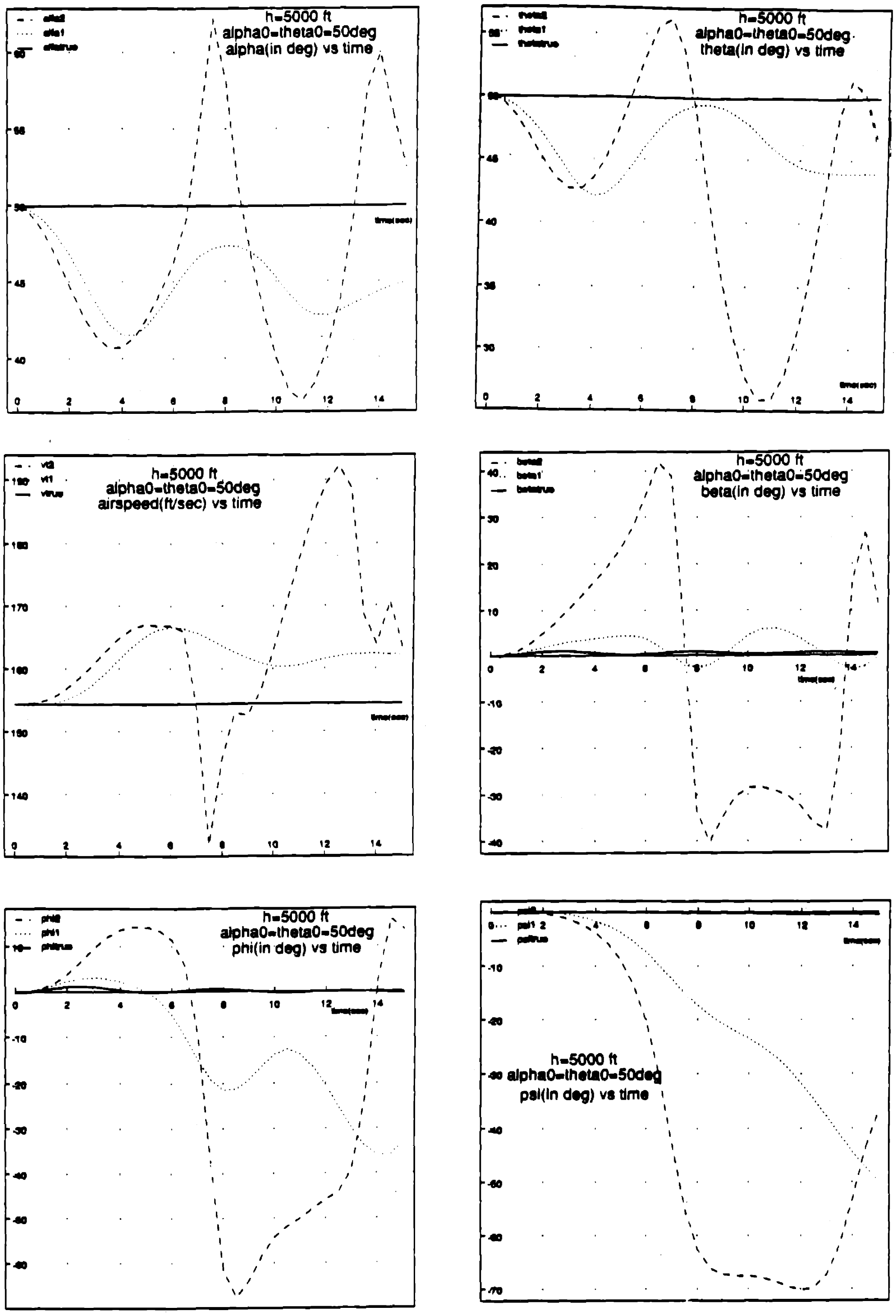

Figure B.13 Open-Loop Time Simulation Results at the Second Trim Point

APPENDIX C

THE INPUT-OUTPUT LINEARIZING CONTROLLER FOR THE HARV

C.1 Design model of the HARV for Input-Output Linearization

Plugging in the approximations of the aerodynamic coefficients through the stability derivatives (equations 2-35 to 2-40) and the expressions for the propulsive forces and moments (equations 2-41 to 2-49) into the state equations in Section 2.4 (equations 2-26 to 2-34), we obtain the design model in the form of

$$\dot{x} = f(x) + G(x)\,u \tag{C-1}$$

$$y = Cx \tag{C-2}$$

with x and u as defined in Section 3.3.2,

and $$f(x) = [f_1(x), \ldots, f_9(x)]^T \tag{C-3}$$

$$G(x) = [g_1^T(x), \ldots, g_{11}^T(x)]^T \tag{C-4}$$

The elements of the vector field f(x) are defined by

$$f_1(x) = \frac{1}{2}\frac{\rho V_t^2}{m} S(-C_{D0} - \frac{\partial C_D}{\partial Q} Q + \beta^2 \frac{\partial C_Y}{\partial \beta} + \beta \frac{\partial C_Y}{\partial P} P + \beta \frac{\partial C_Y}{\partial R} R\,)$$
$$+ g(\cos\theta \cos\phi \sin\alpha - \sin\theta \cos\alpha + \beta \cos\theta \sin\phi) \tag{C-5}$$

$$
\begin{aligned}
f_2(x) = {} & Q + \frac{g}{V_t}(\cos\theta \cos\phi \cos\alpha + \sin\alpha \sin\theta) - \beta(P\cos\alpha + R\sin\alpha) \\
& - \frac{1}{2}\frac{\rho V_t}{m} S\left(C_{L0} + \frac{\partial C_L}{\partial Q} Q\right)
\end{aligned}
\tag{C-6}
$$

$$
\begin{aligned}
f_3(x) = {} & P\sin\alpha - R\cos\alpha + \frac{g}{V_t}[\beta(\sin\theta\cos\alpha - \cos\theta\sin\alpha\cos\phi) + \sin\phi\cos\theta] \\
& + \frac{1}{2}\frac{\rho V_t}{m} S[\beta(C_{D0} + \frac{\partial C_D}{\partial Q} Q) + \frac{\partial C_Y}{\partial \beta}\beta + \frac{\partial C_Y}{\partial P} P + \frac{\partial C_Y}{\partial R} R]
\end{aligned}
\tag{C-7}
$$

$$
\begin{aligned}
f_4(x) = {} & \frac{A}{B} PQ + \frac{C}{B} QR \\
& + \frac{1}{2}\rho V_t^2 S\, b \frac{I_{zz}}{B}\left(C_{1asy} + \frac{\partial C_1}{\partial \beta}\beta + \frac{\partial C_1}{\partial P} P + \frac{\partial C_1}{\partial R} R\right) \\
& + \frac{1}{2}\rho V_t^2 S\, b \frac{I_{xz}}{B}\left(\frac{\partial C_N}{\partial \beta}\beta + \frac{\partial C_N}{\partial P} P + \frac{\partial C_N}{\partial R} R\right)
\end{aligned}
\tag{C-8}
$$

$$
f_5(x) = \frac{(I_{zz} - I_{xx})RP + I_{xz}(R^2 - P^2)}{I_{yy}} + \frac{1}{2}\frac{\rho V_t^2}{I_{yy}} S\, c\left(C_{M0} + \frac{\partial C_M}{\partial Q} Q\right)
\tag{C-9}
$$

$$
\begin{aligned}
f_6(x) = {} & \frac{D \cdot PQ + E \cdot QR}{B} \\
& + \frac{1}{2}\rho V_t^2 S\, b \frac{I_{xz}}{B}\left(C_{1asy} + \frac{\partial C_1}{\partial \beta}\beta + \frac{\partial C_1}{\partial P} P + \frac{\partial C_1}{\partial R} R\right) \\
& + \frac{1}{2}\rho V_t^2 S\, b \frac{I_{xx}}{B}\left(\frac{\partial C_N}{\partial \beta}\beta + \frac{\partial C_N}{\partial P} P + \frac{\partial C_N}{\partial R} R\right)
\end{aligned}
\tag{C-10}
$$

$$
f_7(x) = Q\cos\phi - R\sin\phi
\tag{C-11}
$$

$$
f_8(x) = P + Q\sin\phi\tan\theta + R\cos\phi\tan\theta
\tag{C-12}
$$

$$
f_9(x) = Q\sin\phi\sec\theta + R\cos\phi\sec\theta
\tag{C-13}
$$

The vector fields g_i making up the matrix G are as follows

$$g_1^T(x) = \begin{bmatrix} 0 \\ -\frac{1}{2}\frac{\rho V_t^2}{m} S \frac{\partial C_D}{\partial Stab_{sym}} \\ \frac{1}{2}\frac{\rho V_t^2}{m} S\, \beta \frac{\partial C_Y}{\partial Ail_{asy}} \\ \frac{1}{2}\frac{\rho V_t^2}{m} S\, \beta \frac{\partial C_Y}{\partial Rud} \\ \frac{1}{2}\frac{\rho V_t^2}{m} S\, \beta \frac{\partial C_Y}{\partial Stab_{asy}} \\ \frac{2 \cos \alpha}{m} \\ 0 \\ \frac{\beta}{m} \\ \frac{\beta}{m} \\ \frac{\sin \alpha}{m} \\ \frac{\sin \alpha}{m} \end{bmatrix} \qquad \text{(C-14)}$$

$$g_2^T(x) = \begin{bmatrix} -\frac{1}{2}\frac{\rho V_t}{m} S \frac{\partial C_L}{\partial Ail_{sym}} \\ -\frac{1}{2}\frac{\rho V_t}{m} S \frac{\partial C_L}{\partial Stab_{sym}} \\ 0 \\ 0 \\ 0 \\ \frac{-2 \sin \alpha}{V_t m} \\ 0 \\ 0 \\ 0 \\ \frac{\cos \alpha}{V_t m} \\ \frac{\cos \alpha}{V_t m} \end{bmatrix} \qquad \text{(C-15)}$$

$$g_3^T(x) = \begin{bmatrix} 0 \\ \frac{1}{2}\frac{\rho V_t}{m} S\,\beta \frac{\partial C_D}{\partial Stab_{sym}} \\ \frac{1}{2}\frac{\rho V_t}{m} S \frac{\partial C_Y}{\partial Ail_{asy}} \\ \frac{1}{2}\frac{\rho V_t}{m} S \frac{\partial C_Y}{\partial Rud} \\ \frac{1}{2}\frac{\rho V_t}{m} S \frac{\partial C_Y}{\partial Stab_{asy}} \\ \frac{-2\beta \cos\alpha}{V_t m} \\ 0 \\ \frac{1}{V_t m} \\ \frac{1}{V_t m} \\ \frac{-\beta \sin\alpha}{V_t m} \\ \frac{-\beta \sin\alpha}{V_t m} \end{bmatrix} \tag{C-16}$$

$$g_4^T(x) = \begin{bmatrix} 0 \\ 0 \\ \frac{1}{2}\frac{\rho V_t^2}{B} S\, b(I_{zz} \frac{\partial C_1}{\partial Ail_{asy}} + I_{xz} \frac{\partial C_N}{\partial Ail_{asy}}) \\ \frac{1}{2}\frac{\rho V_t^2}{B} S\, b(I_{zz} \frac{\partial C_1}{\partial Rud} + I_{xz} \frac{\partial C_N}{\partial Rud}) \\ \frac{1}{2}\frac{\rho V_t^2}{B} S\, b(I_{zz} \frac{\partial C_1}{\partial Stab_{asy}} + I_{xz} \frac{\partial C_N}{\partial Stab_{asy}}) \\ 0 \\ \frac{-2y_0 I_{xz}}{B} \\ \frac{-(z_0 I_{zz} + x_0 I_{xz})}{B} \\ \frac{-(z_0 I_{zz} + x_0 I_{xz})}{B} \\ \frac{-y_0 I_{zz}}{B} \\ \frac{y_0 I_{zz}}{B} \end{bmatrix} \tag{C-17}$$

$$g_5^T(x) = \begin{bmatrix} \frac{1}{2}\frac{\rho V_t^2}{I_{yy}} S\, c \frac{\partial C_M}{\partial Ail_{sym}} \\ \frac{1}{2}\frac{\rho V_t^2}{I_{yy}} S\, c \frac{\partial C_M}{\partial Stab_{sym}} \\ 0 \\ 0 \\ 0 \\ \frac{2z_0}{I_{yy}} \\ 0 \\ 0 \\ 0 \\ \frac{x_0}{I_{yy}} \\ \frac{x_0}{I_{yy}} \end{bmatrix} \qquad \text{(C-18)}$$

$$g_6^T(x) = \begin{bmatrix} 0 \\ 0 \\ \frac{1}{2}\frac{\rho V_t^2}{B} S\, b(I_{xz}\frac{\partial C_l}{\partial Ail_{asy}} + I_{xx}\frac{\partial C_N}{\partial Ail_{asy}}) \\ \frac{1}{2}\frac{\rho V_t^2}{B} S\, b(I_{xz}\frac{\partial C_l}{\partial Rud} + I_{xx}\frac{\partial C_N}{\partial Rud}) \\ \frac{1}{2}\frac{\rho V_t^2}{B} S\, b(I_{xz}\frac{\partial C_l}{\partial Stab_{asy}} + I_{xx}\frac{\partial C_N}{\partial Stab_{asy}}) \\ 0 \\ \frac{-2y_0 I_{xx}}{B} \\ \frac{-(z_0 I_{xz} + x_0 I_{xx})}{B} \\ \frac{-(z_0 I_{xz} + x_0 I_{xx})}{B} \\ \frac{-y_0 I_{xz}}{B} \\ \frac{y_0 I_{xz}}{B} \end{bmatrix} \qquad \text{(C-19)}$$

$$g_7(x) = g_8(x) = g_9(x) = [0\ 0\ 0\ 0\ 0\ 0\ 0\ 0\ 0\ 0\ 0] \qquad \text{(C-20)}$$

The outputs are given by $y = Cx$, with

$$C = \begin{bmatrix} 1&0&0&0&0&0&0&0&0 \\ 0&1&0&0&0&0&0&0&0 \\ 0&0&1&0&0&0&0&0&0 \\ 0&0&0&0&0&0&1&0&0 \\ 0&0&0&0&0&0&0&1&0 \\ 0&0&0&0&0&0&0&0&1 \end{bmatrix} \qquad \text{(C-21)}$$

C.2 Derivation of the Linearizing Control

Starting from the design model in the previous section, we repeatedly differentiate the outputs (w.r.t. time) until the inputs appear. V_t, α, and β only have to be differentiated once while θ, ϕ, and ψ have to be differentiated twice. Collecting these time derivatives into the vector

$$w = \left[\dot{V}_t,\ \dot{\alpha},\ \dot{\beta},\ \ddot{\theta},\ \ddot{\phi},\ \ddot{\psi}\right]^T \qquad \text{(C-22)}$$

we get

$$w = a(x) + B(x)\,u \qquad \text{(C-23)}$$

with $a(x) = [a_1(x), \ldots, a_6(x)]^T$ (C-24)

and $B(x) = [b_1^T(x), \ldots, b_6^T(x)]^T$ (C-25)

The components of the vector field a are given by

$$a_1(x) = \frac{1}{2}\frac{\rho V_t^2}{m} S(-C_{D0} - \frac{\partial C_D}{\partial Q} Q + \beta^2 \frac{\partial C_Y}{\partial \beta} + \beta \frac{\partial C_Y}{\partial P} P + \beta \frac{\partial C_Y}{\partial R} R\,)$$
$$+\ g(\cos\theta\cos\phi\sin\alpha - \sin\theta\cos\alpha + \beta\cos\theta\sin\phi) \qquad \text{(C-26)}$$

$$a_2(x) = Q + \frac{g}{V_t}(\cos\theta\cos\phi\cos\alpha + \sin\alpha\sin\theta) - \beta(P\cos\alpha + R\sin\alpha)$$
$$-\ \frac{1}{2}\frac{\rho V_t}{m} S(C_{L0} + \frac{\partial C_L}{\partial Q} Q) \qquad \text{(C-27)}$$

$$a_3(x) = P\sin\alpha - R\cos\alpha + \frac{g}{V_t}\,[\beta(\sin\theta\cos\alpha - \cos\theta\sin\alpha\cos\phi) + \sin\phi\cos\theta]$$
$$+\ \frac{1}{2}\frac{\rho V_t}{m} S[\beta(C_{D0} + \frac{\partial C_D}{\partial Q}\,Q) + \frac{\partial C_Y}{\partial \beta}\,\beta + \frac{\partial C_Y}{\partial P}\,P + \frac{\partial C_Y}{\partial R} R] \qquad \text{(C-28)}$$

$$a_4(x) = \frac{(I_{zz} - I_{xx})RP + I_{xz}(R^2 - P^2)}{I_{yy}} \cos\phi - \frac{D{\cdot}PQ + E{\cdot}QR}{B} \sin\phi$$
$$- (Q \sin\phi + R \cos\phi)(P + Q \sin\phi \tan\theta + R \cos\phi \tan\theta)$$
$$+ \frac{1}{2} \rho V_t^2 S\, c \frac{\cos\phi}{I_{yy}} (C_{M0} + \frac{\partial C_M}{\partial Q} Q)$$
$$- \frac{1}{2} \rho V_t^2 S\, b \frac{I_{xz}}{B} \sin\phi\, (C_{l\,asy} + \frac{\partial C_l}{\partial \beta} \beta + \frac{\partial C_l}{\partial P} P + \frac{\partial C_l}{\partial R} R)$$
$$- \frac{1}{2} \rho V_t^2 S\, b \frac{I_{xx}}{B} \sin\phi\, (\frac{\partial C_N}{\partial \beta} \beta + \frac{\partial C_N}{\partial P} P + \frac{\partial C_N}{\partial R} R) \qquad \text{(C-29)}$$

$$a_5(x) = \frac{(I_{zz} - I_{xx})RP + I_{xz}(R^2 - P^2)}{I_{yy}} \sin\phi \tan\theta + \frac{A{\cdot}PQ + C{\cdot}QR}{B}$$
$$+ \frac{D{\cdot}PQ + E{\cdot}QR}{B} \cos\phi \tan\theta + PQ \cos\phi \tan\theta - RP \sin\phi \tan\theta$$
$$+ (Q \cos\phi - R \sin\phi)(Q \sin\phi + R \cos\phi)(\tan^2\theta + \sec^2\theta)$$
$$+ \frac{1}{2} \frac{\rho V_t^2}{I_{yy}} S\, c \sin\phi \tan\theta (C_{M0} + \frac{\partial C_M}{\partial Q} Q)$$
$$+ \frac{1}{2} \rho V_t^2 S\, b \frac{I_{zz} + I_{xz} \cos\phi \tan\theta}{B} (C_{l\,asy} + \frac{\partial C_l}{\partial \beta} \beta + \frac{\partial C_l}{\partial P} P + \frac{\partial C_l}{\partial R} R)$$
$$+ \frac{1}{2} \rho V_t^2 S\, b \frac{I_{xz} + I_{xx} \cos\phi \tan\theta}{B} (\frac{\partial C_N}{\partial \beta} \beta + \frac{\partial C_N}{\partial P} P + \frac{\partial C_N}{\partial R} R) \qquad \text{(C-30)}$$

$$a_6(x) = \frac{(I_{zz} - I_{xx})RP + I_{xz}(R^2 - P^2)}{I_{yy}} \sin\phi \sec\theta + \frac{D{\cdot}PQ + E{\cdot}QR}{B} \cos\phi \sec\theta$$
$$+ PQ \cos\phi \sec\theta - RP \sin\phi \sec\theta$$
$$+ 2(Q \cos\phi - R \sin\phi)(Q \sin\phi + R \cos\phi) \sec\theta \tan\theta$$
$$+ \frac{1}{2} \frac{\rho V_t^2}{I_{yy}} S\, c \sin\phi \sec\theta (C_{M0} + \frac{\partial C_M}{\partial Q} Q)$$
$$+ \frac{1}{2} \rho V_t^2 S\, b \frac{I_{xz} \cos\phi \sec\theta}{B} (C_{l\,asy} + \frac{\partial C_l}{\partial \beta} \beta + \frac{\partial C_l}{\partial P} P + \frac{\partial C_l}{\partial R} R)$$
$$+ \frac{1}{2} \rho V_t^2 S\, b \frac{I_{xx} \cos\phi \sec\theta}{B} (\frac{\partial C_N}{\partial \beta} \beta + \frac{\partial C_N}{\partial P} P + \frac{\partial C_N}{\partial R} R) \qquad \text{(C-31)}$$

The rows of the B matrix are given by

$$b_1(x) = g_1(x),\ b_2(x) = g_2(x),\ b_3(x) = g_3(x) \qquad \text{(C-32)}$$

(the g's are defined in Section C.1)

$$b_4^T(x) = \begin{bmatrix} \frac{1}{2}\frac{\rho V_t^2}{I_{yy}} S\, c \frac{\partial C_M}{\partial Ail_{sym}} \\ \frac{1}{2}\frac{\rho V_t^2}{I_{yy}} S\, c \frac{\partial C_M}{\partial Stab_{sym}} \\ -\frac{1}{2}\frac{\rho V_t^2}{B} S\, b \sin\phi\, (I_{xz}\frac{\partial C_l}{\partial Ail_{asy}} + I_{xx}\frac{\partial C_N}{\partial Ail_{asy}}) \\ -\frac{1}{2}\frac{\rho V_t^2}{B} S\, b \sin\phi\, (I_{xz}\frac{\partial C_l}{\partial Rud} + I_{xx}\frac{\partial C_N}{\partial Rud}) \\ -\frac{1}{2}\frac{\rho V_t^2}{B} S\, b \sin\phi\, (I_{xz}\frac{\partial C_l}{\partial Stab_{asy}} + I_{xx}\frac{\partial C_N}{\partial Stab_{asy}}) \\ \frac{2 z_0 \cos\phi}{I_{yy}} \\ \frac{y_0 I_{xx} \sin\phi}{B} \\ \frac{(z_0 I_{xz} - x_0 I_{xx}) \sin\phi}{B} \\ \frac{(z_0 I_{xz} - x_0 I_{xx}) \sin\phi}{B} \\ \frac{x_0 \cos\phi}{I_{yy}} + \frac{y_0 I_{xz} \sin\phi}{2B} \\ \frac{x_0 \cos\phi}{I_{yy}} - \frac{y_0 I_{xz} \sin\phi}{2B} \end{bmatrix} \qquad \text{(C-33)}$$

$$b_5^T(x) = \begin{bmatrix} \frac{1}{2}\frac{\rho V_t^2}{I_{yy}} S\, c \sin\phi \tan\theta \frac{\partial C_M}{\partial Ail_{sym}} \\ \frac{1}{2}\frac{\rho V_t^2}{I_{yy}} S\, c \sin\phi \tan\theta \frac{\partial C_M}{\partial Stab_{sym}} \\ \frac{1}{2}\frac{\rho V_t^2}{B} S\, b[(I_{zz} + I_{xz}\cos\phi \tan\theta)\frac{\partial C_1}{\partial Ail_{asy}} + (I_{xz} + I_{xx}\cos\phi \tan\theta)\frac{\partial C_N}{\partial Ail_{asy}}] \\ \frac{1}{2}\frac{\rho V_t^2}{B} S\, b[(I_{zz} + I_{xz}\cos\phi \tan\theta)\frac{\partial C_1}{\partial Rud} + (I_{xz} + I_{xx}\cos\phi \tan\theta)\frac{\partial C_N}{\partial Rud}] \\ \frac{1}{2}\frac{\rho V_t^2}{B} S\, b[(I_{zz} + I_{xz}\cos\phi \tan\theta)\frac{\partial C_1}{\partial Stab_{asy}} + (I_{xz} + I_{xx}\cos\phi \tan\theta)\frac{\partial C_N}{\partial Stab_{asy}}] \\ \frac{2z_0 \sin\phi \tan\theta}{I_{yy}} \\ \frac{-y_0(I_{xz} + I_{xx}\cos\phi \tan\theta)}{B} \\ \frac{-[z_0(I_{zz} + I_{xz}\cos\phi \tan\theta) + x_0(I_{xz} + I_{xx}\cos\phi \tan\theta)]}{B} \\ \frac{-[z_0(I_{zz} + I_{xz}\cos\phi \tan\theta) + x_0(I_{xz} + I_{xx}\cos\phi \tan\theta)]}{B} \\ \frac{x_0 \sin\phi \tan\theta}{I_{yy}} - \frac{y_0(I_{zz} + I_{xz}\cos\phi \tan\theta)}{2B} \\ \frac{x_0 \sin\phi \tan\theta}{I_{yy}} + \frac{y_0(I_{zz} + I_{xz}\cos\phi \tan\theta)}{2B} \end{bmatrix} \tag{C-34}$$

$$b_6^T(x) = \begin{bmatrix} \frac{1}{2}\frac{\rho V_t^2}{I_{yy}} S\, c \sin\phi \sec\theta \frac{\partial C_M}{\partial Ail_{sym}} \\ \frac{1}{2}\frac{\rho V_t^2}{I_{yy}} S\, c \sin\phi \sec\theta \frac{\partial C_M}{\partial Stab_{sym}} \\ \frac{1}{2}\frac{\rho V_t^2}{B} S\, b \cos\phi \sec\theta (I_{xz}\frac{\partial C_1}{\partial Ail_{asy}} + I_{xx}\frac{\partial C_N}{\partial Ail_{asy}}) \\ \frac{1}{2}\frac{\rho V_t^2}{B} S\, b \cos\phi \sec\theta (I_{xz}\frac{\partial C_1}{\partial Rud} + I_{xx}\frac{\partial C_N}{\partial Rud}) \\ \frac{1}{2}\frac{\rho V_t^2}{B} S\, b \cos\phi \sec\theta (I_{xz}\frac{\partial C_1}{\partial Stab_{asy}} + I_{xx}\frac{\partial C_N}{\partial Stab_{asy}}) \\ \frac{2z_0 \sin\phi \sec\theta}{I_{yy}} \\ \frac{-y_0 I_{xx} \cos\phi \sec\theta}{B} \\ -\frac{(z_0 I_{xz} + x_0 I_{xx})\cos\phi \sec\theta}{B} \\ -\frac{(z_0 I_{xz} + x_0 I_{xx})\cos\phi \sec\theta}{B} \\ \frac{x_0 \sin\phi \sec\theta}{I_{yy}} - \frac{y_0 I_{xz} \cos\phi \sec\theta}{2B} \\ \frac{x_0 \sin\phi \sec\theta}{I_{yy}} + \frac{y_0 I_{xz} \cos\phi \sec\theta}{2B} \end{bmatrix} \qquad \text{(C-35)}$$

The linearizing control is chosen such that $a(x) + B(x)\, u = v$, as discussed in detail in Section 3.3.2.

C.3 Numerical Value of the Weighting Matrix W Used in the Input-Output Linearizing Controller

At a trim point setting of steady level flight with $h = 15000$ feet, $\alpha = \theta = 35°$, W is chosen to be a diagonal matrix with diagonal elements: $1/(25)^2$, $1/(14)^2$, $1/(25)^2$, $1/(30)^2$, $1/(14)^2$, $1/(9681)^2$, $1/(2000)^2$, $1/(4193)^2$, $1/(4193)^2$, $1/(4193)^2$, $1/(4193)^2$.

APPENDIX D

LINEAR MODEL FOR THE UNCOMPENSATED PLANT AND THE INNER-LOOP COMPENSATED PLANT

D.1 Linear Model for the Uncompensated Plant

A linear model for the uncompensated plant is obtained by perturbing the system from the following trim point:

$h = 15000$ ft,

$V_t = 211.231$ ft/sec,

$\alpha = \theta = 35^\circ$,

$\beta = \phi = 0^\circ$,

$P = Q = R = 0$ deg/sec,

Left Aileron = Right Aileron = 0°,

Left Stabilator = Right Stabilator = -9.70415°,

Left Rudder = Right Rudder = 0°,

Left Engine Throttle = Right Engine Throttle = 119.817°,

and Thrust Vectoring off ($\sigma = 0^\circ$).

The resulting linear model is as follows

$$\dot{x} = Ax + Bu \tag{D-1}$$

$$y = Cx \tag{D-2}$$

where the state vector is defined as

$$x = [V_t, \alpha, \beta, P, Q, R, \phi, \theta, \psi]^T, \tag{D-3}$$

while the control vector is

$$u = [DSL, DSR, DRL, DRR, DAL, DAR, DTVL, DTVR, CPL, CPR]^T \tag{D-4}$$

with DSL: perturbation of the left stabilator from the trim position (down as positive)

DSR: perturbation of the right stabilator from the trim position (down as positive)

DRL: perturbation of the left rudder from the trim position (in as positive)

DRR: perturbation of the right stabilator from the trim position (in as positive)

DAL: perturbation of the left aileron from the trim position (down as positive)

DAR: perturbation of the right aileron from the trim position (down as positive)

DTVL: perturbation of the thrust vectoring angle (σ) for the left engine (upward thrust as positive)

DTVR: perturbation of the thrust vectoring angle (σ) for the right engine (upward thrust as positive)

CPL: perturbation of the left engine throttle from the trim setting

CPR: perturbation of the right engine throttle from the trim setting

(note: no lateral thrust vectoring is considered, the thrust vectoring vanes only go up and down here, i.e. $\eta = 0°$)

and the output vector is defined by

$$y = [V_t, \alpha, \beta, \phi, \theta, \psi]^T \tag{D-5}$$

With angles in degree, airspeed in ft/sec, acceleration in ft/sec^2, angular speeds in deg/sec, angular accelerations in deg/sec^2, and control inputs in deg, the numerical values for the A and B matrices are

$$A = \begin{bmatrix} A_1 A_2 A_3 \\ A_4 A_5 A_6 \\ A_7 A_8 A_9 \end{bmatrix}, \; B = \begin{bmatrix} B_1 B_2 B_3 \\ B_4 B_5 B_6 \\ B_7 B_8 B_9 \end{bmatrix}$$

with

$$A_1 = \begin{bmatrix} \text{-1.2097e-01} & \text{-1.8338e-01} & \text{9.0612e-02} \\ \text{-5.9543e-02} & \text{-1.0007e-01} & \text{4.9565e-02} \\ 0 & 0 & \text{-9.24549e-01} \end{bmatrix},$$

$$A_2 = \begin{bmatrix} 0 & \text{-9.5064e-05} & 0 \\ 0 & \text{9.8425e-01} & 0 \\ \text{5.7342e-01} & 0 & \text{-8.2106e-01} \end{bmatrix},$$

$$A_3 = \begin{bmatrix} 0 & \text{-5.6151e-01} & 0 \\ 0 & \text{-5.6331e-08} & 0 \\ \text{1.2476e-01} & 0 & 0 \end{bmatrix},$$

$$A_4 = \begin{bmatrix} 0 & 0 & \text{-9.24549e-01} \\ \text{-1.0822e-02} & \text{-1.40304e-01} & \text{7.0281e-02} \\ 0 & 0 & \text{-4.0833e-02} \end{bmatrix},$$

$$A_5 = \begin{bmatrix} \text{-9.6166e-01} & 0 & \text{7.3812e-01} \\ 0 & \text{-3.5657e-01} & 0 \\ \text{2.2700e-02} & 0 & \text{-8.8919e-02} \end{bmatrix},$$

$$A_6 = \begin{bmatrix} 0 & 0 & 0 \\ 0 & \text{1.9867e-09} & 0 \\ 0 & 0 & 0 \end{bmatrix},$$

$$A_7 = 0_{3x3},$$

$$A_8 = \begin{bmatrix} 1 & 0 & \text{7.0021e-01} \\ 0 & 1 & 0 \\ 0 & 0 & \text{1.2208e+00} \end{bmatrix},$$

$$A_9 = 0_{3x3},$$

and

$$B_1 = \begin{bmatrix} \text{-7.3713e-02} & \text{-7.3713e-02} & \text{1.7614e-03} \\ \text{-2.2946e-02} & \text{-2.2946e-02} & \text{1.6273e-03} \\ \text{3.4418e-03} & \text{-3.4418e-03} & \text{-2.7075e-03} \end{bmatrix},$$

$$B_2 = \begin{bmatrix} 1.76143e\text{-}03 & 2.1826e\text{-}07 & 2.1826e\text{-}07 \\ 1.6273e\text{-}03 & -3.5507e\text{-}03 & -3.5507e\text{-}03 \\ 2.7075e\text{-}03 & 3.3207e\text{-}03 & -3.3207e\text{-}03 \end{bmatrix},$$

$$B_3 = \begin{bmatrix} -7.9038e\text{-}02 & -7.9038e\text{-}02 & 1.2560e\text{-}01 & 1.2560e\text{-}01 \\ -3.0502e\text{-}02 & -3.0502e\text{-}02 & -2.3766e\text{-}02 & -2.3766e\text{-}02 \\ 0 & 0 & -1.4378e\text{-}03 & 1.4378e\text{-}03 \end{bmatrix},$$

$$B_4 = \begin{bmatrix} 9.0742e\text{-}01 & -9.0742e\text{-}01 & -4.0002e\text{-}03 \\ -4.9460e\text{-}01 & -4.9460e\text{-}01 & 2.1631e\text{-}02 \\ -4.8481e\text{-}02 & 4.8481e\text{-}02 & 5.3668e\text{-}02 \end{bmatrix},$$

$$B_5 = \begin{bmatrix} 4.0002e\text{-}03 & 5.3193e\text{-}01 & -5.3193e\text{-}01 \\ 2.1631e\text{-}02 & -3.4621e\text{-}02 & -3.4621e\text{-}02 \\ -5.3668e\text{-}02 & -3.9160e\text{-}02 & 3.9160e\text{-}02 \end{bmatrix},$$

$$B_6 = \begin{bmatrix} 5.6101e\text{-}01 & -5.6101e\text{-}01 & -1.2357e\text{-}02 & 1.2357e\text{-}02 \\ -1.0456e\text{+}00 & -1.0456e\text{+}00 & 1.4967e\text{-}02 & 1.4967e\text{-}02 \\ -9.8077e\text{-}03 & 9.8077e\text{-}03 & 1.2036e\text{-}01 & -1.2036e\text{-}01 \end{bmatrix},$$

$$B_7 = B_8 = 0_{3x3},$$

$$B_9 = 0_{3x4}.$$

D.2 Linear Model for the Inner-Loop Compensated Plant

The linear model for the inner-loop compensated plant is obtained at the same trim point described in the previous section. It is of the form

$$\dot{z} = Az + Bv + d \tag{D-6}$$

$$y = Cz \tag{D-7}$$

where

$$z = [V_t, \alpha, \beta, \theta, \dot{\theta}, \phi, \dot{\phi}, \psi, \dot{\psi}]^T$$

$$y = [V_t, \alpha, \beta, \theta, \phi, \psi]^T$$

$$v = [v_1, v_2, v_3, v_4, v_5, v_6]^T$$

With angles in deg, airspeed in ft/sec, angular speeds in deg/sec, v_1 in ft/sec^2, v_2 and v_3 in deg/sec, v_4, v_5 and v_6 in deg/sec^2, the numerical values for A, B, d, and C are as follows

$$A = \begin{bmatrix} A_1 A_2 A_3 \\ A_4 A_5 A_6 \\ A_7 A_8 A_9 \end{bmatrix}$$

with

$$A_1 = \begin{bmatrix} -3.4231\text{e-}02 & -4.0842\text{e-}02 & 9.0353\text{e-}02 \\ -9.0588\text{e-}04 & 5.6175\text{e-}03 & 4.7281\text{e-}02 \\ 0 & 0 & -4.3770\text{e-}02 \end{bmatrix},$$

$$A_2 = \begin{bmatrix} -2.7713\text{e-}02 & 1.9784\text{e-}01 & 0 \\ 3.3677\text{e-}03 & -2.9337\text{e-}02 & 0 \\ 0 & 0 & 1.0075\text{e-}01 \end{bmatrix},$$

$$A_3 = \begin{bmatrix} 0 & 0 & 0 \\ 0 & 0 & 0 \\ 4.7027\text{e-}01 & 0 & -8.1867\text{e-}01 \end{bmatrix},$$

$$A_4 = \begin{bmatrix} 0 & 0 & 0 \\ -7.7361\text{e-}03 & 8.3525\text{e-}02 & 6.4617\text{e-}02 \\ 0 & 0 & 0 \end{bmatrix},$$

$$A_5 = \begin{bmatrix} 0 & 1 & 0 \\ 5.2473\text{e-}02 & -4.2637\text{e-}01 & 0 \\ 0 & 0 & 0 \end{bmatrix},$$

$$A_6 = \begin{bmatrix} 0 & 0 & 0 \\ 0 & 0 & 0 \\ 1 & 0 & 0 \end{bmatrix},$$

$$A_7 = \begin{bmatrix} 0 & 0 & 9.6184\text{e-}01 \\ 0 & 0 & 0 \\ 0 & 0 & 1.7865\text{e+}00 \end{bmatrix},$$

$$A_8 = \begin{bmatrix} 0 & 0 & -1.2282\text{e+}00 \\ 0 & 0 & 0 \\ 0 & 0 & -2.4127\text{e+}00 \end{bmatrix},$$

$$A_9 = \begin{bmatrix} -6.3713e{+}00 & 0 & 1.0696e{+}01 \\ 0 & 0 & 1 \\ -1.1114e{+}01 & 0 & 1.9545e{+}01 \end{bmatrix},$$

while

$$\mathbf{B} = \begin{bmatrix} \mathbf{B}_1\mathbf{B}_2 \\ \mathbf{B}_3\mathbf{B}_4 \\ \mathbf{B}_5\mathbf{B}_6 \end{bmatrix}$$

with

$$\mathbf{B}_1 = \begin{bmatrix} 7.7137e{-}01 & -1.3908e{+}00 & 5.1369e{-}02 \\ -2.9016e{-}03 & 1.2559e{-}01 & -3.2262e{-}02 \\ -2.1734e{-}03 & -7.0980e{-}03 & 1.0194e{-}01 \end{bmatrix},$$

$$\mathbf{B}_2 = \begin{bmatrix} 1.5463e{-}04 & -9.2778e{-}05 & -4.1537e{-}05 \\ -3.1183e{-}05 & 7.6439e{-}04 & 9.4054e{-}03 \\ 5.2602e{-}04 & 1.3710e{-}03 & -2.6591e{-}02 \end{bmatrix},$$

$$\mathbf{B}_3 = \begin{bmatrix} 0 & 0 & 0 \\ -3.0074e{-}01 & -1.0447e{+}01 & -4.1587e{-}01 \\ 0 & 0 & 0 \end{bmatrix},$$

$$\mathbf{B}_4 = \begin{bmatrix} 0 & 0 & 0 \\ 8.1913e{-}01 & 9.9158e{-}03 & 4.4186e{-}02 \\ 0 & 0 & 0 \end{bmatrix},$$

$$\mathbf{B}_5 = \begin{bmatrix} 1.9047e{-}01 & -3.7845e{-}01 & 9.2085e{-}01 \\ 0 & 0 & 0 \\ -3.0405e{-}03 & 9.3192e{-}01 & -6.4013e{-}01 \end{bmatrix},$$

$$\mathbf{B}_6 = \begin{bmatrix} -5.5213e{-}02 & 9.8368e{-}01 & 3.2940e{-}01 \\ 0 & 0 & 0 \\ 2.1088e{-}02 & -3.3543e{-}02 & 1.6430e{+}00 \end{bmatrix},$$

and

$$\mathbf{d} = [-3.0430e{-}06, -1.7059e{-}03, 0, 0, -1.7309e{-}02, 0, 0, 0, 0]^T,$$

$$\mathbf{C} = \begin{bmatrix} 1&0&0&0&0&0&0&0&0 \\ 0&1&0&0&0&0&0&0&0 \\ 0&0&1&0&0&0&0&0&0 \\ 0&0&0&1&0&0&0&0&0 \\ 0&0&0&0&0&1&0&0&0 \\ 0&0&0&0&0&0&0&1&0 \end{bmatrix}$$

APPENDIX E

PLOTS OF AERODYNAMIC COEFFICIENTS VS. CONTROL SURFACE DEFLECTIONS

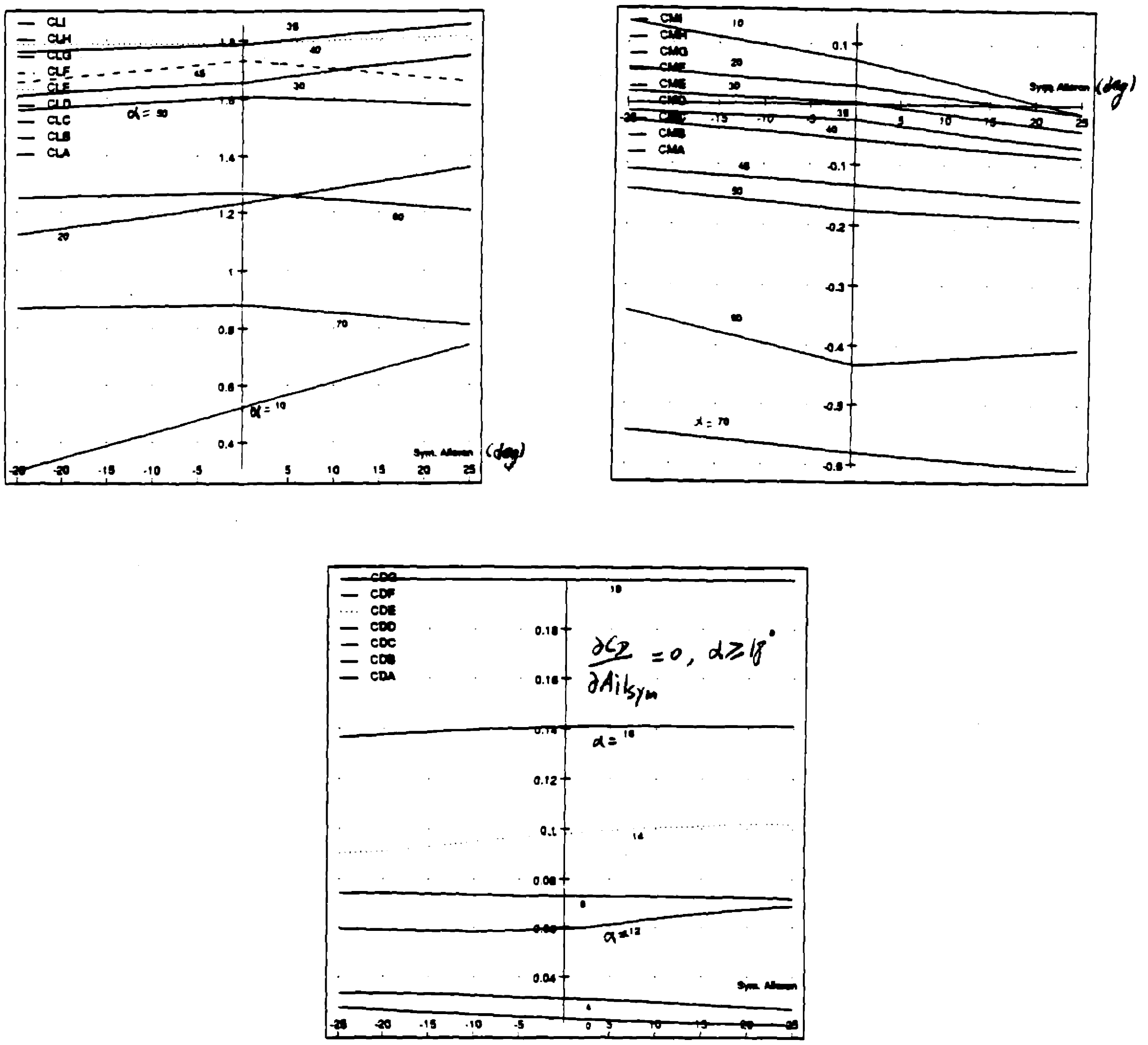

Figure E.1 C_L, C_M, and C_D vs. Ail_{sym}

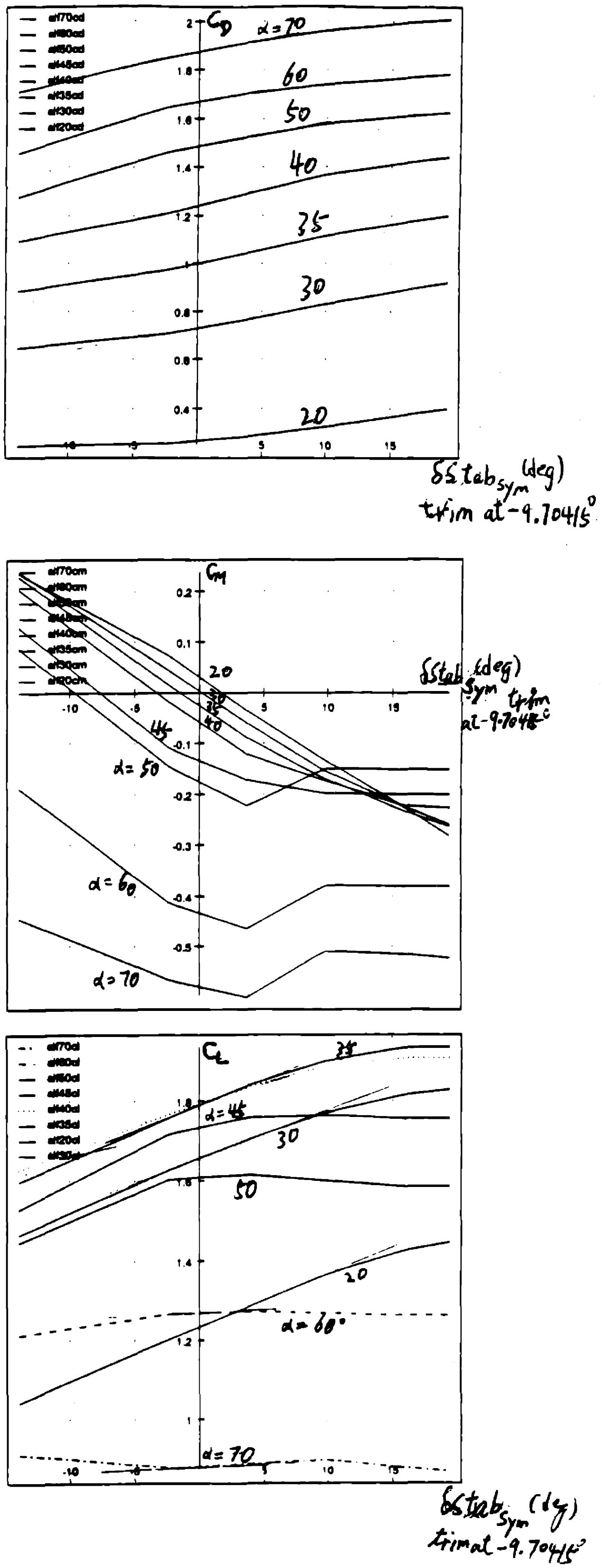

Figure E.2 C_L, C_M, and C_D vs. Stab$_{sym}$

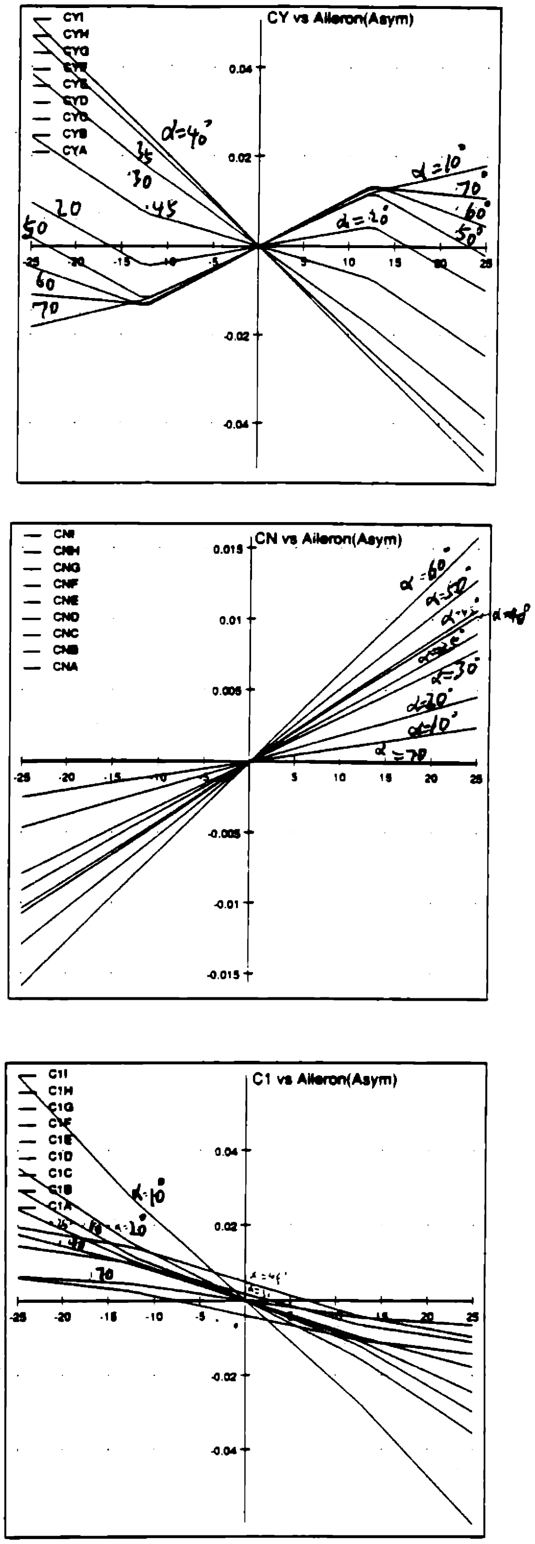

Figure E.3 C_Y, C_N, and C_1 vs.Ail_{asy}

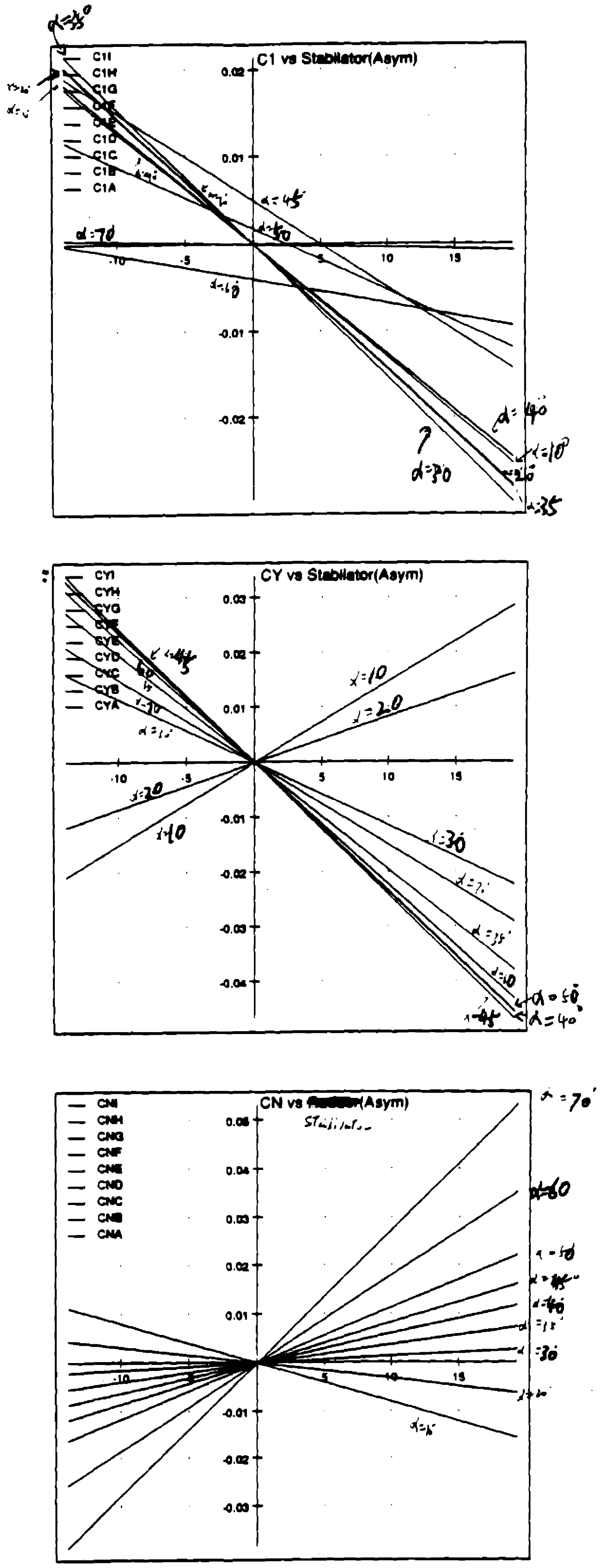

Figure E.4 C_Y, C_N, and C_1 vs. $Stab_{asy}$

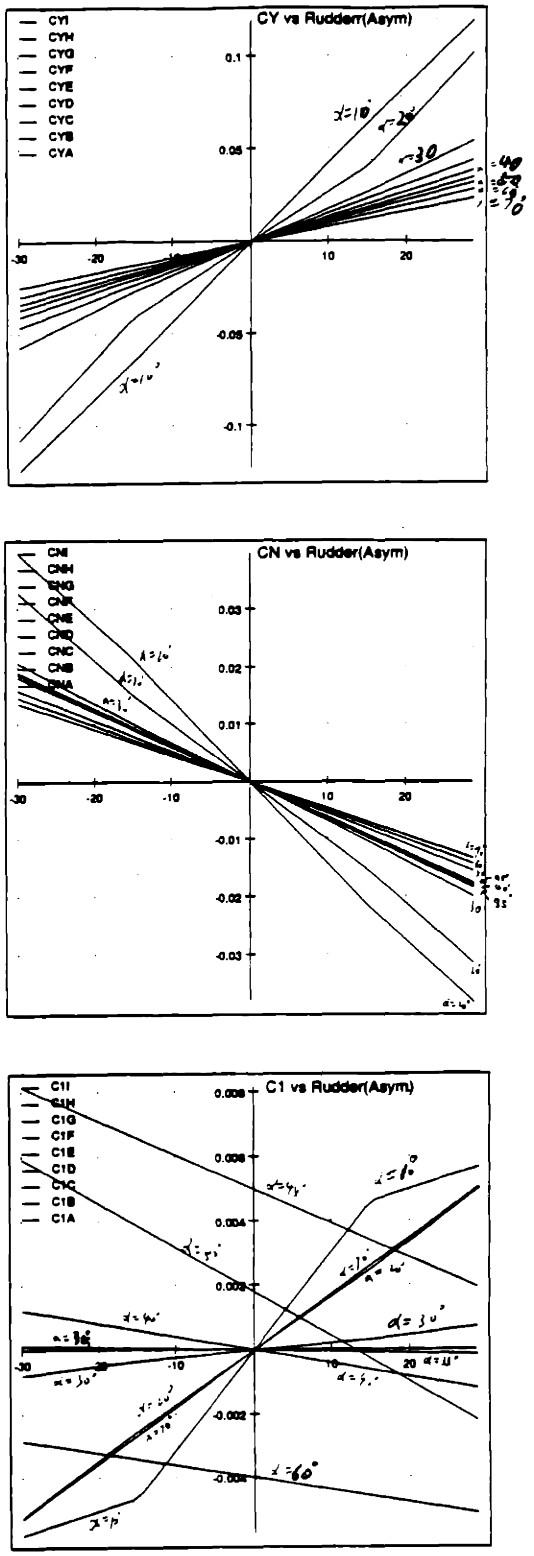

Figure E.5 C_Y, C_N, and C_1 vs. Rud

APPENDIX F

NUMERICAL VALUES FOR THE PARMERTERS OF THE LQG/LTR CONTROLLER DESIGNS IN CHAPTER 4

F.1 Numerical Values for the Parameters of the LQG/LTR Compensator Based on the Trim Point Linear Model

The state-space description of the LQG/LTR controller is given by

$$\dot{z} = (A_a - B_a G - HC_a)z - He \qquad \text{(F-1)}$$

$$\dot{v} = -Gz \qquad \text{(F-2)}$$

$$u = Tv \qquad \text{(F-3)}$$

where v is the pseudo-control and u is the physical control,

T is the distribution matrix given by equation 4-6 in Chapter 4,

e is the error signal given by the difference between the command signal r and the outputs y, $e = r - y$ (F-4)

The numerical values of the matrices $A_c = A_a - B_a G - HC_a$, H, and G are as follows.

```
H =
   1.5034e+00   3.0666e-01  -3.6245e-02   1.2200e-14   1.0718e+00   7.6252e-15
   7.1290e-01   2.0460e-01  -1.9826e-02  -1.4541e-15  -2.2286e-02   6.7614e-16
   8.1971e-16   6.6582e-15   2.3059e-02  -2.4953e-01   4.1784e-15   1.0299e-08
  -3.7530e-16  -1.6053e-14   3.6982e-01   1.7454e-13  -1.1665e-14  -1.1890e-08
   1.2865e-01   2.8095e-01  -2.8112e-02  -2.8969e-15   1.1071e-02   1.7837e-15
   1.4167e-17  -3.2733e-16   1.6333e-02  -1.6939e-16  -3.3439e-16   8.8293e-10
   1.2026e+01  -3.0051e-02   2.1002e-14   4.8356e-15  -2.5615e-02   3.2284e-15
  -5.0085e-03   2.0059e+00  -1.2879e-15  -6.3921e-15   3.7743e-03   3.6266e-16
   6.8836e-16  -2.8024e-16   4.0000e-01   1.8756e-14  -9.8898e-16   7.0066e-15
   1.0557e-15  -1.4823e-14  -4.0146e-14   1.9680e-13  -1.1818e-14  -5.8984e-09
  -7.6231e-03   6.3732e-03  -2.5569e-15  -1.0747e-14   3.0444e-02   9.8169e-16
   5.9598e-16  -1.3428e-16   3.3277e-14   1.6765e-14  -1.4608e-16   8.4238e-09
   1.0665e-15  -6.2280e-15   9.4747e-14   2.0000e+00  -5.5918e-15   1.5753e-14
  -4.2692e-03   3.7743e-03  -5.1218e-15  -5.6227e-15   2.0152e+00   1.3182e-16
   3.2325e-16   1.4529e-16   1.8698e-14   8.6565e-15   1.7658e-16   1.0000e+00

G =
  Columns 1 through 6
   5.7614e+01  -7.7131e-02   2.9075e-03   1.0320e-04  -1.0285e-02   2.0279e-04
  -7.7131e-02   1.4132e+02   8.3516e-03   2.1111e-06   8.9558e-01   6.3072e-05
   2.9107e-03   8.3516e-03   3.1617e+02   5.5024e-01   1.2299e-03  -7.9901e-01
   1.6593e-06   1.8004e-06   5.5025e-01   4.1705e+01   8.8148e-07   2.2599e+00
   1.0286e-02   8.9559e-01   1.2271e-03   1.5352e-04   4.2749e+01   5.0572e-05
  -1.3934e-06  -1.6685e-06  -7.9898e-01   2.2599e+00  -7.9767e-07   5.8626e+01

  Columns 7 through 12
   1.6597e+03  -6.2137e+00   9.4450e-01   2.8802e-03  -8.0225e-01  -1.3176e-03
  -9.1393e+00   9.9857e+03   3.0111e+00   4.8918e-03   1.3608e+02  -5.5100e-03
   1.4152e-01   8.1040e-01   4.9981e+04   1.8017e+02   4.6307e-02  -2.5812e+02
   4.9130e-05   8.1232e-05   1.4938e+01   8.7236e+02   1.4919e-05   1.1736e+02
  -2.9912e-01   2.8768e+01   4.0168e-01   2.0793e-03   9.1413e+02  -1.6912e-03
  -4.5061e-05  -8.0906e-05  -4.0090e+01   1.0894e+02  -1.5453e-05   1.7214e+03

  Columns 13 through 15
   3.3076e-03  -3.3660e+01  -1.9349e-02
   2.5641e-03  -3.4811e+01   1.0775e-02
   3.0431e+01   5.2537e-01   1.8390e+01
   9.7830e+03   1.6232e-04  -4.1444e+03
  -2.3298e-03   9.9999e+03  -2.0327e-02
   2.0721e+03  -1.5556e-04   1.9566e+04
```

```
Ac =
 Columns 1 through 6
 -5.7614e+01   7.7131e-02  -2.9075e-03  -1.0320e-04   1.0285e-02  -2.0279e-04
  7.7131e-02  -1.4132e+02  -8.3516e-03  -2.1111e-06  -8.9558e-01  -6.3072e-05
 -2.9107e-03  -8.3516e-03  -3.1617e+02  -5.5024e-01  -1.2299e-03   7.9901e-01
 -1.6593e-06  -1.8004e-06  -5.5025e-01  -4.1705e+01  -8.8148e-07  -2.2599e+00
  1.0286e-02  -8.9559e-01  -1.2271e-03  -1.5352e-04  -4.2749e+01  -5.0572e-05
  1.3934e-06   1.6685e-06   7.9898e-01  -2.2599e+00   7.9767e-07  -5.8626e+01
  1.0000e+00   0            0            0            0            0
  0            1.0000e+00   0            0            0            0
  0            0            1.0000e+00   0            0            0
  0            0            0            1.0000e+00   0            0
  0            0            0            0            1.0000e+00   0
  0            0            0            0            0            1.0000e+00
  0            0            0            0            0            0
  0            0            0            0            0            0
  0            0            0            0            0            0

 Columns 7 through 12
 -1.6600e+03   5.9071e+00  -7.6328e-01  -2.8802e-03   8.0225e-01   1.3176e-03
  9.0205e+00  -9.9859e+03  -2.9120e+00  -4.8918e-03  -1.3608e+02   5.5100e-03
 -1.4152e-01  -8.1040e-01  -4.9981e+04  -1.8017e+02  -4.6307e-02   2.5812e+02
 -4.9130e-05  -8.1232e-05  -1.6787e+01  -8.7236e+02  -1.4919e-05  -1.1736e+02
  2.7768e-01  -2.9049e+01  -2.6111e-01  -2.0793e-03  -9.1413e+02   1.6912e-03
  4.5061e-05   8.0906e-05   4.0008e+01  -1.0894e+02   1.5453e-05  -1.7214e+03
 -2.1253e+00  -1.5333e-01   9.0612e-02   0           -9.5064e-05   0
 -5.8708e-02  -2.1060e+00   4.9565e-02   0            9.8425e-01   0
 -1.1473e-16   2.8024e-16  -2.0576e+00   5.7342e-01   0           -8.2106e-01
 -1.7595e-16   1.4823e-14  -9.2455e-01  -9.6166e-01   0            7.3813e-01
 -9.5518e-03  -1.4668e-01   7.0281e-02   0           -3.5657e-01   0
 -9.9329e-17   1.3428e-16  -4.0833e-02   2.2700e-02   0           -8.8918e-02
 -1.7775e-16   6.2280e-15  -4.7374e-13   1.0000e+00   0            7.0021e-01
  7.1153e-04  -3.7743e-03   2.5609e-14   0            1.0000e+00   0
 -5.3876e-17  -1.4529e-16  -9.3490e-14   0            0            1.2208e+00

 Columns 13 through 15
 -3.3076e-03   3.2588e+01   1.9349e-02
 -2.5641e-03   3.4833e+01  -1.0775e-02
 -3.0181e+01  -5.2537e-01  -1.8390e+01
 -9.7830e+03  -1.6232e-04   4.1444e+03
  2.3298e-03  -1.0000e+04   2.0327e-02
 -2.0721e+03   1.5556e-04  -1.9566e+04
 -4.8356e-15  -5.3590e-01  -6.4567e-15
  6.3921e-15  -3.7744e-03  -7.2532e-16
  1.2476e-01   9.8898e-16  -1.4013e-14
 -1.9680e-13   1.1818e-14   1.1797e-08
  1.0747e-14  -3.0444e-02  -1.9634e-15
 -1.6765e-14   1.4608e-16  -1.6848e-08
 -2.0000e+00   5.5918e-15  -3.1507e-14
  5.6227e-15  -2.0152e+00  -2.6365e-16
 -8.6565e-15  -1.7658e-16  -2.0000e+00
```

```
T =
 -5.8908e+00  -2.9522e+01   1.4823e+01   1.1916e-01   1.3052e+00   3.9840e-01
 -5.8908e+00  -2.9522e+01  -1.4823e+01  -1.1916e-01   1.3052e+00  -3.9840e-01
  1.5371e+00   9.9685e+00  -7.4365e+01   2.8716e-01  -4.1132e-01   1.9163e+00
  1.5371e+00   9.9685e+00   7.4365e+01  -2.8716e-01  -4.1132e-01  -1.9163e+00
 -1.9065e+00  -1.4689e+01   1.0162e+02   1.1280e-01   5.8111e-01   2.9451e+00
 -1.9065e+00  -1.4689e+01  -1.0162e+02  -1.1280e-01   5.8111e-01  -2.9451e+00
  2.9150e+00   1.4539e+01  -1.1948e+02   5.9371e-01  -1.1224e+00  -3.3319e+00
  2.9150e+00   1.4539e+01   1.1948e+02  -5.9371e-01  -1.1224e+00   3.3319e+00
  2.3365e+00  -8.3168e+00   6.2459e+01   5.0358e-03   6.5423e-02   4.1471e+00
  2.3365e+00   8.3168e+00  -6.2459e+01  -5.0358e-03   6.5423e-02  -4.1471e+00
```

F.2 Numerical Values for the parameter of the Outer-Loop LQG/LTR Compensator with Augmented Integrators

The state space description of the controller is given again by equations F-1 and F-2, with v being the output of the outer-loop controller. The numerical values of the matrices $A_c=A_a-B_aG-HC_a$, H, and G are as follows.

```
H =
 2.0000e-06  0           0           0           0           0
 0           2.0000e-06  0           0           0           0
 0           0           2.0000e-06  0           0           0
 0           0           0           2.0000e-06  0           0
 0           0           0           0           2.0000e-06  0
 0           0           0           0           0           2.0000e-06
 2.0000e+00  0           0           0           0           0
 0           2.0000e+00  0           0           0           0
 0           0           2.0000e+00  0           0           0
 0           0           0           2.0020e+00  0           0
 0           0           0           4.0010e-03  0           0
 0           0           0           0           2.0020e+00  0
 0           0           0           0           4.0010e-03  0
 0           0           0           0           0           2.0020e+00
 0           0           0           0           0           4.0010e-03
```

```
G =
 Columns 1 through 6
  1.4142e+02  0           0           0           0           0
  0           1.4142e+02  0           0           0           0
  0           0           1.4142e+02  0           0           0
  0           0           0           4.3089e+01  0           0
  0           0           0           0           4.3089e+01  0
  0           0           0           0           0           4.3089e+01
 Columns 7 through 12
  1.0000e+04  0           0           0           0           0
  0           1.0000e+04  0           0           0           0
  0           0           1.0000e+04  0           0           0
  0           0           0           1.0000e+04  9.2832e+02  0
  0           0           0           0           0           1.0000e+04
  0           0           0           0           0           0
 Columns 13 through 15
  0           0           0
  0           0           0
  0           0           0
  0           0           0
  9.2832e+02  0           0
  0           1.0000e+04  9.2832e+02
```

```
Ac =
 Columns 1 through 6
 -1.4142e+02  0            0            0            0            0
  0          -1.4142e+02   0            0            0            0
  0           0           -1.4142e+02   0            0            0
  0           0            0           -4.3089e+01   0            0
  0           0            0            0           -4.3089e+01   0
  0           0            0            0            0           -4.3089e+01
  1.0000e+00  0            0            0            0            0
  0           1.0000e+00   0            0            0            0
  0           0            1.0000e+00   0            0            0
  0           0            0            0            0            0
  0           0            0            1.0000e+00   0            0
  0           0            0            0            0            0
  0           0            0            0            1.0000e+00   0
  0           0            0            0            0            0
  0           0            0            0            0            1.0000e+00
 Columns 7 through 12
 -1.0000e+04  0            0            0            0            0
  0          -1.0000e+04   0            0            0            0
  0           0           -1.0000e+04   0            0            0
  0           0            0           -1.0000e+04  -9.2832e+02   0
  0           0            0            0            0           -1.0000e+04
  0           0            0            0            0            0
 -2.0000e+00  0            0            0            0            0
  0          -2.0000e+00   0            0            0            0
  0           0           -2.0000e+00   0            0            0
  0           0            0           -2.0020e+00   1.0000e+00   0
  0           0            0           -4.0010e-03   0            0
  0           0            0            0            0           -2.0020e+00
  0           0            0            0            0           -4.0010e-03
  0           0            0            0            0            0
  0           0            0            0            0            0
 Columns 13 through 15
  0           0            0
  0           0            0
  0           0            0
  0           0            0
 -9.2832e+02  0            0
  0          -1.0000e+04  -9.2832e+02
  0           0            0
  0           0            0
  0           0            0
  0           0            0
  0           0            0
  1.0000e+00  0            0
  0           0            0
  0          -2.0020e+00   1.0000e+00
  0          -4.0010e-03   0
```

REFERENCES

[1] M. Athans, *6.233-6.234 Course Notes*, MIT, Cambridge, MA, 1988 Fall-1989 Spring

[2] J. M. Abercrombie, "F/A-18 Flying Qualities Development", Technical Report MCAIR NO. 84-009, McDonnel Aircraft Company, 1984.

[3] I. K. Craig, "Sensitivity of H_∞ Controller Designs to Structured Uncertainty", S.M. Thesis, MIT, Cambridge, MA, 1988.

[4] J. A. Cro Granito, "Servo Design with Output Feedback", Sc.D. Thesis, MIT, Cambridge, MA, 1989.

[5] J. C. Doyle, K. Glover, P. Khargonekar, and B. A. Francis, "State Space Solutions to Standard H_2 and H_∞ Control Problems", *IEEE Trans. on Automatic Control*, Vol. AC-34, No. 8, pp. 831-847, 1989.

[6] N. Elgersma, and B. Morton, "Partial Inversion of Noninvertible Nonlinear Aircraft Models", UCB-NASA Ames Nonlinear Flight Control Workshop, Univ. of California, Berkeley, Aug. 1989.

[7] B. Etkin, *Dynamics of Flight: Stability and Control*, Wiley, New York, 1982.

[8] W. L. Garrad, and J. M. Jordan, "Design of Nonlinear Automatic Flight Control System", *Automatica*, Vol. 13, pp. 497-505, 1977.

[9] C. A. Hawkins, "Application of Bifurcation and Catastrophe Theories to Near Stall Flight Mechanics", S.M. Thesis, MIT, Cambridge, MA, 1985.

[10] J. K. Hedrick and S. Gopalswamy, "Nonlinear Flight Control Design via Sliding Methods", *AIAA Journal of Guidance and Control*, Vol. 13, No. 5 , pp.850-858, 1990.

[11] A. Inoue, "Structural Properties of Optimality Based Controller Parametrizations", S.M. Thesis, MIT, Cambridge, 1990.

[12] A. Isidori, *Nonlinear Control System: An Introduction*, Lecture Notes in Control and Information Sciences, Springer-Verlag, Berlin, 1985.

[13] P. Kapasouris, "Design for Performance Enhancement in Feedback Control Systems with Multiple Saturating Nonlinearities", Ph.D. Thesis, MIT, Cambridge, MA, 1988.

[14] H. Kwakernaak, and R. Sivan, *Linear Optimal Control Systems*, Wiley-Interscience, NY, 1972.

[15] S. H. Lane, and R. F. Stengel, "Flight Control Design Using Nonlinear Inverse Dynamics", *Automatica*, Vol. 24, pp. 471-483, 1988.

[16] G. Meyer, R. Sui, and L. R. Hunt, "Application of Nonlinear Transformations to Automatic Flight Control", *Automatica*, Vol. 20, pp. 103-107, 1984.

[17] P. C. Murphy, "Aerospace 88: Atmospheric Flight Mechanics", *Aerospace America*, Dec. 1988.

[18] J. W. R. Taylor, Editor, Jane's All the World's Aircraft 1987-88, Jane's Publishing Company, London, England, 1987.

[19] J.-J. E. Slotine and W. Li, *Applied Nonlinear Control*, Prentice Hall, Englewood Cliffs NJ, 1991.

[20] G.Stein, and M. Athans, "The LQG/LTR Procedure for Multivariable Feedback Control Design", *IEEE Trans. on Automatic Control*, Vol. AC-32, No. 2, pp. 105-114, 1987.

[21] G. Stein, "Controller with Guaranteed H_∞-Performance", *Lecture Notes in Multivariable Control Systems II*, MIT, Cambridge, MA, Spring 1989.

[22] P. Voulgaris, "High Performance Multivariable Control of the 'Supermaneuverable' F18/HARV Fighter Aircraft", S.M. Thesis, MIT, Cambridge, MA, 1988.